KØBENHAVNS
UNIVERSITET

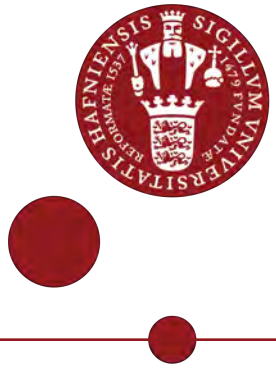

Geometry in Heavy Ions:

Estimating an Angular Power Spectrum

Meera Vieira Machado

Supervisor: Kim Splittorff

Co-supervisor: Poul Henrik Damgaard

Geometry in Heavy Ions:

Estimating an Angular Power Spectrum

Meera Vieira Machado

Supervisor: Prof. Kim Splittorff

Co-supervisor: Prof. Poul Henrik Damgaard

This thesis has been submitted to the PhD School of The Faculty of Science, University of Copenhagen

UNIVERSITY OF COPENHAGEN

"There is a theory which states that if ever anyone discovers exactly what the Universe is for and why it is here, it will instantly disappear and be replaced by something even more bizarre and inexplicable. There is another theory which states that this has already happened."

— Douglas Adams, *The Restaurant at the End of the Universe*

Abstract

Anisotropies found in the final state of heavy ion collisions carry a plethora of information on the creation, expansion and decoupling of the quark-gluon plasma. From the types of fluctuations present in initial conditions, to how jets interact with the medium, to quantum correlations between pairs of identical particles. At the same time, there is an overabundance of studies in azimuthal anisotropies in comparison to longitudinal ones.

This work proposes an analysis of correlations between particle pairs projected on a sphere. In other words, the objective lies in estimating an angular power spectrum of heavy ions. The data set at hand pertains to Pb-Pb collisions at $\sqrt{s_{NN}} = 2.76$ TeV measured by ALICE. Moreover, the selected events belong to the following phase space: $|\eta| < 0.9$, $0 \geq \phi < 2\pi$ and $0.15 < p_T < 100$ GeV.

The method for power spectrum estimation is developed under three main considerations: limited pseudorapidity coverage, typical event multiplicity and detector efficiency. The results are first tested on toy Monte Carlo simulations and later applied to heavy ion data. These are shown for five different centralities, ranging from 0-5% to 30-40%. Then, flow harmonics are extracted and compared to other methods of calculation. At last, spectra are computed for separate transverse momentum intervals $p_T < 0.54\,\text{GeV}$ and $p_T > 0.54\,\text{GeV}$, with each exerting dominance at distinct scales.

Dansk Resumé

Anisotropier fra den endelige tilstand af tunge ionkollisioner bærer en overflod af information om dannelsen, udvidelsen og afkoblingen af kvark-gluon-plasmaet. Fra de typer af udsving, der forekommer under indledende forhold, til hvordan stråler interagerer med mediet, til kvantekorrelationer mellem par af identiske partikler. Samtidig er der en overvægt af undersøgelser i azimutale anisotropier i sammenligning med langsgående.

Dette arbejde foreslår en analyse af korrelationer mellem partikelpar projiceret på en kugle. Det vil sige, målet er estimere et vinkel effektspektrum af tunge ioner. Datasættet ved hånden vedrører Pb-Pb-kollisioner ved $\sqrt{s_{NN}} = 2.76$ TeV målt af ALICE. Ydermere de valgte hændelser følgende faserum: $|\eta| < 0.9$, $0 \geq \phi < 2\pi$ og $0.15 < p_T < 100$ GeV.

Metoden til effektspektrum estimering er udviklet under tre hovedhensyn: begrænset pseudorapiditets dækning, typisk begivenheds-multiplicitet og detektor effektivitet. Resultaterne testes først på legetøj Monte Carlo simuleringer og anvendes senere på tung ion data. Disse vises for fem forskellige centraliteter, lige fra 0-5% til 30-40%. Derefter udvindes flow koefficienter og sammenlignes med andre beregningsmetoder. Til sidst beregnes spektre for separate tværgående momentintervaller $p_T < 0.54$ GeV og $p_T > 0.54$ GeV, med hver udøvende dominans på forskellige skalaer.

Acknowledgments

Firstly, I would like to thank Poul Henrik Damgaard and Kim Splittorff for accepting me into the PhD program on the Niels Bohr Institute. This goes along with my thanks to CNPq and the Science Without Borders program for giving me the opportunity to study in Denmark. Without them I would literally not be here.

I would like to further express my gratitude to Poul Henrik for not only the discussions on the results and pressuring me on writing papers, but also for the networking with both heavy ion physicists and cosmologists. Then I would like to thank Ante Bilandzic for teaching me two-particle correlation methods, as well as some ROOT and C++ programming. Part of it while working together for a week in the Technical University of Munich and also through emails. I thank Jens Jørgen Gaardhøje for the help on experimental ALICE data and being a co-author on my very first paper. This thanks is extended to Christian Bourjau for teaching me about detector acceptance and efficiency, for providing me the data used in this work and the discussions (sometimes over a beer). I am also grateful for the other professors from the HEHI group, for accepting me as a non-official member and inviting me to run on DHS. On the cosmology side, I thank Pavel Naselsky for the initial discussions on power spectrum estimation, as well as Hao Liu for teaching me some techniques applied to limited phase spaces. I also thank Sebastian for introducing me to HEALPix and Python programming. At last, I thank Bjorn for helping me choose a proper computer and Axel for the poster printings and fun conversations.

At this point I would like to thank my parents Zuleide and Wagner, alongside my family for the endless support. Also, I would like to thank Laís for the beers and for helping me practice my Portuguese. Then I thank Emilie for letting me make fun of her and specially for the hugs, and Željka for the fun late-night conversations. I thank Katarína for the beers, as always, but also the fun trips we had together. Just like in Em-

ilie's case, I thank Fabian for also letting me make fun of him, the beers and board games. The latter is extended to Jógvan. Without further ado, I thank Vytautas, Freja, Vojtech, Jean-Loup, Helene for beers, fun conversations and PhD camaraderie. Likewise, I thank my office mates Andreas, Laurie, Ania, Anagha and previous ones, Laure, Jeppe and Amel. Additionally, I thank Elmar and his family for receiving me and providing support when I had just arrived in Europe, and Marie and her family for doing the same. I also thank all my friends outside of Denmark and Europe.

Contents

1 Introduction

"Our whole universe was in a hot dense state..."
— Barenaked Ladies, *Big Bang Theory Theme*

In the universe timeline, the soup of elementary particles is placed right after inflation, a theory of rapid space-time expansion. Ordinary matter was then trapped in gravitational wells, its outwards driven pressure in a tug-of-war with the compressing dark matter. As the universe cooled and expanded, fundamental particles clumped to each other, forming ever increasing complex matter. The first atoms bound the electrons, ceasing their interaction with photons and allowing the latter to freely stream. These carried an imprint of the surface of last scattering, whose features became anisotropies in the Cosmic Microwave Background (CMB), first discovered by radio astronomers in 1964 [1].

The very early stage of the particle soup was denoted *quark epoch*, since the universe was hot and dense enough for quarks to roam free. Otherwise, they would be confined into hadrons, quark-composites such as protons and neutrons, which would later combine into nuclei. Quarks are bound together by gluons, the mediator of the strong force. They are

carriers of color charge and the theory describing their interactions is, accordingly, the Quantum Chromodynamics (QCD).

The quark soup was produced in 2005 [2–5] through collisions of gold nuclei Au-Au at center-of-mass energy $\sqrt{s_{NN}} = 200$ GeV per nucleon pair. This experiment was performed inside the Relativistic Heavy Ion Collider (RHIC). When pairs of quarks and gluons collide directly, sprays of hadronic and gluon matter may scatter back-to-back, the so called jets. Nevertheless, it was observed in RHIC that one of these jets was weaker or completely extinguished, a phenomenon denoted as *jet quenching*. They were absorbed by the medium created in the collision, the quark-gluon plasma (QGP).

Presently, the QGP is also produced and studied in the Large Hadron Collider (LHC). Lead nuclei Pb-Pb are accelerated to energies of $\sqrt{s_{NN}} = 5.02$ TeV and $\sqrt{s_{NN}} = 2.76$ TeV (before year 2013). The QGP acquires its name due to its reigning degrees of freedom. After its creation, the plasma expands and cools, much akin to the early universe, until quarks and gluons recombine into hadrons. These still interact and then freely stream, finally reaching the detectors. When nuclei collide peripherally, they form an initial almond-like shape. This peculiar structure can be observed in the final particle distribution [6–8], suggesting that the QGP behaves collectively, i.e., it is a liquid.

The CMB photons were part of a plasma containing nuclei and electrons. Meanwhile, hadrons observed in the LHC arise from a plasma of quarks and gluons. For the first, gravity had a role of pressuring matter into wells, their pressure interplay etching structures on the scattered photons. For heavy ions, pressure gradients along and transverse to the collision axis drive the collective QGP expansion, thus carrying imprints of the initial configuration into the emitted hadrons. For the CMB, the angular power spectrum is the tool that quantifies the primordial geometries, thus providing constraints to cosmological parameters, e.g., dark matter and dark energy densities, the universe curvature, and the Hubble constant. For the QGP, anisotropies on the transverse direction have

provided information on the equation of state and transport properties of the plasma, like its viscosity.

Inspired by the production of primordial quark-gluon soup in labs, this work proposes another perspective on the geometries of final state heavy ion collisions: estimating its angular power spectrum. As the name itself implies, the latter quantifies correlations between angular-coordinate pairs, thus providing a new window into the final particle distributions. The analysis is done for A Large Ion Collider Experiment (ALICE) open data [9, 10] of Pb-Pb collisions at $\sqrt{s_{NN}} = 2.76$ TeV. Following up, the structure of this thesis is laid out.

In Ch. 2 a brief overview on heavy ion collisions is presented: from the initial conditions, to the QGP and its hydrodynamic expansion, until its transition into hadrons and final scattering of particles (Sec. 2.1). Afterwards, the focus lies on the calculation and measurements of anisotropies on the plane transverse to the collision. These are discussed as they change from central to peripheral collisions, in addition to their dependence on transverse momentum. At last, anisotropies along the longitudinal direction are tackled, with a briefing on two-particle angular correlations (Sec. 2.2).

In Ch. 3 the concept of a power spectrum is introduced. First, it is presented in the 1-D case from a Fourier expansion. A few simple examples illustrate how it quantifies frequencies in a given signal (Sec. 3.1). Then, complexity increases as we move on to functions defined on a sphere. These are expanded in spherical harmonics, from which the angular power spectrum can be calculated (Sec. 3.2). The CMB is succinctly described alongside its temperature map and angular power spectrum. The latter's main features are synthesized within the current cosmological paradigm (Sec. 3.3).

In Ch. 4 the data set, software and analysis method are discussed. It begins with a short introduction on the main ALICE detectors used in the event selection, culminating on the data phase space (Sec. 4.1). Afterwards, we present the software that maps particles distributions

on a sphere and computes their power spectra (Sec. 4.2). Lastly, the method used to estimate the data spectrum is fully delineated using examples from toy Monte Carlo simulations. Effects of detector acceptance (Sec. 4.3.1) and efficiency (Sec. 4.3.3) are tackled as well as an issue caused by the typical number of particles per event (Sec. 4.3.2). Finally, the method is applied for distinct pixel resolutions and the choice made on this work is justified (Sec. 4.3.4).

In Ch. 5 the data itself is at last put under the analysis developed in the previous chapter. First, the beam position of the nuclei collision is considered, since uncovered regions may give rise to artificial spectral structures (Sec. 5.1). Secondly, the aforementioned method is used to estimate the angular power spectrum of heavy ions; results are displayed from central to peripheral collisions (Sec. 5.2). Then, the spectrum is translated into known experimental observables for MC simulations and ALICE data and compared to other calculations (Sec. 5.3). Lastly, the power spectrum is evaluated for two transverse momentum intervals (Sec. 5.4).

The highlights of this study are summed up in Ch. 6. Furthermore, this thesis is the mid-point between the following works:

1. Machado, M., Damgaard, P. H., Gaardhøje, J. J. & Bourjau, C.
   Angular power spectrum of heavy ion collisions.
   Phys. Rev. C **99**, 054910 (5 May 2019)

2. Machado, M.
   Heavy ion anisotropies: a closer look at the angular power spectrum.
   To be submitted in June 2019.

2 On Heavy Ions and Geometry

"The most exciting phrase to hear in science, the one that heralds new discoveries, is not 'Eureka!' but 'That's funny...'"

— Isaac Asimov

The lab-created quark-gluon plasma plays a fundamental role not only in the study of QCD matter, but in understanding the state of the universe post-inflation. In this chapter, we begin with a qualitative description of the QGP formation from heavy ion collisions, how it evolves, and what sort of signature its products leave in a detector. Subsequently, we present the idea of studying the final azimuthal particle distribution through Fourier decomposition and how that aids in probing properties of the QGP itself.

2.1 Overview of the collision

Nuclei accelerated to relativistic energies appear as Lorentz contracted discs in the center-of-mass (lab) frame. From their collision to the resulting hadron distribution, the participating nucleons undergo three main stages: the initial overlap and very first field interactions,

the quark-gluon phase ruled by hydrodynamics, and the hadronization, where last scatterings and free streaming take place.

2.1.1 Initial conditions

The number of nucleons participating in the formation of a QGP and its subsequent evolution depends on the distance between the incoming nuclei, as seen in Fig. 2.1. The impact parameter **b** is the vector denoting the offset of the nuclei's centers perpendicular to their movement. Small $|\mathbf{b}|$ values indicate head-on or central collisions, while large values describe non-central or peripheral collisions. Assuming that the number of particles, or multiplicity, changes monotonically with **b**, the former can be used to determine the collision centrality [11].

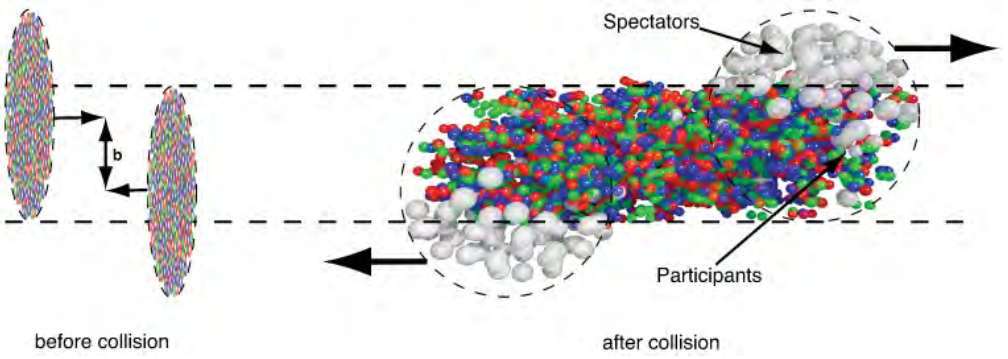

Figure 2.1: Longitudinal view of a heavy ion collision. Image from [11].

The impact parameter also influences the overall geometry of the initial overlapping region of the incoming nuclei, as shown in Fig. 2.2. The beam axis, represented by z, and **b** define the reaction plane Ψ_R. Central collisions yield an approximately circular shape and, as the nuclei collide more peripherally, said shape becomes more almond-like. Additionally, since nuclei are composited of individual nucleons, each collision exhibits a degree of lumpiness driven by nucleon interactions [12].

The combination of these factors results in a primordial stage anisotropy which will be imprinted in the final particle distribution, a subject explored throughout this thesis.

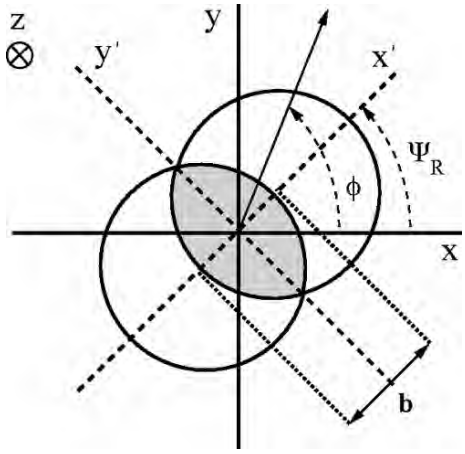

Figure 2.2: Heavy ion collision on the transverse plane. Image from [13].

The understanding of the early stage regime and its physics is still an ongoing discussion, with distinct ideas and interpretations being constantly tested and improved on, for a review see [14]. A currently accepted theoretical framework relies on the following statement: as a hadron accelerates, its energy increases and so does the gluon density and apparent pairs of quarks and anti-quarks ($q\bar{q}$) inside it. Then, when the number of gluons surpasses that of other particle species, a hadron is said to saturate and it is called Color Glass Condensate (CGC) [15]. The term *color* stands for the charge associated with QCD interactions. *Glass* represents a disordered system which acts like a solid on short time scales while behaving like a liquid on long time scales, in analogy to actual glasses. Lastly, *condensate* indicates the high gluon density saturation itself [15]. The transformation from a proton to CGC at relativistic energies is represented on the left of Fig. 2.3.

As two CGC discs collide, their transverse field configurations

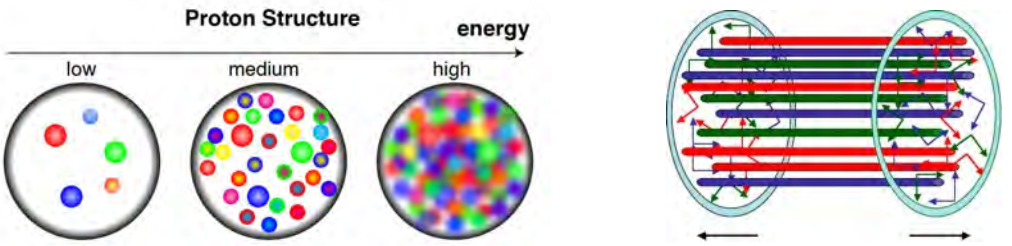

Figure 2.3: Left: CGC formation, image from [16]. Right: Glasma in early stages of hadronic collisions, image from [17].

change into longitudinal color electric and magnetic fields, which fill the medium between the receding colored glass sheets, as depicted on the right of Fig. 2.3. This resulting pre-QGP state is denoted *Glasma* [18–22] and it gradually decays into $q\bar{q}$ pairs and gluons. The name itself is a contraction of "glass" from Color Glass Condensate and "plasma" from quark-gluon plasma, a direct reference to its role as an intermediate phase.

Driven by the collision's kinetic energy and pressure, matter from the immediate aftermath expands both in the longitudinal direction and along the transverse plane. At this stage, interactions are mostly "soft", i.e., with momentum transfers in the order of GeV: fields exchange color charge and $q\bar{q}$ pairs and gluons are created from the energy deposited in the medium.

Due to the collective expansion of the medium, the initial quark-gluon configuration and its dynamics are carried on through the whole system's evolution, resulting in correlations within the final particle distribution. The latter's description on the transverse plane has been thoroughly studied, for a review see [12, 23, 24]. However, to form the full picture of heavy ion collisions, one must understand its dynamics in all four space-time coordinates. Hence the necessity to compute longitudinal-dependent fluctuations and put initial condition models to

the test.

2.1.2 Hydrodynamization and QGP phase

As the name itself suggests, the quark-gluon plasma is a state of matter whose degrees of freedom are quarks and gluons. The energy density of the system surpasses that of hadrons, thus leaving the aforementioned particles deconfined, yet strongly coupled to their neighbors [12]. While the colliding nuclei recede from each other, QGP is forming and expanding in the space between them.

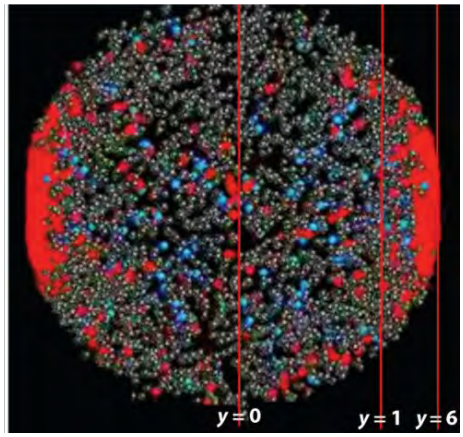

Figure 2.4: Red spheres indicate the QGP, while gray and blue ones are hadrons. Image adapted from [12].

A stage of QGP production is depicted in Fig. 2.4, where the plasma itself is represented in red. Hadrons resulting from the former's cooling are in blue and gray. Different phases of this expansion are associated with momentum rapidity y coordinates. This quantity relates to the Lorentz factor $\gamma = 1/\sqrt{1 - v_z^2}$ through $\cosh(y) \equiv \gamma$, with v_z the velocity along beam direction. Note how the hottest regions (red) in Fig. 2.4 are concentrated at high y. The receding nuclei are gradually losing en-

ergy as quarks and gluons separate from them. These particles move at relativistic speeds, meaning that when they form QGP in their own reference frame, this process will be delayed in the lab frame due to time dilation. Meanwhile, particles at mid-rapidity will be already combining into hadrons. Altogether, quarks and gluons at distinct rapidities produce QGP at different times in the center of mass frame [12].

A generalized formulation of relativistic hydrodynamics takes it as an effective theory for low-energy degrees of freedom (first terms of gradient expansion) consistent with the basic symmetries of the system [25]. In the simplest scenario, there should be energy-momentum conservation, which in turn leads to hydrodynamic equations of motion $\partial_\mu T^{\mu\nu} = 0$ with stress tensor $T^{\mu\nu}$ given by

$$T^{\mu\nu} = \epsilon u^\mu u^\nu - (p + \Pi)\Delta^{\mu\nu} + \pi^{\mu\nu}, \tag{2.1}$$

for energy density ϵ, flow velocity u^μ and pressure p. The projection tensor $\Delta^{\mu\nu} = g^{\mu\nu} - u^\mu u^\nu$ defines the covariant form of the gradient, $\nabla^\mu \equiv \Delta^{\mu\nu}\partial_\nu$, while $\pi^{\mu\nu}$ and Π are shear and bulk viscous corrections to the tensor, respectively. Their expressions are

$$\pi^{\mu\nu} = \eta\sigma^{\mu\nu} + \mathcal{O}(\nabla^2), \qquad \Pi = -\zeta\nabla_\mu u^\mu + \mathcal{O}(\nabla^2), \tag{2.2}$$

to first order approximation in the gradient expansion, with η and ζ the shear and bulk viscosity coefficients. Lastly, $\sigma^{\mu\nu} = \nabla^\mu u^\nu + \nabla^\nu u^\mu - 2/3\Delta^{\mu\nu}\nabla_\alpha u^\alpha$.

The hydrodynamic variables of pressure and viscous coefficients depend on energy density according to an equation of state obtained from QCD calculations on the lattice [26]. Viscosity dissipates anisotropies, as larger η facilitate momentum exchange between distant fluid elements, while ζ determines the liquid's resistance to expansion or compression. Furthermore, the QGP has a low shear viscosity to entropy ratio $\eta/s \sim \mathcal{O}(1/4\pi)$ [27], a value consistent with the theoretical expectation for a

strongly coupled plasma [28]. The effects of bulk viscosity may become apparent when quark-gluon matter combines into hadrons [12, 29].

Hydrodynamization pertains to the stage where the medium can be treated as a low-viscosity liquid. Spatial anisotropies generate pressure gradients and the fluid expands faster along larger differences in pressure. Therefore, hydrodynamics converts spatial anisotropies into momentum ones [12]. This is the standing paradigm of heavy ion collisions: the initial spatial anisotropies are found to evolve collectively and leave their imprint on the final charged particle distribution, thus making the QGP a strongly coupled system [30, 31].

2.1.3 Freeze out

The fluid cools and expands, its energy density dropping below that typical of a hadron (~ 500 MeV/fm^3) [12], finally resulting in quarks and gluons recombining. This shift in degrees of freedom occurs smoothly, i.e., the phase transition between a plasma of quarks and gluons and a hadron gas is of crossover type [32], shown in Fig. 2.5. The gradual formation of said hadron stage can be seen simplified in Fig. 2.4.

After the process of hadronization is complete, the system reaches chemical freeze out: hadrons cease to scatter inelastically, thus establishing the species of particles produced. At this point the latter exchange solely kinetic energy between them [12]. Subsequently, elastic scatterings also stop, determining the momentum spectrum of the resulting particles; this is referred to as kinetic freeze out. Lastly, these particles stream freely, finally reaching the detectors. Different species may have distinct chemical and kinetic freeze out temperatures. Further, hadronic scattering during this last phase may have significant contribution to the final stage geometry, due to momentum conservation.

Finally, we make a brief remark on particle interactions involving momentum transfers of order greater than tens of GeV. Albeit rare, these hard collisions can produce heavy quarks, high transverse momentum

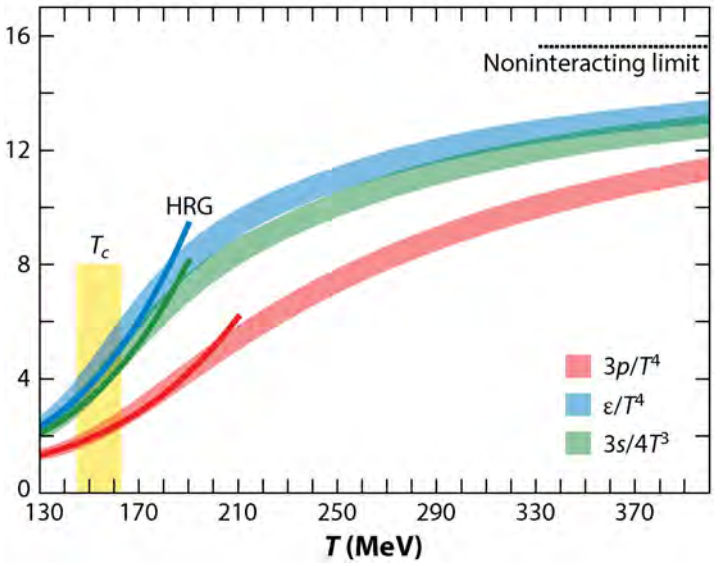

Figure 2.5: Normalized pressure, energy density, and entropy density as functions of temperature. Thin lines are predictions of the Hadron Resonance Gas (HRG) model. Crossover region represented by T_c. Image adapted from [33].

hadrons, and two collimated hadron sprays with $\Delta\phi \approx \pi$ azimuthal separation, commonly denoted as jets. All of these products must cross a region where QGP is still forming and evolving, thus making them retain information on the medium.

The space-time diagram of relativistic heavy ion collisions is depicted in Fig. 2.6. It illustrates the different stages discussed in this section: from the nuclei colliding that shape the initial overall geometry (A,B), to the deconfinement of quarks and gluons into Glasma (gray) and its subsequent QGP formation and collective expansion (red), to the crossover (orange) into a hadron gas (dark blue), and finally the surface of last scattering (light blue). Experimentally, the resulting particle distribution is the only window to the study of the aforementioned phases and their

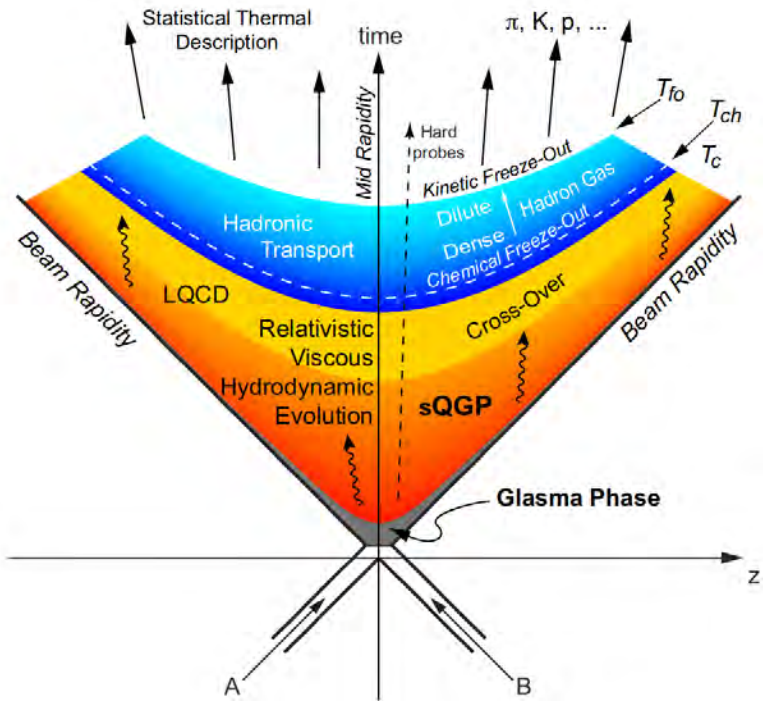

Figure 2.6: Time evolution of a heavy ion collision with each of its stages separated by hyperboles. A and B interact at $z = 0$. Image from [34].

underling dynamics. Hence the focus on quantifying the final state geometry from this point onward.

2.2 Azimuthal anisotropies

The coordinates of hadrons emitted from heavy ion collisions can be represented in terms of pseudorapidity η, azimuthal angle ϕ and transverse momentum p_T. The first is a spatial quantity defined as $\eta \equiv -\ln[\tan(\theta/2)]$, where θ is the particle's polar angle with respect to the beam axis. Also, $p_T \equiv |\mathbf{p}| \sin\theta$, with $\mathbf{p}$ the particle's three-momentum.

Alternatively, η can be written as a function of $\mathbf{p}$ and longitudinal momentum p_L through the expression $\eta = \tanh^{-1}(p_L/|\mathbf{p}|)$ and, in the limit of negligible particle mass $m \ll |\mathbf{p}|$, it is approximately equal to rapidity, $\eta \approx y$. It should be remarked that η will represent pseudorapidity throughout the rest of this thesis, while shear viscosity is denoted as η/s, its specific value.

The final particle distribution is given in terms of the aforementioned coordinates (η, ϕ, p_T). Its azimuthal part may be expanded in a Fourier series [35, 36]:

$$\frac{dN}{d\phi} \propto 1 + 2\sum_{n=1}^{\infty} v_n \cos[n(\phi - \Psi_n)], \tag{2.3}$$

where N is the number of produced particles, v_n are denoted *flow coefficients* and Ψ_n are their corresponding symmetry planes, i.e., the overall orientation of the n^{th} moment. For $n = 1, 2, 3, 4$ v_n can be referred to as directed, elliptic, triangular, and quadrangular flow, respectively. Their values quantify the final state anisotropies, which in turn "flowed" from their origins in the nuclei collision itself, hence the nomenclature. The Fourier decomposition will be further discussed in Ch. 3 within a different context.

Using the orthogonality of trigonometric functions, it is straightforward to see that $v_n = \langle \cos[n(\phi - \Psi_n)] \rangle$, i.e., the expected value of cosine averaged over all emitted particles in a single event. There are various methods to compute integrated v_n [13, 36–42], though the focus of this section lies on their calculation through multi-particle correlations [40, 41] using the Q-cumulants method [13, 42].

Due to even symmetry with respect to Ψ_n, $\langle \sin[n(\phi - \Psi_n)] \rangle = 0$ and the flow coefficients can be rewritten as $v_n = \langle e^{in(\phi - \Psi_n)} \rangle$. Though the symmetry plane orientation Ψ_n cannot be directly accessed experimentally, it is possible to measure the emitted particles' relative azimuthal angles. As a consequence, the flow analysis may rely, for instance, on the calcula-

tion of two-particle azimuthal correlations $\langle e^{in(\phi_1-\phi_2)}\rangle$. The latter is the average over all relative azimuthal angles of a single event.

The relation between two-particle correlations and v_n is quite straightforward under the assumption of factorization:

$$\langle e^{in(\phi_1-\Psi_n)} \cdot e^{-in(\phi_2-\Psi_n)}\rangle = \langle e^{in(\phi_1-\Psi_n)}\rangle \cdot \langle e^{-in(\phi_2-\Psi_n)}\rangle = v_n^2, \tag{2.4}$$

which states that azimuthal correlations between two particles come solely from their correlation with the symmetry plane. However, jets, resonance decays, and quantum fluctuations are all sources of correlations unrelated to initial overlap geometry. These are also referred to as *non-flow* and they modify Eq. (2.4): $\langle e^{in(\phi_1-\phi_2)}\rangle = v_n^2 + \delta_n$, with δ_n the non-flow contribution.

Computing azimuthal anisotropies using multi-particle correlations suppresses non-flow effects [13, 40–42]. Nevertheless, for the sake of this thesis' core analysis and simplicity, only the two-particle function will be explicitly calculated. It should also be remarked that higher order correlations depend on the latter.

For a single event with final multiplicity M and measured particle azimuthal angles $\phi_1, \cdots, \phi_M$, the search for anisotropies in the ϕ distribution begins with introducing the Q-vector [13, 40],

$$Q_n \equiv \sum_{j=1}^{M} e^{in\phi_j}, \tag{2.5}$$

with ϕ_j the azimuthal angle of the j^{th} particle. This global quantity is rather useful on the calculation of both two- and multi-particle correlations, due to the need of going over all possible multiplets. Accordingly, the single-event average two-particle correlation $\langle 2\rangle$ follows the expres-

sion [13]:

$$\langle 2 \rangle \equiv \langle e^{in(\phi_1 - \phi_2)} \rangle \equiv \frac{(M-2)!}{M!} \sum_{i \neq j}^{M} e^{in(\phi_i - \phi_j)}. \tag{2.6}$$

Note that $|Q_n|^2$ involves diagonal terms equal to the total event multiplicity and off-diagonal ones proportional to the two-particle correlation function. As a result $\langle 2 \rangle$ can be written in terms of the Q-vector's absolute value squared:

$$\langle 2 \rangle = \frac{|Q_n|^2 - M}{M(M-1)}. \tag{2.7}$$

After averaging over all particles of a single event, it is now possible to compute the averaged two-point correlation function over the whole event ensemble $\langle\langle 2 \rangle\rangle$. Explicitly, it consists of the weighted average of $\langle 2 \rangle$, where each event weight is chosen according to its multiplicity $W_{\langle 2 \rangle} \equiv M(M-1)$.

The average two-particle correlation is the second order cumulant, $c_n\{2\} = \langle\langle 2 \rangle\rangle$ [41]. It provides an estimation for the n^{th} harmonic through the expression

$$v_n\{2\} = \sqrt{c_n\{2\}}. \tag{2.8}$$

Higher order cumulants and the above calculation for detectors with non-uniform acceptance are detailed in [13, 42]. The concept of correlations will be revisited and further explored in the next chapter.

In general, both flow coefficients v_n and symmetry planes Ψ_n in Eq. (2.3) can be functions of pseudorapidity and transverse momentum. Following up, we firstly present the centrality dependence of Pb-Pb collision measurements of v_n integrated over η and p_T. Then, v_n as a function of p_T and η are discussed. These last two are also denoted *differential* flow.

2.2.1 Centrality dependence

The overlap region of colliding nuclei has a transverse geometry that depends on the impact parameter vector, as seen in Fig. 2.2. If the initial spatial distribution was smooth, the reaction plane would coincide with the symmetry plane $\Psi_R = \Psi_n$ and odd harmonics would vanish. However, the positions of participating nucleons generate a spatial asymmetry which changes event-by-event, thus falsifying the previous statement.

Figure 2.7: Representation of elliptic (left) and triangular (right) azimuthal anisotropies. Participant nucleons indicated in pink. Image from [43, 44].

The initial ellipsoidal shape propagates hydrodynamically to the final state and causes v_2 to be the dominant flow coefficient. In Fig. 2.7 (left), an example of pure elliptic anisotropy is displayed with orientation Ψ_2 relative to the reaction plane. Higher harmonics are associated with the collective expansion of fluctuations on the initial energy density: from Fig. 2.7 (right), the ellipse is now distorted due the interactions between nucleons, the interacting region has a triangular shape quantified by the sum of harmonics v_2 and v_3. The increase in deformation will cause flow harmonics with higher n to be non-zero.

As previously mentioned methods of two- and multi-particle correlations can be employed to calculate flow harmonics. For the latter, non-flow contributions are negligible [46] whereas for the former, it is nec-

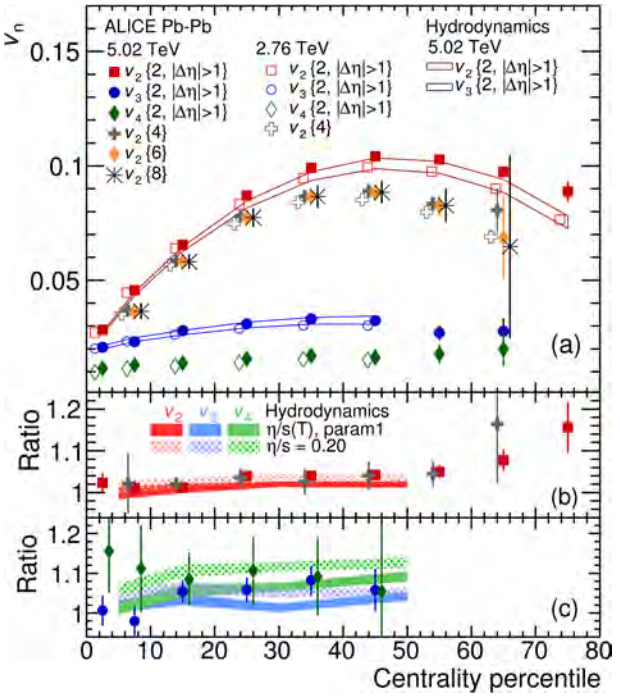

Figure 2.8: Integrated flow coefficients as a function of centrality for collision energies 2.76 TeV and 5.02 TeV. Image from [45], results by the ALICE Collaboration.

essary to suppress their effects. Reason being the plethora two-particle correlation sources. In order to extract solely the global elliptic geometry, a pseudorapidity gap between particle pairs is required [45]. Each event is split into two sides with a minimum separation $|\Delta\eta|$ between them. Their respective Q-vectors, $Q_{n,A}$ and $Q_{n,B}$, are then calculated and the single-event two-particle correlation becomes [47]:

$$\langle 2 \rangle = \frac{Q_{n,A} Q^*_{n,B}}{M_A M_B}, \tag{2.9}$$

with M_A and M_B the respective multiplicities of sub-events A and B. The event weight is given by $W_{\langle 2 \rangle} = M_A M_B$. The estimation of v_n then pro-

ceeds through Eq. (2.8).

The v_n results in Fig. 2.8 were obtained through two-particle correlations with a pseudorapidity gap of $|\Delta\eta| > 1$ and multi-particle correlations. The first is denoted as $v_n\{2, |\Delta\eta| > 1\}$ and the latter as $v_n\{4\}$, $v_n\{6\}$ and $v_n\{8\}$. Measurements of harmonic flow coefficients v_2, v_3, v_4 as functions of event centrality are depicted in Fig. 2.8 (a) for Pb-Pb collisions at center-of-mass energies $\sqrt{s_{NN}} = 5.02$ TeV and 2.76 TeV. Pseudorapidity is limited within $|\eta| < 0.8$ and v_n were integrated over the p_T range $0.2 < p_T < 5.0$ GeV. The ratios of v_n between higher and lower energies are shown in Fig. 2.8 (b-c).

The dominance of v_2 over the other coefficients is clearly visible in Fig. 2.8 (a). Also, it increases from central to peripheral centralities, reaching its maximum value for the 40-50% most central collisions. This behavior of v_2 reflects its relation to the initial almond shape seen in Figs. 2.2 and 2.7. Higher harmonics, on the other hand, have relatively less centrality dependence. Lastly, the difference in v_2 calculated with two- and multi-particle correlations should be due to elliptic flow fluctuations [45].

Given an initial anisotropy configuration, hydrodynamics is responsible for etching its shape into the final particle distribution. At the same time, the equations of motion depend on transport coefficients, i.e., viscosity. If $\eta/s = 0$ the primordial global geometry remains intact and v_n values are driven up. In the opposite scenario, the anisotropies are dampened down and v_n decreases. Therefore, flow measurements provide constraints on the η/s parameter. For this reason, predictions from a hydrodynamic model [48] are compared to the v_n measurements in Fig. 2.8 (a), thus quantifying the collective evolution of initial condition fluctuations. Another model [49] is displayed in Fig. 2.8 (b-c) and it makes use of both constant and temperature dependent viscosities η/s.

2.2.2 Transverse momentum

Differential flow, i.e., v_n for a given type of particle as a function of p_T and η, requires a slightly more distinct formalism than the one presented in the beginning of this section. The reason being lower statistical sample size due to the reduced phase space. A brief description of said calculation follows.

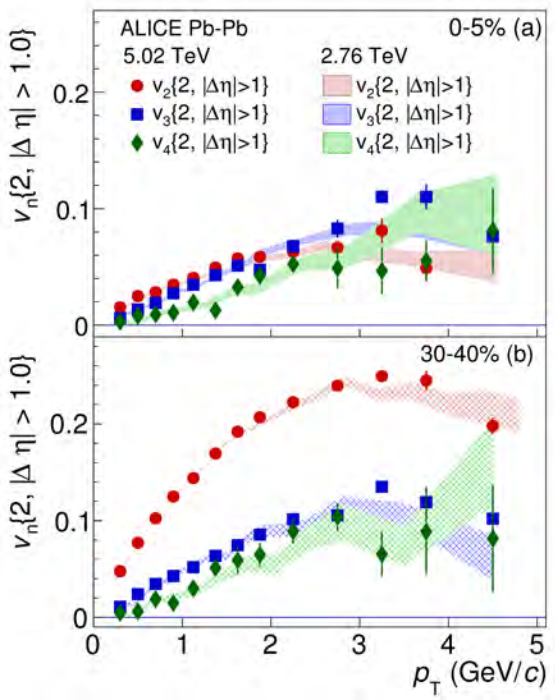

Figure 2.9: Differential flow as a function of transverse momentum for collision energies 2.76 TeV and 5.02 TeV as well as centrality classes 0-5% and 30-40%. Image from [45], results by the ALICE Collaboration.

The analysis for $v_n(p_T)$ is done in two main steps. Firstly, reference particles are chosen[1] and their n^{th} harmonic calculated using Eqs. (2.7,

[1]Those may comprise the whole event sample.

2.8). Secondly, the particles of interest are defined, namely the ones whose differential flow is to be computed. Analogously to the sub-events with an η gap, the two-point correlation is calculated between pairs comprising particles of interest and reference particles. The differential flow is thus given by the ratio between this their event ensemble weighted average and v_n of the reference particles [13, 41]. This can be extended to multi-particle correlations.

The method of differential flow for the two-particle cumulant was employed in Fig. 2.9 with a pseudorapidity gap of $|\Delta\eta| > 1$ for harmonics with $n = 2, 3, 4$. Results are shown for the 0-5% and 30-40% centralities and center-of-mass energies per nucleon 5.02 TeV and 2.76 TeV. The overall trend is the increase of v_n with transverse momentum: it implies that particles emitted with higher p_T transferred hardly any of their momentum to the medium, thus retaining their initial geometry. So measurements of $v_n(p_T)$ are sensitive to initial conditions.

In regards to shear viscosity, $v_n(p_T)$ would only increase with p_T for $\eta/s = 0$. Nevertheless, in Fig. 2.9 they seem to decrease or stay constant after a certain p_T value, indicating the presence of viscosity in the medium. At last, they could also provide information on other evolution stages, such as freeze-out, since the latter influences the final momentum configuration.

2.2.3 Pseudorapidity

The calculation of η-differential flow depicted in Fig. 2.10 relies on the scalar product method [50, 51]. It computes the particles correlation with a global frame, i.e., the event plane Ψ_n which are represented by Q-vectors. The region of interest (ROI) is defined by the chosen η-range η_{ROI}, while the reference region should have a pseudorapidity value with a sufficiently large η gap relative to the particles of interest. Again particle pairs from distinct intervals in the phase space are correlated to each other.

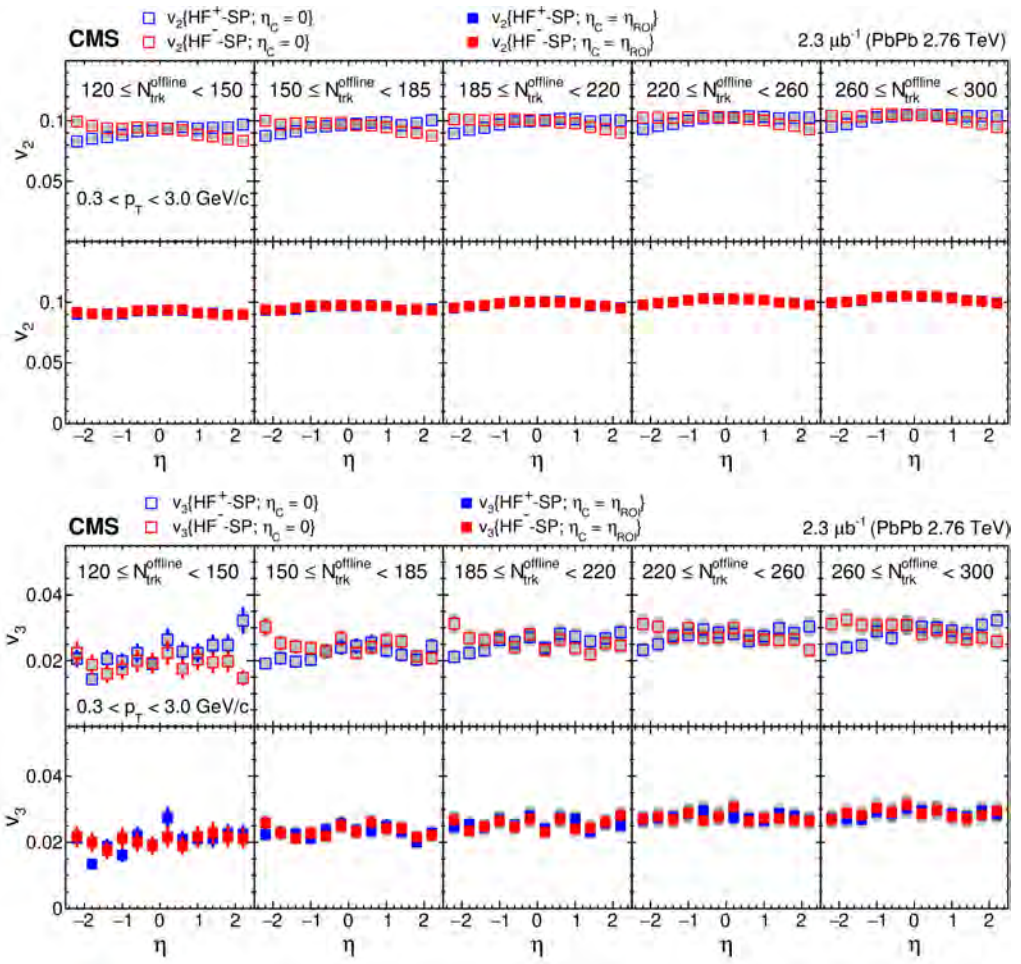

Figure 2.10: Flow coefficients v_2 and v_3 as a function of pseudorapidity for different centralities, 55% to 67%. Images from [52], results by the CMS Collaboration.

Results from the Compact Muon Solenoid (CMS) experiment shown in Fig. 2.10 have two reference event planes denoted by HF^+ and HF^-, which correspond to $-5 < \eta < -3$ and $3 < \eta < 5$ intervals, respectively. The pseudorapidity value η_C is a correction to the resolution of the ref-

erence plane [52]. The ranges of $N_{\text{trk}}^{\text{offline}}$ relate to centrality: higher values mean more central collisions.

The values of v_n for different choices of η_C diverge from each other for both elliptic and triangular flow. Since the reference event plane should approach the global one, this suggests a dependence of symmetry plane Ψ_n on η, which might play a significant role in understanding $v_n(\eta)$ [52]. The $\Psi_n(\eta)$ effect could be caused by fluctuations on the initial positions of nucleons and their constituents, namely random positioning. Alternatively, it could arise from a torqued QGP in the longitudinal direction [53]. Although this matter is still under investigation [23], it suggests that final state anisotropies could have non-trivial dependencies on η.

Lastly, we present the two-particle angular correlation in relative pseudorapidity $\Delta\eta$ and relative azimuthal angle $\Delta\phi$. Each of the aforementioned sources of correlation leave an imprint on the $(\Delta\phi, \Delta\eta)$ distribution.

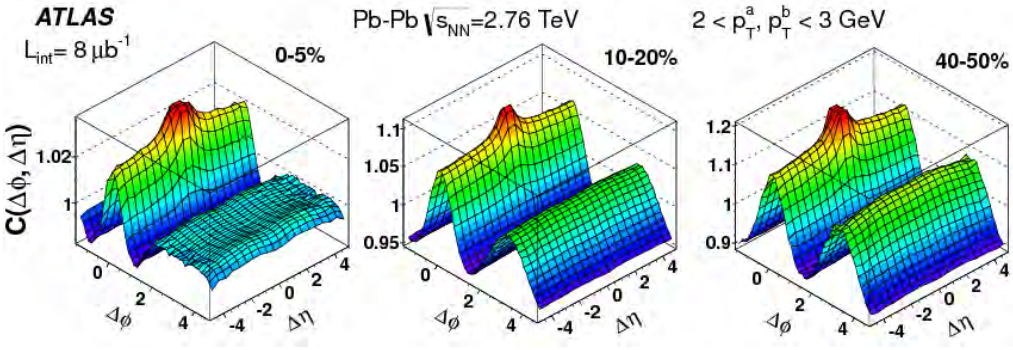

Figure 2.11: Two-particle angular correlation, $C(\Delta\phi, \Delta\eta)$, for different centralities at $\sqrt{s_{NN}} = 2.76$ TeV collision energy; L_{int} is integrated luminosity. Image adapted from [54], results by the ATLAS Collaboration.

The two-particle correlation function $C(\Delta\phi, \Delta\eta)$ is a measurement of particle pairs separated in azimuthal angle $\Delta\phi = \phi^a - \phi^b$ and pseudo-

rapidity $\Delta\eta = \eta^a - \eta^b$. The labels a and b represent the particles which constitute a pair. Explicitly, it is calculated through the average of pair distributions over detector acceptance [54],

$$C(\Delta\phi, \Delta\eta) = \frac{S(\Delta\phi, \Delta\eta)}{B(\Delta\phi, \Delta\eta)}, \tag{2.10}$$

where

$$S(\Delta\phi, \Delta\eta) = \int d\phi_a d\eta_a d\phi_b d\eta_b \delta_{ab} \frac{d^4N}{d\phi_a d\eta_a d\phi_b d\eta_b}, \tag{2.11}$$

$$B(\Delta\phi, \Delta\eta) = \int d\phi_a d\eta_a d\phi_b d\eta_b \delta_{ab} \frac{d^2N}{d\phi_a d\eta_a} \frac{d^2N}{d\phi_b d\eta_b}, \tag{2.12}$$

and δ_{ab} stands for $\delta(\phi_a - \phi_b - \Delta\phi)\delta(\eta_a - \eta_b - \Delta\eta)$. Moreover, $S(\Delta\phi, \Delta\eta)$ is composed of same-event pairs, while $B(\Delta\phi, \Delta\eta)$ has mixed-event pairs. The A Toroidal LHC ApparatuS (ATLAS) experiment measures $C(\Delta\phi, \Delta\eta)$ over its full azimuth and $|\eta| < 2.5$. Its result is depicted in Fig. 2.11 for three centralities and particle pairs within $2 < p_T < 3$ GeV.

There are three remarkable features in the measurements on Fig. 2.11: a peak in $(\Delta\phi, \Delta\eta) \approx (0, 0)$, a ridge-like structure around $\Delta\phi \approx 0$ and, for the more peripheral centralities, another ridge around $\Delta\phi \approx \pi$, while a nearly flat plateau for 0-5%. The first comes from short range correlations, such as resonance decays, Hanbury Brown and Twiss (HBT) effects [55] and jet fragmentation [56]. As for the ridges, flow harmonics are their main cause [57], though back-to-back jets also contribute to the long range structure around $\Delta\phi \approx \pi$ [58].

In the field of heavy ions, azimuthal anisotropies have been carefully studied. Among others, they provide information on QGP viscosity, freeze-out temperature, symmetry plane, and primordial fluctuations. Additionally, distributions in $(\Delta\phi, \Delta\eta)$ have imprints from various sources of correlations, including flow itself. However, the window to

anisotropies in pseudorapidity is still much narrower than that to transverse geometries. In light of this fact, the next chapter presents a way of quantifying (θ, ϕ) pairs. Then, this alternate formalism is brought to the analysis of particle distributions originating from nuclei collisions, where pseudorapidity coordinates shall be changed to the polar angles through $\theta = 2\arctan(e^{-\eta})$.

3 On the Power Spectrum

"We are engaged in a poker game with Nature where it calls all the bluffs."

— Anonymous

Given a stochastic process, it is possible to probe its patterns and correlation structures via a power spectral density, that is, the decomposing of its defined signals into sinusoidal components [59, 60]. In this chapter, we introduce the idea of a power spectrum for a 1-D function, defined from the latter's Fourier expansion. We then extend to functions on a sphere, thus arriving at the definition of an *angular* power spectrum. Lastly, we present how the latter is used in cosmology to extract information on the physics of the primordial universe.

3.1 The 1-D case

Consider an arbitrary continuous function $f : x \mapsto f(x)$ defined on the interval $[\alpha, \beta]$, with $2L = \beta - \alpha$ as its size. Given that $\sin(k\pi x/L)$ and $\cos(k\pi x/L)$ are $2L$ periodic and form an orthogonal basis, $f(x)$ may be

expanded in a Fourier series:

$$f(x) = \frac{1}{2}a_0 + \sum_{k=1}^{\infty} a_k \cos\left(\frac{k\pi x}{L}\right) + \sum_{k=1}^{\infty} b_k \sin\left(\frac{k\pi x}{L}\right) \tag{3.1}$$

with coefficients

$$\begin{aligned} a_0 &= \frac{1}{L}\int_{\alpha}^{\beta} f(x)dx, \\ a_k &= \frac{1}{L}\int_{\alpha}^{\beta} f(x)\cos\left(\frac{k\pi x}{L}\right)dx, \\ b_k &= \frac{1}{L}\int_{\alpha}^{\beta} f(x)\sin\left(\frac{k\pi x}{L}\right). \end{aligned} \tag{3.2}$$

Note that Eq. (3.1) is yet another way of writing Eq. (2.3).

A Fourier series also possess a complex form: using Euler's relation $e^{ix} = \cos x + i \sin x$ in Eq. (3.1) yields

$$f(x) = \sum_{k=-\infty}^{\infty} c_k e^{ik\pi x/L}, \tag{3.3}$$

where $c_k \in \mathbb{C}$ is given by

$$c_k = \frac{1}{2L}\int_{\alpha}^{\beta} f(x)e^{-ik\pi x/L}dx. \tag{3.4}$$

The latter defines the *Power Spectrum* $P(k) \equiv |c_k|^2$, a quantity that describes the amplitude of a signal, represented here by $f(x)$, as a function of its frequency k; signal refers to information about the behavior of a system [61]. Alternatively, one may say that the power spectrum indicates the presence of patterns in $f(x)$.

A signal of constant frequency may be represented by the function $f(x) = \sin(4x)$. Note how its power spectrum on the right of Fig. 3.1

show a non-trivial value only at $k = 4$, indicating the only sinusoidal function that contributes to describing $\sin(4x)$. Unsurprisingly, the signal represented by $\sin(x) + 3/2 \cdot \cos(9x)$ has an associated $P(k)$ with non-trivial $k = 1$ and $k = 9$ modes. The latter is higher valued due to the amplitude associated with its frequency. Lastly, we give an example of a function not composed by sines and cosines, $f(x) = x^3 \cdot e^{-x^2}$: as its shape closely resembles that of $\sin x$, its power spectrum peaks at $k = 1$ while it dampens on higher frequencies. All functions were taken in the interval $[-\pi, \pi]$ for simplicity.

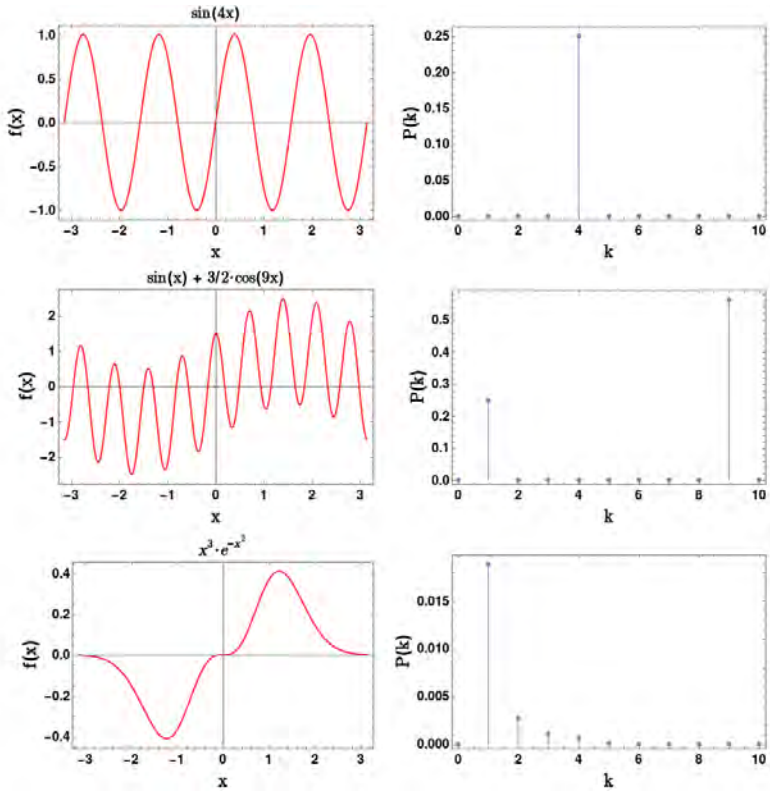

Figure 3.1: Examples of signals with function $f(x)$ and their respective power spectra $P(k)$.

The simple examples given above were but an introduction to what a power spectrum entails. In real life situations, signals can be buried in noise, as an unwanted disturbance, hence $P(k)$ being a useful tool in the identification of patterns and extraction of information. It can be used, for instance, to describe characteristics of musical instruments, of light sources and even of earthquakes [62].

In the limit as $L \to \infty$, the complex Fourier series presented above generalizes to the Fourier transform. Let $k/L \to \nu$ and substitute the discrete c_k coefficients by $F(\omega)$, then Eqs. (3.3) and (3.4) become:

$$f(x) = \int_{-\infty}^{\infty} F(\nu) e^{i2\pi\nu x} d\nu, \tag{3.5}$$

$$F(\nu) = \int_{-\infty}^{\infty} f(x) e^{-i2\pi\nu x} dx, \tag{3.6}$$

called inverse and forward Fourier transforms, respectively. The latter can also be denoted $F(\nu) = \mathcal{F}[f(x)](\nu)$.

Analogously to $P(k) = |c_k|^2$, we define the power spectrum in this new scenario as $\mathcal{P}(\nu) \equiv |F(\nu)|^2$. Explicitly,

$$|F(\nu)|^2 = F(\nu)\overline{F}(\nu) = \int_{-\infty}^{\infty}\int_{-\infty}^{\infty} f(x) f(x') e^{-i2\pi\nu(x-x')} dx dx'$$

$x - x' \to u$:

$$|F(\nu)|^2 = \int_{-\infty}^{\infty} \left[\int_{-\infty}^{\infty} f(x) f(x-u) dx \right] e^{-i2\pi\nu u} du = \mathcal{F}[f \star f](\nu), \tag{3.7}$$

where $f \star f \equiv \int_{-\infty}^{\infty} f(x) f(x-u) dx$ is the *autocorrelation* function, a tool commonly used to study stochastic processes. In brief, its Fourier transform is the power spectrum, or equivalently, the inverse Fourier transform of the power spectrum is the autocorrelation. This statement is known as the Wiener-Khinchin theorem [63].

If we were to calculate the power spectra of the functions in Fig. 3.1 through Eq. (3.7), the result would have yielded continuous functions like $\mathcal{P}(\nu) \propto (\delta(\nu-4)+\delta(\nu+4))$ in the case of $f(x) = \sin(4x)$, for example. Overall, $\mathcal{P}(\nu)$ is just the continuous case of $P(k)$, as expected. It is worth remarking that to calculate the autocorrelation function of $\sin(4x)$, the latter is taken as zero outside of the interval $[-\pi, \pi]$.

Fields of study such as astronomy, signal processing, statistics, have different interpretations on the meaning of correlation. In broad terms, it describes the relationship between variables of a system. When these are represented by the same function evaluated in different points, the measure of their connection is then called autocorrelation. For instance, imagine that $f(t)$ represents a sound changing with time t. Then $f(t-t_1)$ is that same sound displaced by a time interval t_1. After integrating their product over all possible t, the result should indicate whether there is a pattern in the signal or it is simply noise, i.e., random. Furthermore, the Fourier transform of the resulting autocorrelation should reveal the frequencies which compose said sound, if any.

3.2 The spherical case

Consider now an arbitrary function defined on the surface of a sphere $f : (\theta, \phi) \mapsto f(\theta, \phi)$, with the polar coordinate $\theta \in [0, \pi]$ and the azimuthal coordinate $\phi \in [0, 2\pi]$. Moreover, $f(0, \phi)$, $f(\pi, \phi)$ are independent of ϕ and $f(\theta, 0) = f(\theta, 2\pi)$. Analogously to the previous case, $f(\theta, \phi)$ can be expanded in a set of orthogonal functions denoted *spherical harmonics* $Y_{\ell m}$:

$$f(\theta, \phi) = \sum_{\ell=0}^{\infty} \sum_{m=-\ell}^{\ell} a_{\ell m} Y_{\ell m}(\theta, \phi), \tag{3.8}$$

where $a_{\ell m}$ are the complex coefficients of the expansion given by

$$a_{\ell m} = \int_{\Omega} f(\theta, \phi) Y^*_{\ell m}(\theta, \phi) d\Omega. \tag{3.9}$$

Additionally, m describes the angular orientation of a mode, while ℓ determines its characteristic angular size [64]. One may refer to ℓ as the *multipole moment*.

The spherical harmonics $Y_{\ell m}(\theta, \phi)$ are the angular part of the solution to Laplace's equation $\nabla^2 \psi = 0$ in spherical coordinates. Their explicit form is

$$Y_{\ell m}(\theta, \phi) = \sqrt{\frac{2\ell + 1}{4\pi} \frac{(\ell - m)!}{(\ell + m)!}} P_{\ell m}(\cos\theta)) e^{im\phi}, \tag{3.10}$$

with

$$P_{\ell m}(\cos\theta) = \frac{(-1)^m}{2^\ell \ell!} (\sin^2\theta)^{m/2} \frac{d^{\ell+m}}{d(\cos\theta)^{\ell+m}} (\cos^2\theta - 1)^\ell \tag{3.11}$$

as the associated Legendre polynomials for $m \geq 0$. The latter are defined for $m < 0$ as $P_{\ell -m}(\cos\theta) = (-1)^m [(\ell - m)!/(\ell + m)!] \cdot P_{\ell m}(\cos\theta)$.

It is worth noticing that the role occupied by wave functions in the 1-D case is taken by shapes like in Fig. 3.2, which depicts the real part of spherical harmonics for $\ell = 0, \cdots, 3$ and $m = 0, \cdots, 3$. The imaginary part of harmonics with $m = 0$ is null, otherwise rotating the real $Y_{\ell m}$ counterclockwise by $\pi/(2m)$ will get their imaginary part. Similarly to the Fourier case, a function $f(\theta, \phi)$ defined on the sphere can be represented by the superposition of the modes shown in Fig. 3.2 associated with their respective coefficients $a_{\ell m}$.

A straightforward way of picturing the geometry represented by ℓ and m is thinking of them as partitions through the sphere: while ℓ determines the total number of sections, m will indicate how many of those

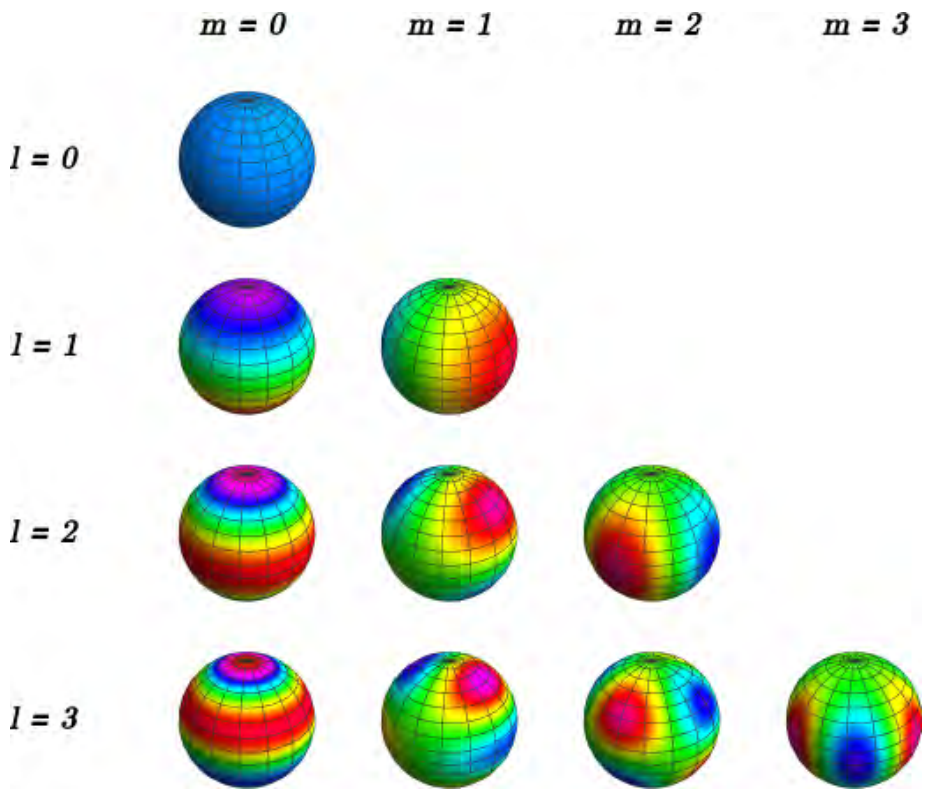

Figure 3.2: Real part of spherical harmonics.

should be across meridians (along θ coordinate); the remaining sections cut the sphere through parallels (along ϕ coordinate). For instance, $m = 0$ modes will have partitions only across parallels, with $\ell = 1$ having one division, $\ell = 2$, two and so forth. Besides, each partition will alternate between having a peak and a valley. Note in Fig. 3.2 how modes with $m = 0$, as a consequence, have rotational symmetry around the poles. Fig. 3.3 aids in visualizing the aforementioned partitions for some m in the case where $\ell = 6$.

In regards to functions decomposed in Fourier modes like Eq. (3.3), it is possible to quantify their amplitude as it varies with frequency k

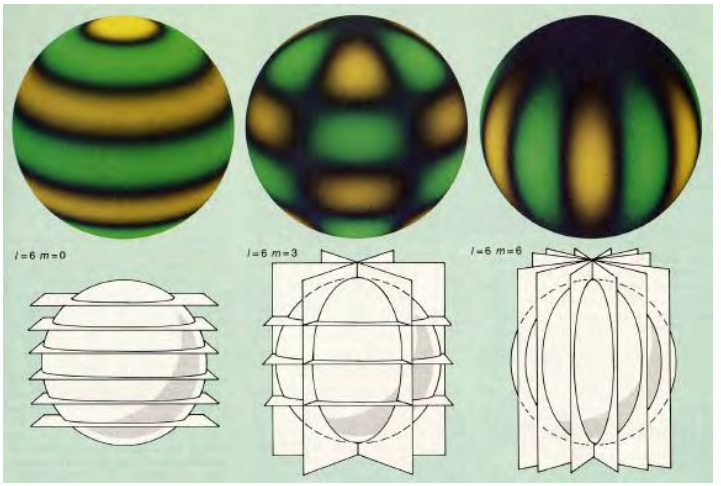

Figure 3.3: Spherical harmonics as partitions through a sphere. Picture from [65].

through $P(k)$; previously seen in Fig. 3.1. Likewise, for $f(\theta, \phi)$, one may introduce the *Angular Power Spectrum*, C_ℓ, defined as

$$\langle a_{\ell m} a^*_{\ell' m'} \rangle = \delta_{\ell\ell'} \delta_{mm'} C_\ell, \tag{3.12}$$

$$\text{or } C_\ell = \frac{1}{2\ell + 1} \sum_{m=-\ell}^{\ell} |a_{\ell m}|^2, \tag{3.13}$$

the variance of $a_{\ell m}$ coefficients for a given ℓ. It is a function of multipole moment, as opposed to the wave number k from the previous case.

The angular correlation function is the average product of $f(\theta, \phi)$ with itself sampled over all possible spatial points, or $\langle f(\theta, \phi) f(\theta', \phi') \rangle$. Using Eqs. (3.8, 3.12) it can be explicitly written as

$$\begin{aligned}\langle f(\theta,\phi)f(\theta',\phi')\rangle &= \sum_{\ell m}\sum_{\ell' m'}\langle a_{\ell m}a^*_{\ell' m'}\rangle Y_{\ell m}(\theta,\phi)Y^*_{\ell' m'}(\theta',\phi') \\ &= \sum_{\ell=0}^{\infty} C_\ell \sum_{m=-\ell}^{\ell} Y_{\ell m}(\theta,\phi)Y^*_{\ell m}(\theta',\phi') \\ &= \frac{1}{4\pi}\sum_{\ell=0}^{\infty}(2\ell+1)C_\ell P_\ell(\cos\theta), \end{aligned} \tag{3.14}$$

where the relation $\sum_{m=-\ell}^{\ell} Y_{\ell m}(\theta,\phi)Y^*_{\ell m}(\theta',\phi') = (2\ell+1)/(4\pi)P_\ell(\cos\theta)$ was employed, with P_ℓ as the Legendre polynomials. Furthermore, note how the equation above is similar to the Fourier series in Eq. (3.1). Summing up, the angular power spectrum describes the (θ_i, ϕ_i) pair correlation in Fourier space.

Throughout this work, the terms two-point or two-particle correlation function will substitute autocorrelation, as they are more commonly used in the field of heavy ion collisions.

3.3 A real life example

Signals originated from sources like sound waves and electric circuits may have their information extracted through Fourier decomposition and the computation of $P(k)$. However, in the study of higher dimensional structures like atomic orbitals or black holes, the expansion in spherical harmonics has a bigger appeal. The quintessential example of using such tools to analyze physical phenomena consists in the study of the Cosmic Microwave Background radiation, or CMB for short. Being the oldest picture of the universe at around 380,000 years old, it is composed of photons that escaped recombination: as electrons were bound to nuclei, forming the very first atoms, their interactions with photons became rarer, allowing them to stream freely.

Ever since its discovery in the early 1960s [1], the CMB has been measured more and more accurately by missions such as the Cosmic Background Explorer (COBE) satellite [66], the Wilkinson Microwave Anisotropy Probe (WMAP) spacecraft [67] and the European Space Agency's Planck satellite [68]. The latter's CMB map is depicted in Fig. 3.4 (top) and it shows temperature fluctuations that carry information on the primordial seeds which would later evolve into the cosmic structure observed today. The CMB is usually mapped onto a Mollweide projection: it distorts shape while preserving proportions in area. As a temperature field on the surface of a sphere, it may be decomposed in spherical harmonics like Eq. (3.8). Consequently, one can compute its angular power spectrum, whose result is shown in Fig. 3.4 (bottom) as measured by the Planck Collaboration (red dots). It is important to remark that the quantity plotted on the y-axis of Fig. 3.4 (bottom) is $\ell(\ell+1)C_\ell/2\pi$.

The angular power spectrum of the CMB depicts its temperature fluctuations as a function of the angular scale, a quantity related to the multipole moment through $\sim 180^o/\ell$. That means large scale structures correspond to low ℓ-modes, while smaller scales connect to high ℓ. The green curve shown in Fig. 3.4 represents the best fit of the current standard model of cosmology to Planck data.

The monopole ($\ell = 0$) and dipole ($\ell = 1$) moments of the temperature map in Fig. 3.4 (top) correspond, respectively, to the mean CMB temperature at $T = 2.73$ K and a Doppler beaming caused by the relative motion of the solar system to the CMB. The angular power spectrum's main features for $\ell \geq 2$ are its seemingly constant values at large scales ($\ell \lesssim 20$), its acoustic peaks and their relative sizes and its damping tail at quite large ℓ. These are understood mainly as resulting from the dynamics at play in the early universe, which involved three key ingredients: gravity, thermodynamics and fluid dynamics.

Inflation stretched quantum fluctuations originated from the Big Bang to cosmic scale. These generated gravitational potentials which

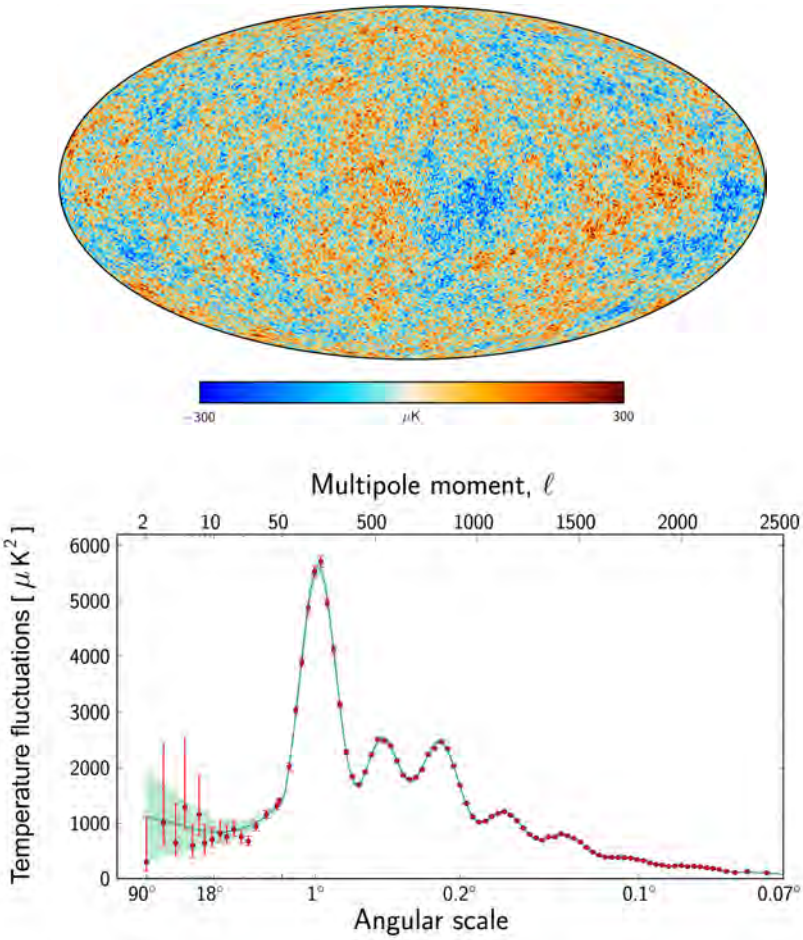

Figure 3.4: CMB map (top) and its angular power spectrum (bottom) as measured by the Planck Collaboration. Pictures from [69] and [70], respectively.

were dominated by dark matter and steadily evolving. As temperatures cooled below the binding energies of nuclei, the universe became permeated by a hot ionized fluid, basically a baryon-electron plasma strongly coupled to photons. The latter's mean free path was quite

small, as they constantly interacted electromagnetically and via Compton scattering. This primordial plasma would sit in gravitational wells, with photons exerting radiation pressure outwards, while gravity would compress the fluid; a tug-of-war that caused acoustic oscillations, or sound waves [71]. As the temperature dropped below $3,000\,\mathrm{K}$, electrons bound to nuclei forming neutral atoms and allowing photons to travel freely over long distances, carrying with them the intricate patterns of the last scattering.

Sound horizon is characterized by how far the longitudinal waves resultant from plasma oscillations could travel before recombination. Having said that, imagine regions separated by distances larger than the aforementioned: since the sound waves of one cannot reach the other before last scattering, anisotropies observed at such scales should still be remnants of even earlier times, presumably inflation. As it stands, they reflect the initial conditions of the universe.

The hot and cold spots in the CMB represent regions of plasma compression and rarefaction, respectively. In that same note, modes that were caught at the extrema of their oscillations, either in a gravitational well or hill, became the so called acoustic peaks of the CMB spectrum (see bottom of Fig. 3.4) and they form a harmonic series based on the sound horizon. The first peak on the spectrum corresponds to modes that managed to just reach maximum compression before photon decoupling. Modes on the second peak compressed and rarefied, on the third they compressed, rarefied and compressed, and so on. In brief, odd peaks represent maximum compression, while even peaks, maximum rarefaction [71].

The position of the first peak is consistent with a flat universe. The size of the sound horizon at recombination was found to be about 0.9^o, or $\ell \approx 200$ [72]. Then if the universe has positive or negative curvatures, the peaks would be respectively shifted left or right of said position: since light would not propagate in straight lines, the CMB anisotropies would appear bigger or smaller than they currently are. The ratio between

matter density and radiation mainly influences the overall height of the peaks. High baryon density loads the gravitational wells, thus increasing the amplitude of oscillations and making compression stronger than rarefaction. Consequently, odd peaks become enhanced relative to even ones as clearly seen in the difference between the first and second peaks. Dark matter also contributes to such characteristic, since it fixes the gravitational potentials. In a radiation-dominated scenario, however, the outwards pressure would cause the potentials to eventually decay, making the amplitude of peaks hierarchical. Therefore, the relative height of the third peak to the second one suggests that dark matter dominates the universe at recombination [73].

The amplitude of acoustic oscillations rapidly decreases with higher ℓ, as seen in Fig. 3.4 (bottom). The reason being that the scale of these fluctuations is comparable to the mean free path of photons during recombination. As the latter diffuse, regions of over and underdensity mix, thereby equalizing temperatures and making the CMB more uniform; this effect was first described in [74]. Since increasing baryon density implies in shortening the photons mean free path, the damping tail may also provide information on the matter composition of the early universe.

The CMB takes part in the body of evidence supporting the expanding hot Big Bang paradigm of cosmology. The former's angular power spectrum provides constraints to parameters of the cosmological standard model, also denoted ΛCDM. For instance, the densities of dark and baryonic matter, the angular scale of the acoustic fluctuations and even the age of the universe were further measured by the Planck Collaboration [75].

This last section served as an illustration of the physics driving the early universe and its impact on the CMB power spectrum. From this point on, the focus will be again on heavy ion collisions, as this study delves into spherical projections of emitted particles, the computational and detector issues that may arise and, finally, the estimation of C_ℓ asso-

ciated with the formation and evolution of the quark-gluon plasma.

4 Data and Tools: Towards a Method

"Ph'nglui mglw'nafh Cthulhu
R'lyeh wgah'nagl fhtagn."
— H.P. Lovecraft, *The Call of Cthulhu*

A plethora of phenomena are encoded in the distribution of particles emitted from a collision of heavy nuclei. An angular power spectrum quantifies (θ, ϕ) pair correlations, thus finding patterns in a spherically projected function. In this chapter we briefly present the ALICE subdetectors involved in measuring the data, as well as the pixelation software used in the analysis. Then we employ toy Monte Carlo simulations to tackle the possible issues arising from both, finally building a method to estimate the angular power spectrum of heavy ion collisions.

4.1 Event selection with ALICE

A Large Ion Collider Experiment, or ALICE, is one of the detectors at CERN LHC. It focuses on the study of QCD matter at high energy densities and temperatures. Aside from colliding Pb ions, it also runs lighter nuclei, proton-nucleus and proton-proton. The data set sample used in this thesis is a result of Pb-Pb collisions at energy $\sqrt{s_{NN}} = 2.76$ TeV per nucleon pair. It belongs to Run1 of 2010 and it comes from the ALICE-

CERN Open Data portal [9]. The main subdetectors utilized in this analysis are the Inner Tracking System (ITS), the Time Projection Chamber (TPC) and the VZERO (V0) detectors. They are all depicted in Fig. 4.1, a schematic layout of ALICE.

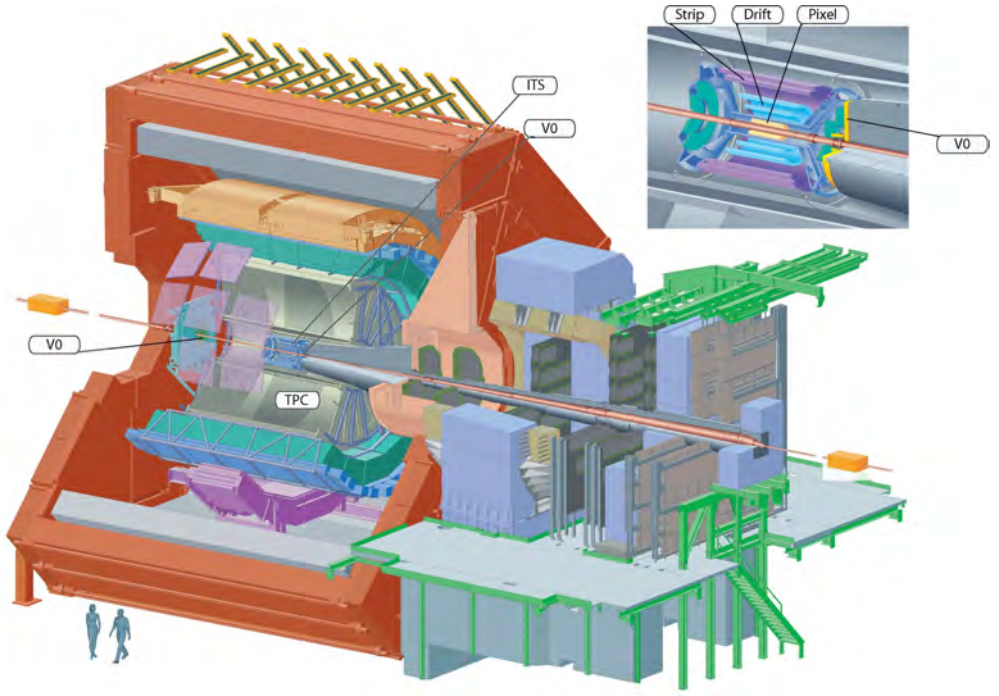

Figure 4.1: Schematic view of ALICE with analysis subdetectors highlighted. Image from [76] with labels from [77].

The ITS [78], as its name suggests, is the innermost detector of ALICE. From the inside out, it has two cylindrical layers of Silicon Pixel Detectors (SPD), two of Silicon Drift Detectors (SDD) and two of Silicon Strip Detectors (SSD); they can be seen on the upper right of Fig. 4.1. The main tasks of the ITS are to locate the primary and secondary vertices, i.e., where the collision takes place and produced hadrons decay, in addition to tracking and identifying particles with $p_T < 0.2$ GeV, and

improving momentum and angular resolution of particles reconstructed by the TPC [79]. It covers the $|\eta| < 0.9$ range.

The main tracking device of ALICE, the TPC [80], is filled with a Ne-CO_2-N_2 gas mix, which ionizes when particles cross it. The electrons emitted from such reactions provide 3-D information on the particles trajectories as well as their energy loss. It has total azimuth coverage, $|\eta| < 0.9$ in pseudorapidity and $0.1 < p_T < 100$ GeV in transverse momentum. The TPC can also provide information on a particle's identity and collision centrality.

The V0 detector [81] consists of two arrays of scintillator counters, denoted V0A and V0C [79], which are depicted, respectively, on the left and right sides of the ITS; see Fig. 4.1. They are asymmetrically placed with respect to the nominal interaction point, making them differ in η coverage: for the V0A, $2.8 < \eta < 5.1$, while for V0C, $-3.7 < \eta < -1.7$. Among its several functions, the V0 detector can differentiate between beam-beam interactions and background events, thus providing a minimum-bias trigger. Due to particles registered on the V0 having a monotone relation to primary ones, the detector also indicates centrality.

In this work, both the extraction of ALICE heavy-ion data and the event selection with its default cuts were performed through the repository in [10]. Firstly, the algorithm checks if each event has a reconstructed primary vertex and whether it lies within 10 cm of the detector's center. Secondly, it requires that multiplicity is non-zero. Lastly, in order to select high efficiency hadronic events, a minimum-bias trigger is fired and two of the subsequent conditions must be met: two pixels hit in the SPD's outer layer, a signal in V0A, a signal in V0C [82].

The combination of all mentioned ALICE subdetectors creates a snapshot of the collision right after kinetic freeze-out. The ITS and TPC reconstruct tracks of charged particles, measuring their spatial coordinates and momentum. The V0 and SPD provide a trigger to identify usable events, i.e., those coming from the collision itself, in opposition to particles generated through interactions in the vacuum chamber. At

last, it should be mentioned that the phase space coverage of the data set in this work is $|\eta| < 0.9$, $0.15 < p_T < 100$ GeV and $0 \leq \phi < 2\pi$.

4.2 About HEALPix

The distribution of emitted particles, as already mentioned in Ch. 2, can be represented by a function $f(\eta, \phi, p_T)$. This work proposes a change of coordinates from pseudorapidity to polar angle through the expression $\theta = 2\arctan(e^{-\eta})$; from this point onward, $f(\eta, \phi, p_T) \rightarrow f(\theta, \phi, p_T)$. Furthermore, it was discussed in Ch. 3 that functions defined on a sphere may be expanded in spherical harmonics. This section thus presents the software package HEALPix [83], which was used in the analysis of $f(\theta, \phi, p_T)$: from projecting it onto a sphere, to calculating $a_{\ell m}$ and C_ℓ.

The acronym HEALPix stands for **H**ierarchical **E**qual **A**rea iso**L**atitude **Pix**elation[1] and, as its name suggests, it makes subdivisions on a spherical surface, where each of these covers the same area, as shown in Fig. 4.2. As a result, data can be sampled without regional dependence.

In Fig. 4.2, the sphere on top-left has the lowest resolution; it is divided in 12 base pixels. Raising resolution to the next level (top-right) means subdividing the existing pixels into four more; see shaded area. This process continues from the bottom-right to bottom-left spheres and higher order subdivisions; hence the term hierarchical. Moreover, the pixels are located on lines of constant latitude, or θ. This ordering is essential for spherical harmonic analysis, since the computation of integrals scales with the total number of pixels, as $\sim N_{\text{pix}}^{1/2}$.

An analysis done in the HEALPix scheme should begin with choosing the adequate resolution, as to avoid signal smoothing; a discussion on that matter for heavy-ion data is a future subject. The parameter that

[1] https://healpix.sourceforge.io/

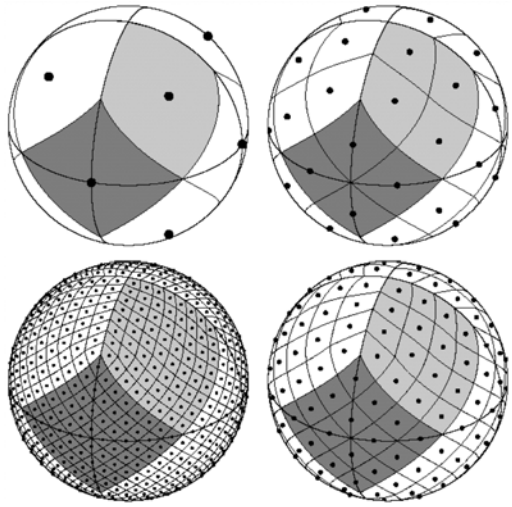

Figure 4.2: Pixelation of a sphere in four resolutions. Image from [83].

determines resolution is denoted N_{side} and given in powers of 2, once it represents the number of subdivisions on the side of the base pixel; note the shaded areas in Fig. 4.2. The total number of pixels relates to N_{side} through the expression $N_{\text{pix}} = 12N_{\text{side}}^2$, basically the number of subdivisions in each base pixel.

An array of unit vectors $\hat{\mathbf{n}} = (\theta, \phi)$, either coming from a data set or the sampling of a function $f(\theta, \phi)$, may be mapped onto the surface of a sphere. Each of its entries (j) will correspond to the pixel whose boundaries (θ_j, ϕ_j) falls within. As a result, a 2-D angular distribution becomes a 1-D array where pixels are indexed $p \in [0, N_{\text{pix}}]$ from north $(\theta = 0)$ to south $(\theta = \pi)$ along each consecutive isolatitude ring.

This resulting "sky" map $f(\mathbf{n_p})$ from the pixelation of a function $f(\hat{\mathbf{n}})$ can be thus decomposed in spherical harmonics, with $a_{\ell m}$ coefficients

estimated as a discretization of Eq. (3.9):

$$a_{\ell m} = \sum_{p=0}^{N_{pix}-1} \Omega_p f(\mathbf{n_p}) Y^*_{\ell m}(\mathbf{n_p}), \tag{4.1}$$

where $\Omega_p = 4\pi/N_{pix}$ is the standard pixel weight, i.e. their area, under the HEALPix scheme and $\mathbf{n_p} = (\theta_p, \phi_p)$ are the pixel center coordinates.

The spherical harmonics conventions of HEALPix consist of Eqs. (3.10, 3.11). Here the alignment of pixel centers in rings of same θ speeds up computations, since associated Legendre polynomials are evaluated once for each parallel. A Fast Fourier Transform is performed on ϕ [83]. It should also be remarked that, when $Y_{\ell m}$ are discretized, they form a linearly independent system up to a multipole value $\ell_{max} = 3N_{side} - 1$. Hence limiting the estimation of $a_{\ell m}$ and consequently of C_ℓ to ℓ_{max}; the angular power spectrum is calculated with Eq. (3.13).

Through HEALPix it is possible to create maps, or projections, of functions $f(\hat{\mathbf{n}})$ in addition to estimating their spherical harmonic coefficients $a_{\ell m}$ using Eq. (4.1). At this point we have the tools and knowledge on data features to finally build a method of angular power spectrum estimation for heavy ion collisions.

4.3 Software meets data

The angular distribution of particles $f(\theta, \phi)$ reconstructed by the ITS and TPC has a set of characteristics worth considering during power spectrum calculation: firstly, the limit imposed on η (θ) by the aforementioned subdetectors, secondly, the non-uniformity of azimuthal acceptance and lastly, the effect caused on C_ℓ by the typical event multiplicities. This section aims at tackling the issues arising from said data features by using toy Monte Carlo simulations under the same conditions. Moreover, the resulting power spectra are compared to their expected values, which are analytically calculated with Eqs. (3.9, 3.13). At

the end, there is a discussion on the choice of resolution N_{side} associated with the number of pixels per map.

4.3.1 Spectrum under a mask

The acceptance of a detector may be represented by a function of polar and azimuthal angles $W(\hat{\mathbf{n}})$, also denoted *mask*. In a scenario with perfect detector coverage, $W(\hat{\mathbf{n}}) = 1$, $\forall \hat{\mathbf{n}}$. Accordingly, the experimentally observed final particle distribution $f_{obs}(\hat{\mathbf{n}})$ relates to the true one $f_{tru}(\hat{\mathbf{n}})$ via the expression $f_{obs}(\hat{\mathbf{n}}) = W(\hat{\mathbf{n}}) \cdot f_{tru}(\hat{\mathbf{n}})$.

For the measured data at hand, the full azimuth is covered while the polar coordinates are limited to $44^o \lesssim \theta \lesssim 136^o$. Consider $W(\hat{\mathbf{n}})$ within the mentioned boundaries unitary, though zero otherwise. After expanding $f_{obs}(\hat{\mathbf{n}})$ and $f_{tru}(\hat{\mathbf{n}})$ in spherical harmonics, their respective coefficients $a_{\ell m}$ and $\tilde{a}_{\ell m}$ are linearly correlated through the expression

$$a_{\ell m} = \sum_{\ell'} \sum_{m'=-\ell'}^{\ell'} \underbrace{\left[\int_{\Omega_\eta} Y_{\ell' m'}(\hat{\mathbf{n}}) Y^*_{\ell m}(\hat{\mathbf{n}}) d\Omega \right]}_{W^{\ell\ell'}_{mm'}} \tilde{a}_{\ell' m'}, \tag{4.2}$$

with Ω_η representing the region covered by the detector.

The matrix $W^{\ell\ell'}_{mm'}$ is depicted in Fig. 4.3 for a truncated multipole sum of Eq. (4.2) to $\ell_{max} = 47$. The harmonic coefficients $a_{\ell m}$ consist of 1-D arrays where each entry corresponds to an index pair ℓ, m, shown in Fig. 4.4: the value of m is fixed, while ℓ varies from $\ell = m$ to $\ell = \ell_{max}$. For instance, from position 0 to 47 the arrays are occupied by $a_{\ell 0}$ with $0 \leq \ell \leq 47$. Accordingly, from entry 48 to 94 are the $a_{\ell 1}$ values with $1 \leq \ell \leq 47$ and so forth. A change in resolution affects ℓ_{max}, resulting in the evaluation of a wider or smaller range of ℓ values.

As a consequence of how $a_{\ell m}$ arrays are arranged, each square of matrix $W^{\ell\ell'}_{mm'}$ in Fig. 4.3 represents a combination of m and m' values

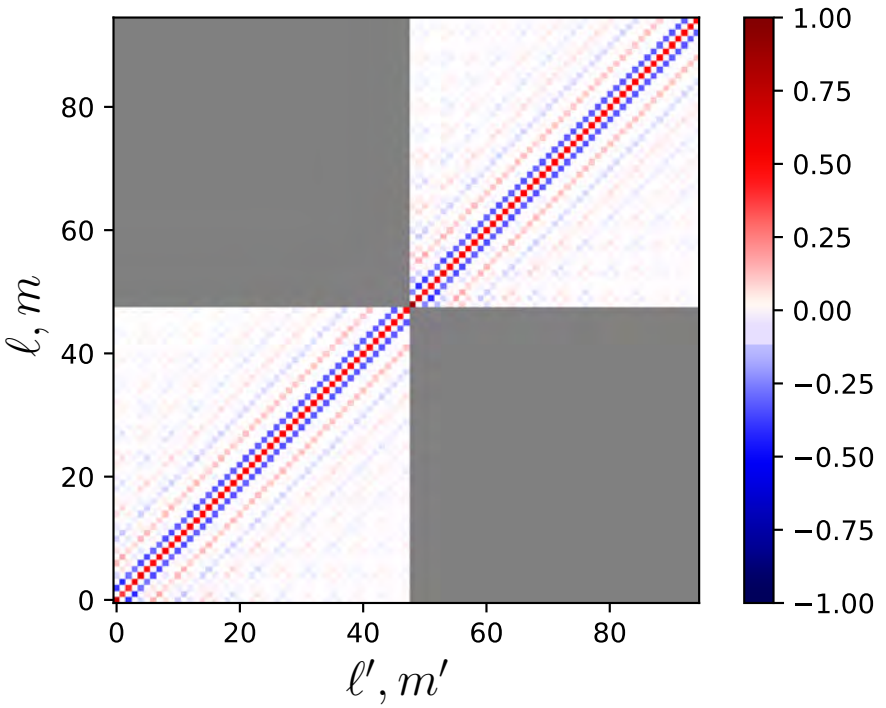

Figure 4.3: Coupling matrix $W^{\ell\ell'}_{mm'}$ for $m, m' = 0, 1$ associated with the mask $W(\hat{\mathbf{n}})$ in question for $\ell_{max} = 47$.

$$a_{\ell m} = \Big(\overbrace{0 \;\; 1 \;\; \cdots \;\; \ell_{max}}^{m=0} \;\; \overbrace{1 \;\; \cdots \;\; \ell_{max}}^{m=1} \;\; \cdots\Big)$$

Figure 4.4: Array representation of $a_{\ell m}$.

with their sides correspond to varying ℓ (vertical) and ℓ' (horizontal). The gray areas are equal to zero and depict $m' \neq m$. They were painted so in order to highlight where the azimuthal modes are equal.

Due to full coverage in ϕ, the integral in Eq. (4.2) selects solely $m' = m$. Furthermore, it can be seen in Fig. 4.3 that $W^{\ell\ell'}_{mm'}$ approaches zero with

increasing $\Delta\ell = |\ell' - \ell|$. Lastly, its chessboard-like pattern indicates that the matrix has non-trivial values only if ℓ and ℓ' have the same parity, i.e. they are either both odd or both even.

Since the determinant of $W^{\ell\ell'}_{mm'}$ is equal to zero, the linear system in Eq. (4.2) has no unique solution, making it impossible to recover $\tilde{a}_{\ell m}$ by straightforwardly inverting the mixing matrix. This is not a surprising result, as the data coverage corresponds to roughly 50% of the sphere surface thus implying a significant loss of information.

The method of estimating C_ℓ under a finite detector coverage was first proposed in [84] and is commonly referred to as *pseudo power spectrum estimator* or PCL. As it stands, the statistical properties of $a_{\ell m}$ and C_ℓ differ from their true counterparts $\tilde{a}_{\ell m}$ and $\tilde{C}_\ell$. The PCL method is discussed and applied to CMB analysis in [85, 86], where cosmological parameters may be estimated by maximizing a likelihood function of the pseudo C_ℓ. Alternatively, it is possible to bin the spectra at hand in ℓ, such that mixed modes would be within the same bin width.

This work aims at estimating the angular power spectrum of heavy ion collisions, so physical parameter calculations based on models are beyond its scope. Additionally, the final distribution of emitted particles is dominated by large scale anisotropies (flow coefficients), making C_ℓ for small ℓ prominent relative to higher modes [87]. Therefore, binning the spectra is not a viable step, as information on specific low ℓ values would be lost. Instead, a simpler approach is performed: we analyze the effects of $W(\hat{\mathbf{n}})$ on MC simulated distributions of different complexities, from fully isotropic to $f_{MC}(\hat{\mathbf{n}}) = g(\theta) \cdot h(\phi)$.

Before moving on, we should first remark on an important characteristic of data gathered from cosmic sources, like galaxy distributions or CMB: that our universe is a single realization of all possible observable ones. For this reason, nearly universe-sized fluctuations have few samples and, consequently, inconclusive statistical significance, whereas small scale structures yield a more considerable number of realizations. Translated into power spectrum vocabulary, an angular scale pertaining

to a certain ℓ will have $2\ell+1$ independent measurements for each spherical harmonic mode. The expected difference between the observed C_ℓ and the underlying ensemble average is termed *cosmic variance*. Its significance increases with lower ℓ.

In contrast, heavy ion collisions form an ensemble of events, as particle distributions are produced under controlled lab conditions. Their estimated angular power spectrum is, therefore, given by the ensemble average, i.e. $\langle C_\ell \rangle$. Furthermore, the error on the measurement may be simply calculated from the array of heavy ion observations itself, instead of estimating it from cosmic variance. Since this difference between CMB and heavy ion power spectrum analysis has been dully noted, we now tackle the effects of $W(\hat{\mathbf{n}})$ on $f(\hat{\mathbf{n}})$ when calculating C_ℓ.

In the case of isotropic particle distributions ($f_{iso}(\hat{\mathbf{n}}) = const.$), it is straightforward to see that, under full angular coverage, the only non-trivial harmonic coefficient is $\tilde{a}^{iso}_{00}$. Substituting it in Eq. (4.2), yields only $a^{iso}_{\ell 0} = W^{\ell 0}_{00}\tilde{a}^{iso}_{00}$ non-zero, since $m' = 0$. Moreover, ℓ' and ℓ must share parity if $W^{\ell\ell'}_{mm'} \neq 0$. Given that $\ell' = 0$, the only surviving coefficients for isotropic distributions under $|\eta| < 0.9$ coverage are $a^{iso}_{\ell 0}$ with ℓ even.

The aforementioned result for the power spectrum of isotropic distributions under limited coverage is depicted in Fig. 4.5. Around 8000 events were generated, each with multiplicity $1400 \lesssim M \lesssim 1800$ within $|\eta| < 0.9$, roughly corresponding to the 10-15% most central events at 2.76 TeV collision energy. The estimated $\langle C_l \rangle$ is the ensemble average over the spectra of each event map with resolution $N_{side} = 16$. The error bars pertain to the standard deviation. Also, the monopole value is fixed at $C_0 = 4\pi$, a consequence of Eq. (4.1) and the normalization factor N_{pix}/M applied to each event map before spectral calculation. This proceeding is repeated for all data sets in this work.

The zig-zag feature in Fig. 4.5 was expected due to only $a^{iso}_{\ell 0}$ with ℓ even contributing to C_ℓ. The enhancement of certain ℓ modes relative to the others is a direct result of the coverage percentage, as other $|\eta|$ ranges would change $W^{\ell\ell'}_{mm'}$, thus favoring different ℓ values [87]. Lastly, note

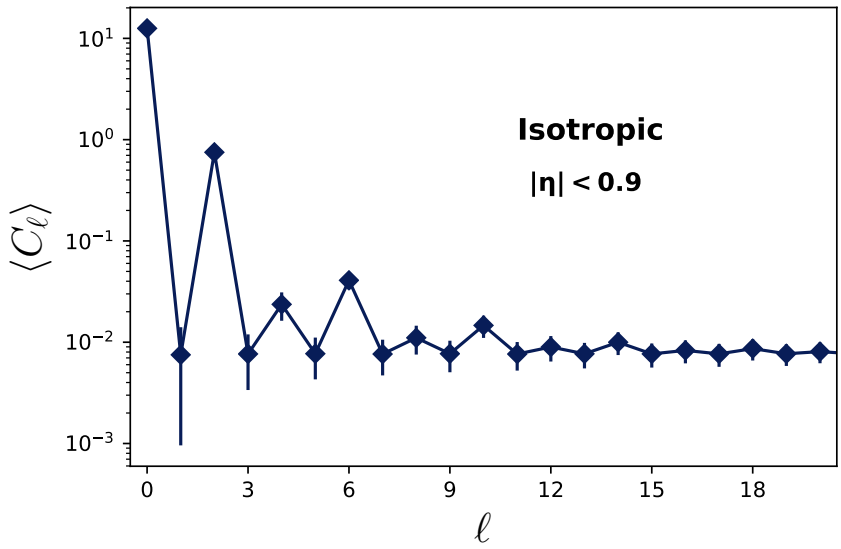

Figure 4.5: Averaged angular power spectrum of ~ 8000 isotropic distributions under $|\eta| < 0.9$ coverage.

how odd $\langle C_\ell \rangle \sim 7 \times 10^{-3}$, instead of being zero. This issue will be tackled soon, when we discuss the effects of typical heavy ion multiplicity on the estimation of the average spectrum.

Given how particles with no preferred direction of emission yield features on the resulting $\langle C_\ell \rangle$ in the presence of $W(\hat{\mathbf{n}})$, the next step consists on quantifying how the presence of anisotropies adds up to the averaged spectrum. Hence distributions like $f_{MC_1}(\hat{\mathbf{n}}) = h(\phi)$ and $f_{MC_2}(\hat{\mathbf{n}}) = g(\theta)h(\phi)$ being the focus of the following subsections.

The overlapping geometry of colliding nuclei plus fluctuations in the initial conditions are imprinted in the resulting particle distribution, as previously discussed in Ch. 2. The azimuthal anisotropy is then quantified through the flow coefficients v_n of a Fourier expansion. Inspired by this ansatz, the following simulated MC distributions are factorizable functions $f_{MC}(\hat{\mathbf{n}}) = g(\theta)h(\phi)$ with $h(\phi)$ given by the right side of

Eq. (2.3) divided by 2π. Considering full angular coverage and substituting $f_{MC}(\hat{\mathbf{n}})$ in Eq. (3.9) yields the harmonic coefficients:

$$\tilde{a}_{\ell m} = \begin{cases} \tilde{b}_{\ell 0} & \text{for } m = 0 \\ \tilde{b}_{\ell m} \cdot v_{|m|} e^{-im\Psi_{|m|}} & \text{for } m \neq 0 \end{cases} \tag{4.3}$$

with

$$\tilde{b}_{\ell m} = N_{\ell m} \int_0^{\pi} g(\theta) P_{\ell m}(\cos\theta) \sin\theta d\theta, \tag{4.4}$$

where $N_{\ell m}$ is the square root coefficient of $Y_{\ell m}$, depicted in Eq. (3.10). Note how only flow coefficients v_n with $n = |m|$ contribute to $\tilde{a}_{\ell m}$.

The two types of simulated data, dubbed MC_1 and MC_2, differ in their $g(\theta)$ expressions: while the first is constant in θ, the second follows a function with its global minimum in $\theta = \pi/2$, inspired on measured charged-particle pseudorapidity densities [88]. Over the full η range, the η-distribution is symmetric around $\eta = 0$, which is equivalent to $\theta = \pi/2$. A change of variable from η to θ on the pseudorapidity density plots depicted in [88] yields a function of the polar angle analogous to the one in Fig. 4.6; the limited $44^o \lesssim \theta \lesssim 136^o$ ($|\eta| < 0.9$) detector coverage is represented by $\Delta\theta_\eta$.

So $f_{MC_1}(\hat{\mathbf{n}})$ is isotropic in θ and $f_{MC_2}(\hat{\mathbf{n}})$ follows the polar function in Fig. 4.6. As a result, a new feature has to be considered in their expressions for $\tilde{a}_{\ell m}$: in both cases $g(\theta)$ is even around $\pi/2$ within the interval $[0, \pi]$. As $\sin\theta$ has the same property, $\tilde{b}_{\ell m}$ in Eq. (4.4) will be non-trivial according to the parity of $P_{\ell m}$. The associated Legendre polynomials are *even* when ℓ, m have *same* parity and *odd* when ℓ, m have *opposite* parities. Consequently, $\tilde{b}_{\ell m} \neq 0$ if, and only if, ℓ, m are either both even or both odd.

The objective at this point consists in quantifying the effects on the harmonic coefficients and power spectra of both $f_{MC_1}(\hat{\mathbf{n}})$ and $f_{MC_2}(\hat{\mathbf{n}})$ under the mask $W(\hat{\mathbf{n}})$. For this reason, we reintroduce the index notation

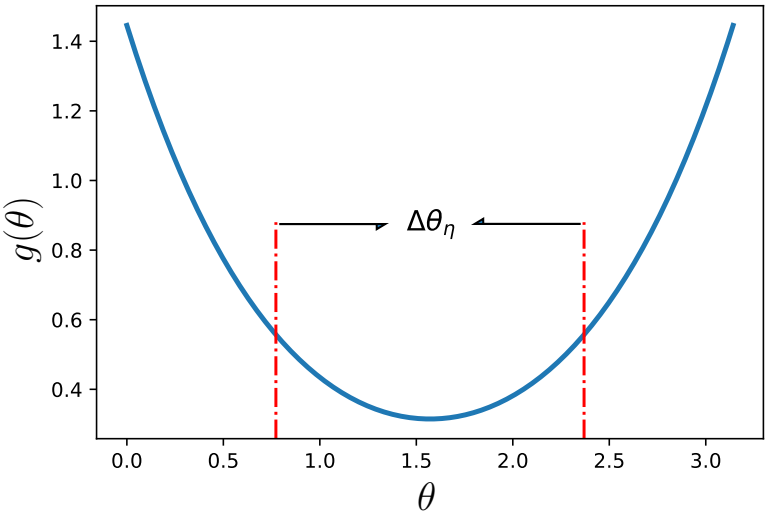

Figure 4.6: Polar function $g(\theta) \propto \cosh(0.5(\theta - \pi/2)) \cdot ((\theta - \pi/2)^2 + 1)$.

where ℓ, m correspond to the masked $a_{\ell m}$, while ℓ', m' represent the full coverage $\tilde{a}_{\ell' m'}$.

Let us begin by recalling the rules of the mixing matrix in Fig. 4.3: $W^{\ell\ell'}_{mm'} \neq 0$ when (i) $m' = m$ and (ii) ℓ', ℓ share parity. Due to (i), the sum in m' selects only $\tilde{a}_{\ell' m}$ - refer to Eq. (4.2). Furthermore, $f_{MC}(\hat{\mathbf{n}})$ being even around $\theta = \pi/2$ makes $\tilde{a}_{\ell' m} \neq 0$ only if ℓ', m share parity themselves. Combining that with (ii) results in ℓ, m having the same parity for the masked $a_{\ell m}$ be non-trivial. This paragraph can be visualized in Fig. 4.7, where the aforementioned consequence is highlighted in bold.

All in all, the masked harmonic coefficients $a_{\ell m} \propto v_{|m|} e^{-im\Psi_{|m|}}$, following Eq. (4.3), save for their $b_{\ell m}$ factors, which are a sum in ℓ' of $\tilde{b}_{\ell' m}$ given by Eq. (4.4). It is due to $W(\hat{\mathbf{n}})$ being uniform in ϕ, that there is no mixing of v_n and Ψ_n parameters in $a_{\ell m}$.

Once the features of $a_{\ell m}$ have been determined, it is time to generate the $f_{MC_1} = h(\phi)$ and $f_{MC_2} = g(\theta)h(\phi)$ themselves. Their azimuthal part

$$\underbrace{a_{\ell m}}_{\substack{\textbf{same}\\ \textbf{parity}}} = \sum_{\ell'} \overbrace{W_{mm}^{\ell\ell'}}^{\substack{\text{same}\\ \text{parity}}} \cdot \underbrace{\tilde{a}_{\ell' m}}_{\substack{\text{same}\\ \text{parity}}}$$

Figure 4.7: Parity relations between indices.

$h(\phi)$ has the sum in Eq. (2.3) truncated at $n = 6$. The v_n are constant with its values depicted in Table 4.1. As for the complex phase angles Ψ_n, they are randomly picked from an uniform distribution in the interval $[0, 2\pi)$. However, they do not affect C_ℓ, since it depends solely on $|a_{\ell m}|^2$.

v_1	v_2	v_3	v_4	v_5	v_6
0.02119	**0.05928**	**0.02636**	**0.01218**	**0.00520**	**0.00209**

Table 4.1: Values of v_n coefficients for $h(\phi)$.

The same number of events $N_{evts} \sim 8000$, each with the same multiplicities as in the isotropic case, are produced following the distributions $f_{MC_1}(\hat{\mathbf{n}})$ and $f_{MC_2}(\hat{\mathbf{n}})$. As previously mentioned, v_n have a fixed value, while Ψ_n are randomized event-by-event. Each sampled event is then projected onto a map with $N_{side} = 16$ and has its C_ℓ calculated. Finally their average is taken, yielding $\langle C_\ell \rangle$. Fixing N_{evts} and the individual event multiplicities when generating both isotropic and MC distributions guarantees that their spectra are compared under the same statistical conditions.

The monopole $C_0 = 4\pi$ has a fixed value for all event spectra, a result from the normalization N_{pix}/M imposed on each map. Said procedure will permeate throughout all power spectrum calculations in this work, so C_ℓ from distributions with different multiplicities and map res-

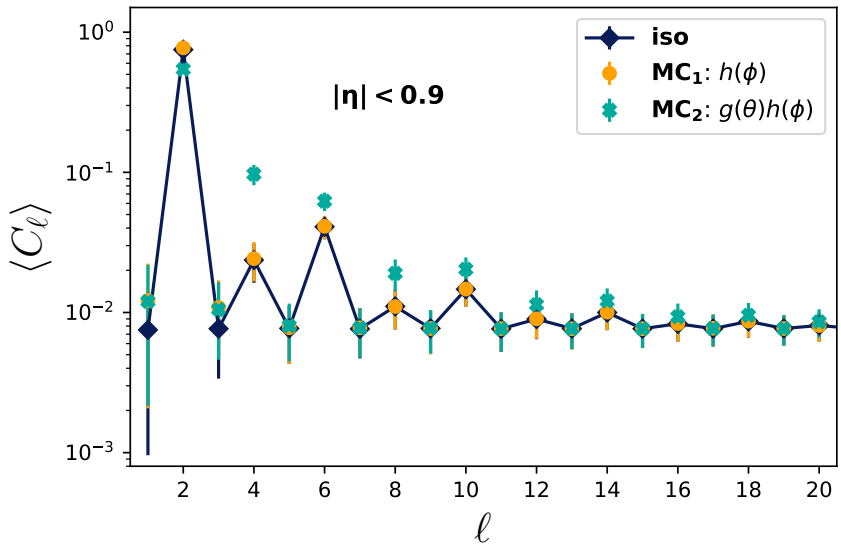

Figure 4.8: Averaged power spectra $\langle C_\ell \rangle$ for isotropic (iso), $f_{MC_1}(\hat{\mathbf{n}}) = h(\phi)$ and $f_{MC_2}(\hat{\mathbf{n}}) = g(\theta)h(\phi)$ distributions. It begins in $\ell = 1$.

olutions can be compared. An alternative normalization is to compute C_ℓ/C_0 instead, since the monopole is simply the integral of $f(\hat{\mathbf{n}})$ over the whole sphere.

An striking feature of the $\langle C_\ell \rangle$ comparison in Fig. 4.8 is how the averaged spectrum of MC_1 has seemingly the same values as the fully isotropic case, despite being dependent on ϕ. It should be remarked that, under full coverage, all $m = 0$ modes with $\ell > 0$ should disappear for MC_1, so its masked $a_{\ell 0}$ coefficients are equal to the iso ones. Therefore, Fig. 4.8 shows that, for even ℓ, $a_{\ell 0}$ actually holds the majority of power in the $|a_{\ell m}|^2$ sum that yields $\langle C_\ell \rangle$.

In order to visualize this predominance of certain modes, we produced a single event with 10^7 particles for each MC distribution with symmetry planes Ψ_n set to zero. Each event was then projected onto a map with resolution $N_{nside} = 64$; see the left side of Fig 4.9. The choice of

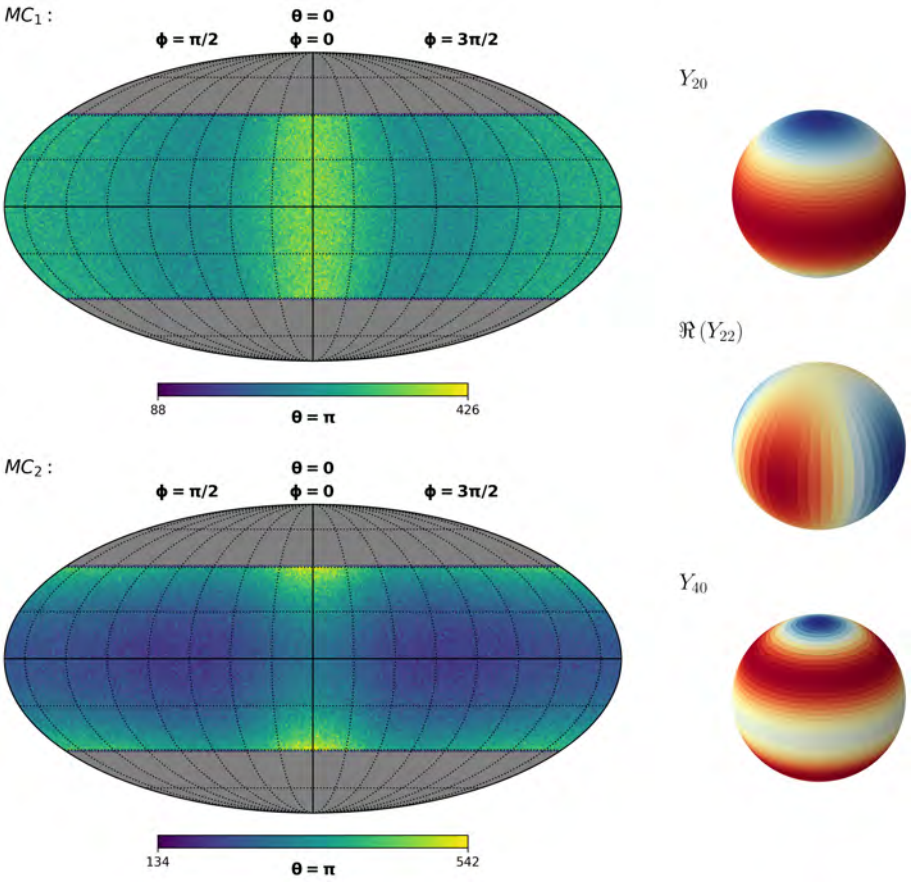

Figure 4.9: Left: maps of single events with 10^7 particles at $N_{side} = 64$ for both MC distributions. Right: some of the contributing spherical harmonics.

high multiplicity and N_{side} allows for clearly seeing the $f_{MC}(\hat{\mathbf{n}})$ functions that generated the maps. Also, the bars represent the number of particles in each pixel. The limited coverage is depicted in gray.

Firstly, note in Fig. 4.9 how the mask's geometry is akin to that of Y_{20}. The latter is characterized by two parallels, which mirror quite well the central strip of both MC maps. Consequently, a_{20} will have a rela-

tive high value in the harmonic expansions of both $f_{MC}(\hat{\mathbf{n}})$ compared to the other coefficients. This explains why $\langle C_2 \rangle$ (in all cases) stands above all other modes in Fig. 4.8. Secondly, observe how $\Re\mathfrak{e}(Y_{22})$ bears resemblance to the azimuthal shapes of both maps, where particles concentrate mostly around $\phi = 0$. As a result, a_{22} will also have a significant contribution in the harmonic expansions. However, $\langle C_2 \rangle_{MC_1} \sim \langle C_2 \rangle_{iso}$, making a compelling case of a_{20} surpassing by far all the other a_{2m} modes.

The presence of a symmetric θ function in $f_{MC_2}(\hat{\mathbf{n}})$ is responsible for its even $\langle C_\ell \rangle$ having different values compared to the other distributions. From Fig. 4.6, it can be seen that $g(\theta)$ causes particles to accumulate on the edges of the mask and makes a valley around the equator. For this, the map ends up with five subregions in θ, a characteristic shared with Y_{40} and shown in Fig. 4.9. The latter explains $\langle C_4 \rangle_{MC_2} > \langle C_4 \rangle_{MC_1}, \langle C_4 \rangle_{iso}$.

In contrast to their even $\langle C_\ell \rangle$, the odd modes for $f_{MC_1}(\hat{\mathbf{n}})$ and $f_{MC_2}(\hat{\mathbf{n}})$ seem to have the same values. A clear distinction to the isotropic case occurs only for $\ell = 1$ and $\ell = 3$, despite $h(\phi)$ carrying a v_5 contribution. This probably pertains to the low-multiplicity effects, an issue of the next subsection.

There is a plethora of evidence that $a_{\ell 0}$ for even ℓ are the greatest contributors to their $\langle C_\ell \rangle$ value. The enhancement of even modes with respect to odd ones, the proximity between isotropic and MC_1 spectra at even ℓ, and how the global map geometries mirror the even $Y_{\ell 0}$ harmonics. In light of these, a remarkably simple approach is proposed to visualize the anisotropies of both $f_{MC}(\hat{\mathbf{n}})$ [87]: the removal of all $a_{\ell 0}$ modes in the power spectrum calculation. There should be virtually no difference for the odd modes, since $a_{\ell 0} = 0$ for them. So, for each event map,

$$C_\ell^{m\neq 0} = \frac{1}{2\ell+1} \sum_{m=-\ell}^{\ell} |a_{\ell m}|^2 - \frac{|a_{\ell 0}|^2}{2\ell+1}. \tag{4.5}$$

The averaged power spectra $\langle C_\ell^{m\neq 0} \rangle$ for the isotropic, $f_{MC_1}(\hat{\mathbf{n}})$ and

$f_{MC_2}(\hat{\mathbf{n}})$ distributions are depicted in Fig. 4.10. For $\ell \leq 6$, it is finally possible to see a deviation from isotropy: both MC have a clear peak in $\ell = 2$, a consequence of v_2 being the highest valued flow coefficient; see Table 4.1. The $\ell = 1$ and $\ell = 3$ modes remain above the isotropic spectrum, which is now predominantly flat. The typical $\sim 7 \times 10^{-3}$ values are associated with the event multiplicities of the distributions at hand.

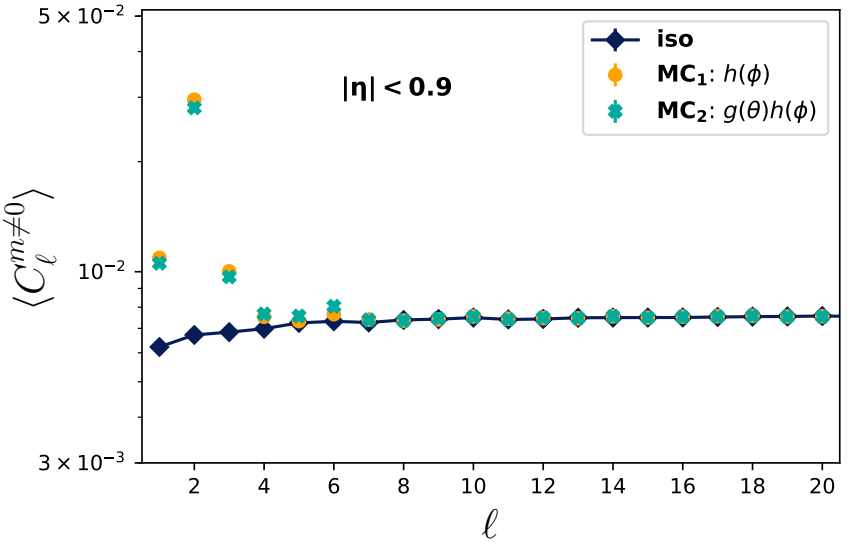

Figure 4.10: Averaged power spectra with $m = 0$ modes subtracted $\langle C_\ell^{m\neq 0} \rangle$ for isotropic (iso), $f_{MC_1}(\hat{\mathbf{n}})$ and $f_{MC_2}(\hat{\mathbf{n}})$ distributions.

The error bars in Fig. 4.10 correspond to the *standard error*, which measures the statistical accuracy of the $\langle C_\ell^{m\neq 0} \rangle$ estimation. In Fig. 4.8, the standard deviation of each $\langle C_\ell \rangle$ shows how they can vary significantly event-by-event. However, when the averaged spectra of different event populations from the same distribution are compared, they are equal (within the standard error) to each other. Since the interest of this work lies in estimating $\langle C_\ell^{m\neq 0} \rangle$, the standard error will be used as the error bar in all its plots from this point on.

Summing up, the $a_{\ell m}$ coefficients under limited detector coverage are a linear combination of the true underlying $\tilde{a}_{\ell m}$. The mixing matrix $W^{\ell\ell'}_{mm'}$ at hand causes Eq. 4.2 to be a system with no unique solution. For this reason, there was a necessity of quantifying the mask effects on the averaged power spectrum. Non-trivial even mode values were observed in isotropic distributions (Fig. 4.5) and they were found to be strikingly close to anisotropic ones (Fig. 4.8). Hence the introduction of $\langle C_\ell^{m\neq 0}\rangle$, which allowed the observation of a peak in $\ell = 2$ (Fig. 4.10), caused by the relatively high v_2 value.

Nevertheless, there is a caveat: the $\langle C_\ell^{m\neq 0}\rangle$ values calculated above for MC_1 and MC_2 are on average $\mathcal{O}(10)$ higher than the expected ones for $\ell \leq 6$. The following discussion will treat the effects of low multiplicity on the estimation of $\langle C_\ell^{m\neq 0}\rangle$ and propose a viable solution to get the right spectrum values.

4.3.2 A multiplicity issue

The Monte Carlo sampling of each event is a possible reason for the discrepancy between the observed $\langle C_\ell^{m\neq 0}\rangle$ and their expected values. The error on the approximation of an event distribution to $f(\hat{\mathbf{n}})$ propagates to its $a_{\ell m}$ estimation and, consequently, to its power spectrum. One could also think that resolution may contribute to this difference. After all, harmonic coefficient calculations involve the pixelation of their corresponding distributions $f(\hat{\mathbf{n}}) \rightarrow f(\mathbf{n_p})$, see Eq. (4.1). It has been observed, however, that map binning does not change the resulting $\langle C_\ell^{m\neq 0}\rangle$ significantly. This is the last item discussed in this chapter.

As a means of quantifying the typical multiplicity effect on the averaged power spectrum, 8000 isotropic events were generated for each multiplicity value ranging from $M = 100$ to $M = 5000$ and each of their $\langle C_\ell^{m\neq 0}\rangle$ were then calculated. These simulations were under the same $W(\hat{\mathbf{n}})$ mask as previous distributions and chosen resolution was $N_{side} =$

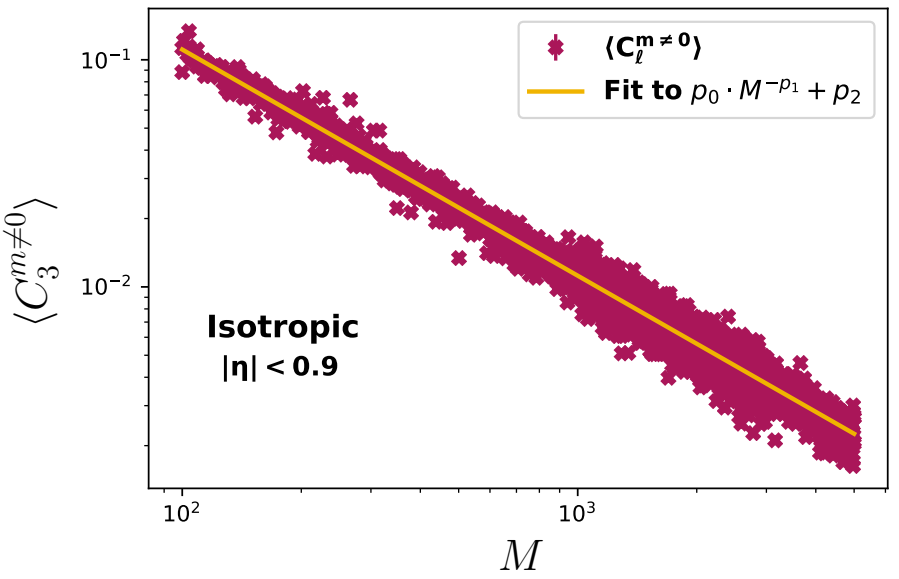

Figure 4.11: Example of how the averaged spectrum $\langle C_\ell^{m\neq 0} \rangle$ changes with typical event multiplicity.

16. The resulting $\langle C_\ell^{m\neq 0} \rangle$ as a function of M is depicted in Fig. 4.11 for $\ell = 3$.

Unsurprisingly, $\langle C_3^{m\neq 0} \rangle$ is inversely proportional to the event multiplicities. From Fig. 4.11, one can see that for $\langle C_3^{m\neq 0} \rangle = 7 \times 10^{-3}$, the corresponding range in M covers the input multiplicity values of the isotropic distributions which yielded Fig. 4.10. This same averaged spectrum behavior is seen for the remaining $\ell > 0$ modes. Furthermore, the dependence of $\langle C_\ell^{m\neq 0} \rangle$ on M follows a power law of the type $p_0 \cdot M^{-p_1} + p_2$, with $p_0, p_1, p_2 \geq 0$. Note that, as $M \to \infty$, $\langle C_\ell^{m\neq 0} \rangle \to p_2$, meaning that p_2 is the true averaged spectrum value at that ℓ. For $\langle C_3^{m\neq 0} \rangle_{iso}$ in Fig. 4.11, $p_2 = 0$.

For each ℓ, imagine that p_0 and p_1 are independent of the underlying distribution, i.e., $\langle C_\ell^{m\neq 0} \rangle_{MC}$ relates to M through $p_0 \cdot M^{-p_1} + p_2^{MC}$, where p_2^{MC} is the expected spectrum value of $f_{MC}(\hat{\mathbf{n}})$. In this case, find-

ing the latter would be quite simple: through a plot of isotropic spectra like Fig. 4.11, one could extract the fitting parameters p_0 and p_1 for each ℓ mode. Then, the true anisotropic MC spectrum would be estimated through $\langle C_\ell^{m\neq 0}\rangle_{MC} - \langle p_0 \cdot M^{-p_1}\rangle$, subtracting from the observed spectrum the power law factor averaged over all event multiplicities.

Alternatively to finding the fit parameters p_0, p_1, one may instead estimate a background spectrum at $m \neq 0$, here denoted $\langle N_\ell^{m\neq 0}\rangle$, based on the multiplicity distribution of the event ensemble. For instance, return to the population of isotropic distributions responsible for the spectra in Figs. 4.5, 4.10; it was composed of ~ 8000 events with $1400 \lesssim M \lesssim 1800$ each. The resulting flat $\langle C_\ell^{m\neq 0}\rangle_{iso}$ corresponds to the mean fluctuation size at all angular scales due to low MC sampling. Altogether, the simplest background spectrum associated to a data set coincides with the isotropic averaged spectrum for the ensemble multiplicities.

Once $\langle N_\ell^{m\neq 0}\rangle$ has been calculated, analogously to the procedure described above, the expected average power spectrum is estimated through $\langle C_\ell^{m\neq 0}\rangle - \langle N_\ell^{m\neq 0}\rangle$. The latter is motivated by how the signal-to-background ratio deviates from unity, $|\langle C_\ell^{m\neq 0}\rangle / \langle N_\ell^{m\neq 0}\rangle - 1|$. Notice that both expressions are related to each other by a factor of $1/\langle N_\ell^{m\neq 0}\rangle$. Throughout this work, $\langle S_\ell^{m\neq 0}\rangle = |\langle C_\ell^{m\neq 0}\rangle - \langle N_\ell^{m\neq 0}\rangle|$ will be used as the estimate of the true underlying spectrum.

The calculation of $\langle N_\ell^{m\neq 0}\rangle$ goes as follows: 10^6 isotropic events limited by $|\eta| < 0.9$ are generated with multiplicity values drawn according to the distribution at hand. For instance, if the latter is uniform, each M will have equal weight on the averaged power spectrum. The reason for $N_{evts} = 10^6$ lies in sampling a significant quantity of maps which correspond for a certain M value, since there are many variations on how the filled pixels could be distributed. This should increase precision and accuracy on the estimation of $\langle N_\ell^{m\neq 0}\rangle$ for each of the multiplicities.

The results of $\langle S_\ell^{m\neq 0}\rangle$ for both $f_{MC_1}(\hat{\mathbf{n}}) = h(\phi)$ and $f_{MC_2}(\hat{\mathbf{n}}) = g(\theta)h(\phi)$ are shown in Fig. 4.12, subplots (a) and (b) respectively. They are compared to the analytical power spectrum calculation $\mathtt{C}_\ell^{m\neq 0}$ of their corre-

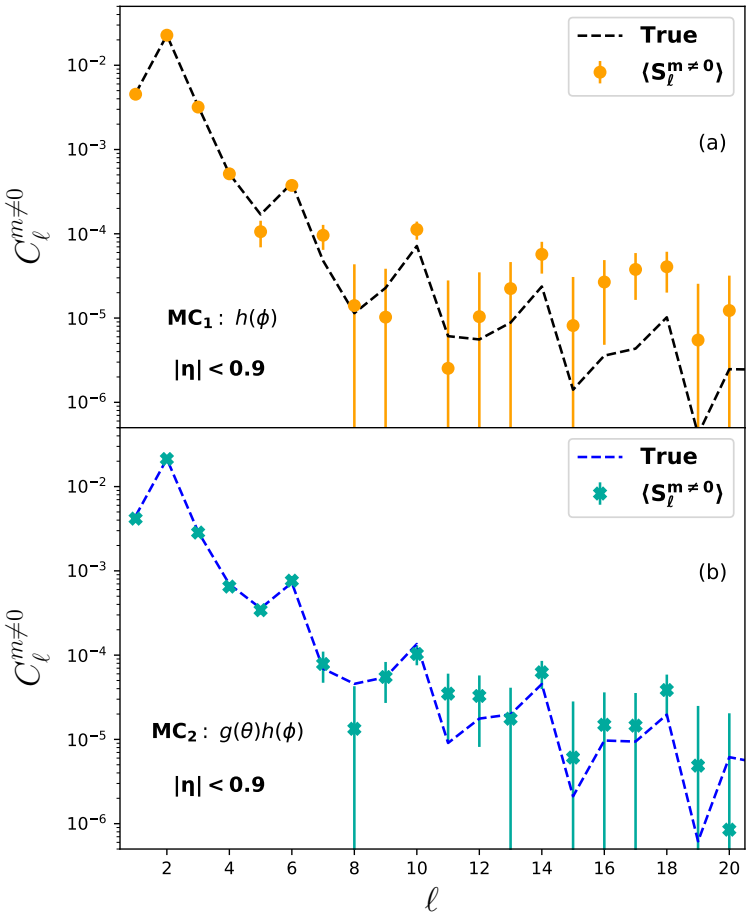

Figure 4.12: Comparison between estimated $\langle S_\ell^{m\neq 0}\rangle$ and analytically calculated spectra for both MC distributions within $|\eta| < 0.9$.

sponding functions through Eqs. (3.9,4.5), also under the $W(\hat{\mathbf{n}})$ mask; those are denoted as **True** in the aforementioned plot and they have $\Psi_n = 0$, $\forall n$, since $\mathtt{C}_\ell^{m\neq 0}$ only depends on $|a_{\ell m}|^2$.

The power spectrum values at $\ell = 1, 2, 3$ still remain enhanced relative to the rest, a feature already observed in Fig. 4.10. Also, what was

but a suggestion of a peak in $\ell = 6$, can now be clearly seen in Fig. 4.12. For the $\langle S_\ell^{m\neq 0}\rangle$ values corresponding to $\ell = n$, the difference to the true $\mathtt{C}_\ell^{m\neq 0}$ is less than 10% of it, save for MC_1 at $\ell = 5$, which is 38%. All in all, this procedure of background subtraction has managed to reproduce the expected spectrum remarkably well for $\ell \leq 6$.

As previously stated, the v_n coefficients at hand strongly influence the large scale structure of the final particle distributions. For instance, $\ell = 6$ roughly corresponds to an angular separation of $\sim 30^o$. Return to Fig. 4.9 and look at the MC maps: the meridians in their grids are 24^o apart, while for the parallels this number is 22.5^o. So, the scale of v_6 influence covers more than a full grid-square in a map. Beyond $\ell = 6$, the contribution of v_n becomes smaller and smaller, since $v_n = 0$ for $n > 6$. Adding that to the multiplicities of $\mathcal{O}(10^3)$ in each event and it gets trickier to estimate the true $\mathtt{C}_\ell^{m\neq 0}$ for $\ell > 6$.

Overall, $\langle S_\ell^{m\neq 0}\rangle$ for MC_2 lies closer to its expected value than MC_1 to its own, specially at higher ℓ. A possible explanation is that $g(\theta)$ allows particles to cluster more towards the edges, thus increasing their density in such regions and facilitating the calculation of $a_{\ell m}$ for smaller scales.

The geometry of $f_{MC_1}(\hat{\mathbf{n}})$ and $f_{MC_2}(\hat{\mathbf{n}})$ is purely dominated by flow. Their expected spectra are characterized by a periodicity with peaks at $\ell = 2k$, $k = 1, 3, 7, \cdots$, a feature followed by the $\langle S_\ell^{m\neq 0}\rangle$ estimations until $\ell = 10$. The limitations of the presented method depend on the underlying functions as well as the number of sampled particles per event. For the cases at hand, one could say that it cannot be relied on beyond a 18^o angular scale ($\ell = 10$). However, with more particles and higher v_n values or perhaps another distribution function, this boundary could be pushed towards $\ell > 10$. It could also decrease with lower multiplicities and v_n.

Summing up, it is possible to get around the multiplicity-caused effect by subtracting from the observed spectrum an estimated background. The latter is dependent on the M-distribution of the actual event population. For the discussed MC cases, $\langle N_\ell^{m\neq 0}\rangle$ coincided with

the averaged spectrum of isotropic maps with same multiplicities. In the next subsection, we see this is not always the case. Lastly, the method yields values which lie quite closely to the expected ones until a certain ℓ. Said limitation is mostly related to the underlying function and typical event multiplicity. Resolution could play a part in it, as well as N_{evts}, though its influence is tightly connected to M themselves.

4.3.3 Detector efficiency

Although all the spectra calculated so far were taken under the acceptance mask $W(\hat{\mathbf{n}})$, nothing has been discussed about detector efficiency. In other words, the simulations from the previous subsections mimic a ratio of measured to incident particles equaling one. In other to check the efficiency corresponding to the ALICE data set at hand [9], events from a selected centrality were superposed. Due to the orientation of each nuclei collision, the resulting angular distribution of all overlapping events is azimuthally uniform, while its shape in the polar direction resembles $g(\theta)$ from Fig. 4.6; the overall pseudorapidity density function is not flat [88].

The aforementioned sum of event maps is depicted in Fig. 4.13 for the 10-15% centrality. The angular differences between each parallel and meridian are 22.5^o and 24^o, respectively; just like in Fig. 4.9. As expected, particle density around the edges surpasses that of the equatorial regions. Conversely, the map is not smooth along the azimuthal direction, e.g., the dark patch between meridians at 96^o and 120^o. Some of the 18 TPC sectors can also be faintly seen.

The next step deals with uncovering these detector efficiency effects on the estimated power spectrum and how to tackle them. Yet again MC simulated distributions are in order. First, it is necessary to isolate the efficiency-caused anisotropies in Fig. 4.13 from the overall θ distribution, a task achieved by dividing them. The map of particles polar density is calculated by randomizing the ϕ coordinates of each event and summing

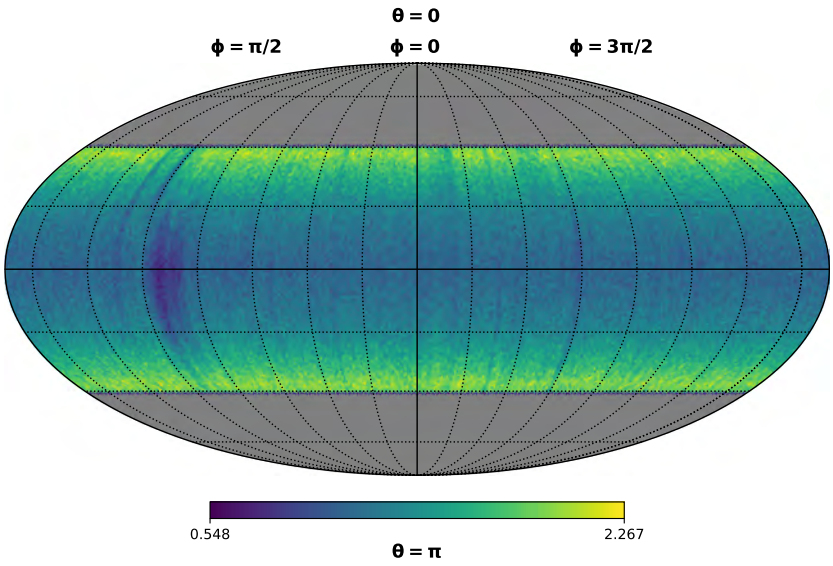

Figure 4.13: Map of overlapped events from the 10-15% centrality. Normalized by the ratio of N_{pix} to total event multiplicity.

over them. The resulting map of efficiencies is dubbed $D(\mathbf{n_p})$; note the use of $\mathbf{n_p}$ to indicate pixelation.

Due to its similarity to real data, MC_2 was chosen as the distribution to be analyzed under those detector-caused anisotropies. Explicitly, $f_{MC_2}(\hat{\mathbf{n}}) \to D(\hat{\mathbf{n}}) f_{MC_2}(\hat{\mathbf{n}})$, with the efficiency function $D(\hat{\mathbf{n}})$ considered to equally affect events pertaining to the same Run. Since we only have access to the pixelated map $D(\mathbf{n_p})$, the associated function $D(\hat{\mathbf{n}})$ must be estimated from it: given a resolution $N_{side} = 128$ map, a spline is made in θ for each fixed ϕ value. Event particles within the phase space $\phi \in [0, 2\pi)$, $\eta \in (-0.9, 0.9)$ are then sampled from the product $f_{D_2}(\hat{\mathbf{n}}) = D(\hat{\mathbf{n}}) f_{MC_2}(\hat{\mathbf{n}})$, where $D(\hat{\mathbf{n}})$ is the aforementioned collection of splines.

Likewise the previous MC cases, each event sampled from $f_{D_2}(\hat{\mathbf{n}})$ is projected onto a map with $N_{side} = 16$ and has its power spectrum calculated. The ensemble average is then taken and subtracted from the

isotropic $\langle N_\ell^{m\neq0}\rangle$, thus yielding $\langle S_\ell^{m\neq0}\rangle_{D_2}$ for particle distributions under varying detector efficiency.

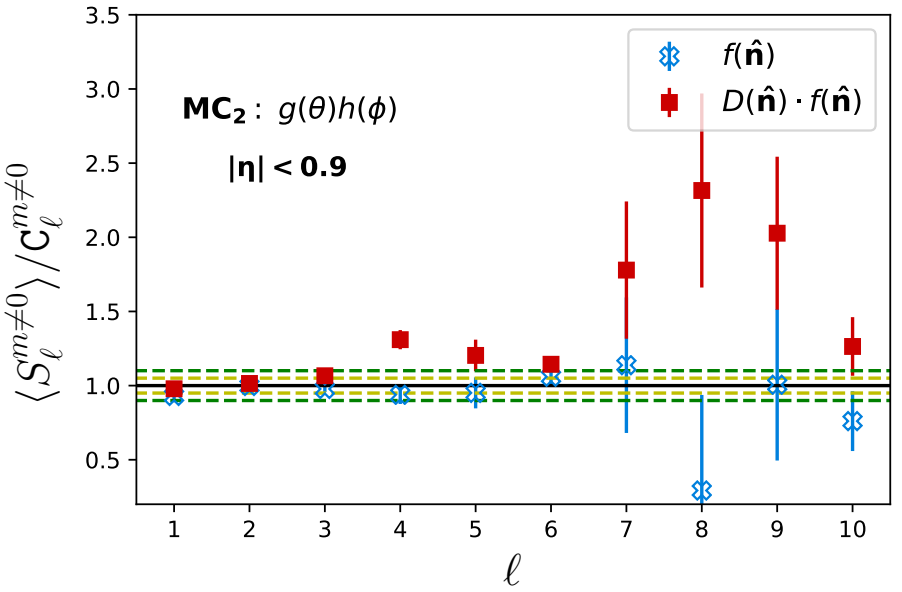

Figure 4.14: Ratios $\langle S_\ell^{m\neq0}\rangle / C_\ell^{m\neq0}$ for $f_{MC_2}(\hat{\mathbf{n}})$ and $f_{D_2}(\hat{\mathbf{n}})$. Dashed lines are 1σ (yellow) and 2σ (green) deviations for $f_{MC_2}(\hat{\mathbf{n}})$ within $1 \leq \ell \leq 6$.

As means of quantifying the effects of $D(\hat{\mathbf{n}})$ on the estimated power spectrum $\langle S_\ell^{m\neq0}\rangle_{D_2}$, the latter is divided by the true $C_\ell^{m\neq0}$. Furthermore, its performance is compared to that of MC_2 under perfect detector efficiency. The results are shown in Fig. 4.14 for $1 \leq \ell \leq 6$, which correspond to the modes associated with the input v_n coefficients. The dashed bands are 1σ and 2σ deviations of $\langle S_\ell^{m\neq0}\rangle_{MC_2}/C_\ell^{m\neq0}$ from unity. Note how the same ratio for the spectrum with detector-caused anisotropies stands above 2σ for $\ell \geq 4$, specially at $\ell = 8$. The angular scale at such mode is around 22.5^o, which turns out to be the approximate width of the dark patch in Fig. 4.13.

The contribution of detector efficiency is additive to the power spectrum. As a consequence, there is a fight for dominance between the latter and v_n-caused anisotropies. These mostly affect modes for $\ell \leq 6$ and their contribution wanes at higher ℓ values. From Fig. 4.14, v_n seems to have the upper hand for $\ell \leq 3$, while their influence and the detector's look comparable within $4 \leq \ell \leq 6$, with the latter's $\ell = 4$ being $\sim 30\%$ above unity. Finally, $D(\hat{\mathbf{n}})$ surpasses v_n for $\ell \geq 7$, where the angular scales correspond to the sizes of fluctuations in the efficiency function.

The proposed solution [87] begins with the overlap of all simulated event maps, $F^{all}(\mathbf{n_p})$, at $N_{side} = 16$ to create a projection akin to Fig. 4.13. As $D(\mathbf{n_p})$ is constant for all events and their θ distribution does not change orientation,

$$F^{all}(\mathbf{n_p}) = \sum_{i=0}^{N_{evts}} f_{D_2}^{(i)}(\mathbf{n_p}) = D(\mathbf{n_p}) g(\mathbf{n_p}), \tag{4.6}$$

where $g(\mathbf{n_p})$ stands for a map of $g(\theta)$ (Fig. 4.6) with ϕ uniform.

The second step consists in dividing each event map by $F^{all}(\mathbf{n_p})$, thus assigning weights to the pixels according to their positions. Explicitly,

$$\overline{f}_{D_2}(\mathbf{n_p}) = \frac{f_{D_2}(\mathbf{n_p})}{D(\mathbf{n_p}) g(\mathbf{n_p})}. \tag{4.7}$$

Note that these resulting maps are normalized by their total average θ distribution. Consequently, their associated background spectrum $\langle N_\ell^{m\neq 0} \rangle_{bar}$ must account for said division, as pixel weights change but not their densities, which in turn increase towards the edges. Therefore, to estimate $\langle N_\ell^{m\neq 0} \rangle_{bar}$, one must first randomize ϕ for each (θ, ϕ) event set. These are then mapped onto a spherical projection and subsequently divided by $g(\mathbf{n_p})$. Finally their spectra for $m \neq 0$ is calculated, with $\langle N_\ell^{m\neq 0} \rangle_{bar}$ being the ensemble average over 10^6 events. Each of the mentioned event maps have pixel weights distributed according to $g(\mathbf{n_p})$, though their densities remain the same, akin to $\overline{f}_{D_2}(\mathbf{n_p})$.

The maps $\overline{f}^{(i)}_{D_2}(\mathbf{n_p})$ are normalized by the factor N_{pix}/M_{pix}, where M_{pix} is the total pixel sum. Then, in the same way as before, we take the power spectrum of each $\overline{f}^{(i)}_{D_2}(\mathbf{n_p})$ and average over them, finally subtracting $\langle N_\ell^{m\neq 0}\rangle_{bar}$ from the result to yield $\langle S_\ell^{m\neq 0}\rangle_{bar}$. From Eq. (4.7), $\overline{f}_{D_2}(\mathbf{n_p}) = h(\mathbf{n_p})$, with $h(\mathbf{n_p})$ a map of $h(\phi)$ also smooth in θ. Furthermore $\langle N_\ell^{m\neq 0}\rangle_{bar}$ already accounts for the characteristic pixel densities. As a result, $\langle S_\ell^{m\neq 0}\rangle_{bar}$ must be an estimate of the spectrum for $f_{MC_1}(\hat{\mathbf{n}}) = h(\phi)$.

Unsurprisingly, the estimated $\langle S_\ell^{m\neq 0}\rangle_{bar}$ for $\overline{f}_{D_2}(\mathbf{n_p})$ seems to fit the calculated $f_{MC_1}(\hat{\mathbf{n}})$ spectrum quite well, as seen in Fig. 4.15 (a). For $\ell = 8$, the spectrum value was subdued relative to $\langle S_8^{m\neq 0}\rangle_{D_2}$, thus suggesting that the aforementioned procedure may have worked. In Fig. 4.15 (b), there is a comparison between the performances of the $f_{MC_1}(\hat{\mathbf{n}})$ and $\overline{f}_{D_2}(\mathbf{n_p})$ spectra relative to the true one, calculated through $\langle S_\ell^{m\neq 0}\rangle / \mathrm{C}_\ell^{m\neq 0}$ for each of them. The dashed yellow and green lines correspond, respectively, to 1σ and 2σ deviations of the mentioned ratio to unity.

Until $\ell = 6$, $\langle S_\ell^{m\neq 0}\rangle_{bar}$ behaves quite similarly to $f_{MC_1}(\hat{\mathbf{n}})$, with its values sitting approximately within the 1σ deviation of MC_1. As previously remarked, that is the region of v_n dominance. For higher ℓ, the values mainly affected by detector anisotropies have lowered, despite the large error bars. In any case, those are compatible with the ones for $f_{MC_1}(\hat{\mathbf{n}})$, which at least indicates that the proposed method worked for the present distributions at a minimum scale of $\ell = 10$.

Summing up, the estimated spectrum under varying detector efficiency is characterized by values that stand above its perfect counterpart (Fig. 4.14). Specially for $\ell = 8$, the mode associated with the angular size of the biggest patch in Fig. 4.13. The solution to this issue consists in basically normalizing the $f_{D_2}(\mathbf{n_p})$ maps by their sum. As a consequence, pixel weights were assigned according not only to the desired $D(\mathbf{n_p})$, but also to $g(\mathbf{n_p})$, leading to the background estimation $\langle N_\ell^{m\neq 0}\rangle_{bar}$. The final resulting spectrum $\langle S_\ell^{m\neq 0}\rangle_{bar}$ matched that of MC_1 and performed successfully in the flow dominated region, aside from yielding lower values

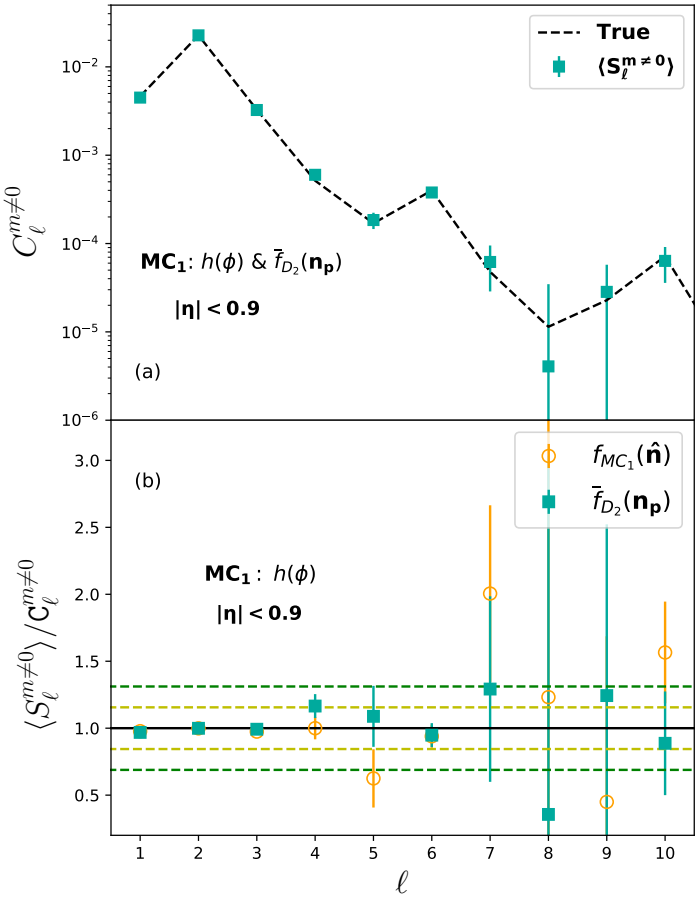

Figure 4.15: Comparison between $\langle S_\ell^{m\neq0}\rangle_{bar}$ and the expected MC_1 spectrum (a). Ratios $\langle S_\ell^{m\neq0}\rangle / C_\ell^{m\neq0}$ for $f_{MC_1}(\hat{\mathbf{n}})$ and $\overline{f}_{D_2}(\mathbf{n_p})$ (b). Dashed lines are 1σ (yellow) and 2σ (green) deviations of the MC_1 ratio from unity within $1 \leq \ell \leq 6$.

where $D(\mathbf{n_p})$ anisotropies are the main contributors, $\ell = 7, 8, 9$.

In conclusion, the method introduced in this subsection to tackle detector efficiency seems to have worked within the limits of the scales associated with the MC distributions at hand, i.e., $\ell \leq 10$. Thus, it shall

be used to estimate the angular power spectrum of heavy ions, a result shown and discussed in the next chapter.

4.3.4 Choosing resolution

Both methods presented above for tackling the low multiplicity and detector efficiency effects on the estimated power spectrum have relied on a resolution of $N_{side} = 16$. However, no clear reason for such choice has been given. Because of that, this last subsection deals with the resulting $\langle S_\ell^{m\neq 0} \rangle$ for the resolutions pertaining to $N_{side} = 8, 16, 32$.

As mentioned in Sec. 4.2, each value of N_{side} permits different ℓ_{max}, with one directly proportional to the other. Due to their low multiplicities, heavy ion collisions at 2.76 TeV cannot be probed at very high ℓ, like in the CMB. Additionally, they are mainly dominated by large scale geometries, such as the fluctuations caused by flow. Then, if modes up to $\ell = 20$ should be considered, $N_{side} = 8, 16, 32$ are all reasonable choices. Their main characteristics, N_{pix} within $|\eta| < 0.9$, mean pixel spacing and area are shown in Table 4.2.

N_{side}	N_{pix} ($\|\eta\| < 0.9$)	Mean Spacing (deg)	Area (sterad)
8	**600**	**7.3290**	$\mathbf{1.6362 \times 10^{-2}}$
16	**2344**	**3.6645**	$\mathbf{4.0906 \times 10^{-3}}$
32	**9040**	**1.8323**	$\mathbf{1.0227 \times 10^{-3}}$

Table 4.2: HEALPix pixel information for $N_{side} = 8, 16, 32$. Adapted from [89].

For the selected centralities in this work, typical event multiplicity varies from ~ 450 to ~ 3100 within the present phase space $|\eta| < 0.9$, $\phi \in [0, 2\pi)$. In principle, $N_{side} = 8$ could cover the whole range, with minimum amount of empty pixels. However, there is the risk of excessively smoothing the signal for more central collisions. The alternative

is $N_{side} = 16$, where events with multiplicities of $\mathcal{O}(10^3)$ should cover $\sim 50\%$ of the pixels, while those with lower M will become more granular. Finally, $N_{side} = 32$ provides better estimations for the harmonic coefficients $a_{\ell m}$ through Eq. (4.1), since $Y_{\ell m}(\mathbf{n_p})$ are evaluated at pixel center and those have smaller mean spacing; see Table 4.2.

It is necessary to quantify the impact of resolution in this context where multiplicities and flow harmonics change with centrality. As previously discussed, estimating $\langle S_\ell^{m\neq 0}\rangle$ depends not only on the number of samples per event, but also on the underlying function. Taking the range of 0-40% most central collisions, it is well understood that v_n increases as they become more peripheral, see for instance [45, 90]. In light of these facts, the next MC distributions are drawn from $f_{MC_2}(\hat{\mathbf{n}})$ for three centralities: 0-5%, 10-15% and 35-40%.

The multiplicity intervals at hand were inspired by the ALICE open data set [9] itself. Their centrality division was done by first taking the 0-5% events with highest multiplicity, then proceeding in intervals of 5% until 35-40%. Above this value, the number of particles per event could be quite low for the power spectrum analysis, hence the chosen threshold. The multiplicity intervals of interest are as follows: $M \in (2200, 3100)$, $M \in (1400, 1800)$ and $M \in (470, 600)$, for 0-5%, 10-15% and 35-40%, respectively. Furthermore, each population of simulated events has the same $g(\theta)$ distribution, though the v_n values from $h(\phi)$ differ. From v_2 to v_4, they were estimated through splines made from the results in [45]. As for v_5 and v_6, their values were directly taken from [90]. Lastly, v_1 was simply chosen to stand between v_3 and v_4.

Akin to the preceding cases, $\langle N_\ell^{m\neq 0}\rangle$ was calculated according to the events' multiplicity distribution and subtracted from the observed spectrum to estimate $\langle S_\ell^{m\neq 0}\rangle$. This process was repeated for all three centralities and N_{side} values presented above and the result can be seen in Fig. 4.16, along with the ratio to expected $\mathtt{C}_\ell^{m\neq 0}$. The dashed lines on the right plots represent 1σ (yellow) and 2σ deviations of the $N_{side} = 16$ ratio result to unity within the flow-dominated interval $1 \leq \ell \leq 6$. No matter

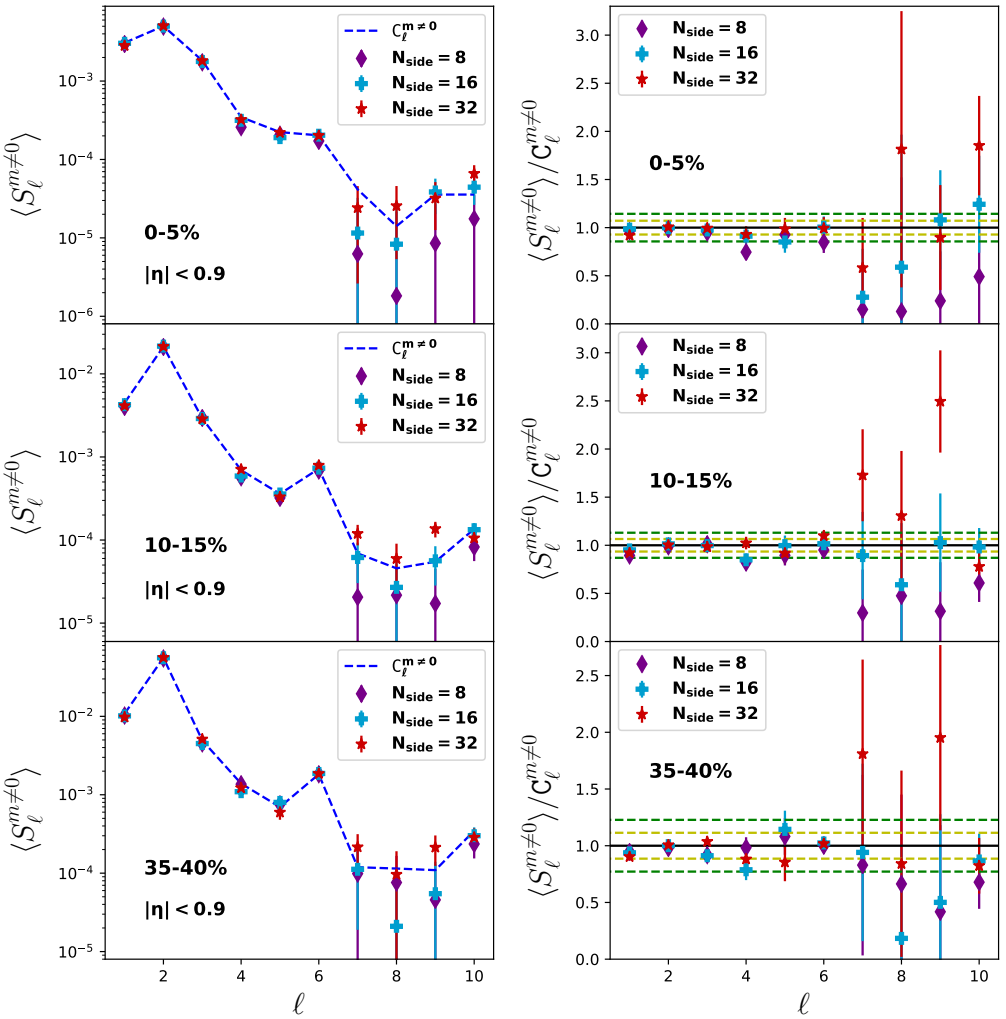

Figure 4.16: Left: estimates of $\langle S_\ell^{m\neq0}\rangle$ for three centralities, with different v_n values. Right: their ratios to the expected $f_{MC_2}(\hat{\mathbf{n}})$ spectra are compared to 1σ and 2σ deviations (dashed lines) of $N_{side} = 16$ within $1 \leq \ell \leq 6$.

the resolution or centrality, it is at specifically these values that $\langle S_\ell^{m\neq 0}\rangle$ is the closest to the true spectrum. For $\ell \geq 7$, where v_n contribution dwindles, uncertainties are large for all N_{side}, with 32 usually overestimating $\langle S_\ell^{m\neq 0}\rangle$ and 8 doing the opposite.

At least in the angular scales of interest ($1 \leq \ell \leq 6$), $N_{side} = 8$ was overall a slightly better choice for 35-40%, while $N_{side} = 32$ was for 0-5%. As for the whole multipole region at hand ($\ell \leq 10$), $N_{side} = 16$ had the best performance for 0-5% and 10-15%. At higher M and v_n, probing small angular scales would become easier and easier. Instead, heavy ion data behaves in a way that there is an inverse relation between multiplicity/centrality and flow. Note how $\ell = 10$ for 0-5% differs from the other centralities, despite being a mode with contributions from all even v_n. Central collisions are, after all, the closest to isotropy.

Given this multiplicity-flow interplay, the calculation of $\langle S_\ell^{m\neq 0}\rangle$ faces challenges at all centralities. Additionally, it is of interest in this work to choose a single resolution for all event maps. Thus, settling at $N_{side} = 16$ is a reasonable middle-ground approach. It actually performs quite similarly to $N_{side} = 32$ for more central collisions and, though $N_{side} = 8$ could be a better option for 35-40%, $N_{side} = 16$ is not far off the mark. Also, there was no significant difference between resolutions for $\ell \leq 6$, a sign that the binning of $f_{MC_2}(\mathbf{n_p})$ maps and $Y_{\ell m}(\mathbf{n_p})$ somehow compensate for each other. The former may have more empty pixels with higher N_{side}, but the latter's value should be more accurate. On the other hand, $f_{MC_2}(\mathbf{n_p})$ may fill up most of the pixels, though $Y_{\ell m}(\mathbf{n_p})$ becomes less accurate.

At last we are equipped with a method for estimating the angular power spectrum of heavy ions. The chosen resolution of $N_{side} = 16$ permeates through this work and $\langle S_\ell^{m\neq 0}\rangle$ will be analyzed up to $\ell = 20$, associated with scales of $\sim 9^o$. After all, it has been stated that limits of the computed spectrum are not only connected to the multiplicity, but also the function at hand. Summing up, after setting on N_{side}, event maps are created, their spectra calculated for $m \neq 0$ modes and finally

the average is taken. Then, background spectrum estimation $\langle N_\ell^{m\neq 0}\rangle$ comes into play: how do fully isotropic distributions with same multiplicity fare under the same map manipulations? Finally, the primary spectrum $\langle C_\ell^{m\neq 0}\rangle$ is subtracted from background to estimate the signal spectrum $\langle S_\ell^{m\neq 0}\rangle$. All calculations are based on the average ensemble behavior, with no mechanisms currently existing to make low-M corrections event-by-event.

On the next chapter, the method presented above will be applied to ALICE open data [9]. The whole analysis on MC simulations has anisotropies coming solely from flow, with factorizable functions. Consequently, we have an idea of how an angular power spectrum should be in this scenario. Elliptic flow would cause a high peak in $\ell = 2$ and a smaller one in $\ell = 6$, the presence of v_3 would also make $\ell = 3$ rise above modes with higher ℓ. Moreover, beyond a certain ℓ value, the spectrum would be characterized by large uncertainties, as flow contribution wanes and angular scales count with more empty spaces than particles.

5 Angular Power Spectrum of Heavy Ions

"New ideas pass through three periods: 1) It can't be done. 2) It probably can be done, but it's not worth doing. 3) I knew it was a good idea all along!"

— Arthur C. Clarke

Equipped with a method which works for Monte Carlo simulations until a characteristic scale, it is time to apply power spectrum estimation to data. We know from Ch. 2 that there are a plethora of phenomena resulting in two-particle correlations. Accordingly, the calculated spectrum should have both the influence of anisotropic flow and other sources, with each probably dominating different scales. This chapter begins with vertex selection, since it interferes in the final geometry, then we move to compute the very first power spectra of heavy ion collisions, each for a centrality class. Following up, we translate the spectrum into flow coefficients, comparing to Q-cumulants results with and without a pseudorapidity gap. Finally, we check what happens when the transverse momentum phase space is split into $p_T < 0.54$ GeV and $p_T > 0.54$ GeV, thus uncovering their typical geometries.

5.1 Vertex selection

One of the main tasks of the ITS subdetector consists in reconstructing the collision's interaction point, also called primary vertex, whose position is defined here as z_{vtx}. As mentioned in Ch. 4, the algorithm used for data selection [10] fires solely for charged particles and when $z_{vtx} \in (-10, 10)$ cm relative to the detector's center along the beam direction z.

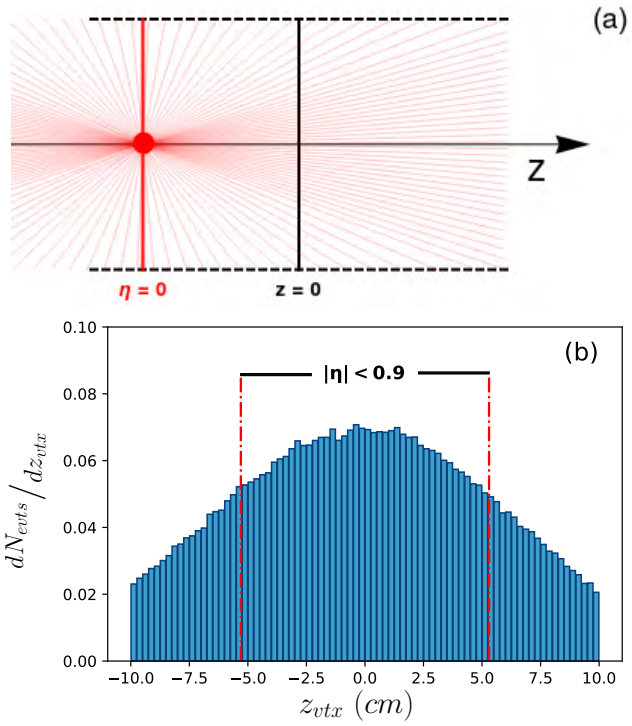

Figure 5.1: Scheme of a heavy ion collision with $z_{vtx} = -7.5$ cm (a). Distribution of N_{evts} according to their z_{vtx} (b).

In Fig. 5.1 (a), a cross section of the ITS inner barrel is roughly depicted, as particles are emitted from the collision's primary vertex ($\eta = 0$) located at $z_{vtx} = -7.5$ cm. The solid line at $z = 0$ indicates the mid-point

along the beam axis, in the ITS center, while the dashed ones represent the detector's pseudorapidity coverage within $|\eta| < 0.9$. However, for events occurring on the edges, the full length of said phase space is compromised. More specifically, for an uniform acceptance in $|\eta| < 0.9$, primary vertices must lie within a length of ± 5.3 to $z = 0$ [79]. Luckily, the majority of events correspond to the aforementioned condition, as seen in Fig. 5.1 (b); dashed red lines mark the limit where $|\eta| < 0.9$ can be fully covered.

Let $f_z^{(i)}(\mathbf{n_p})$ be the map of an event (i) whose interaction point z_{vtx} lies within a certain interval $(z - dz/2, z + dz/2)$, for a chosen dz length and z position. Then define $F_z^{all}(\mathbf{n_p})$ as the sum over these maps, similarly to Eq. (4.6). Said results are shown in Fig. 5.2 for $dz = 2$ cm and events with primary vertices belonging to $(8, 10)$ cm, the right-most interval, and $(-2, 0]$ cm, which is close to the center. Note the asymmetry of $F_9^{all}(\mathbf{n_p})$ (top), as particles whose polar coordinates approach the mask edge, $\theta \to 44^o$, are unaccounted for. In contrast, $F_{-1}^{all}(\mathbf{n_p})$ (bottom) has the expected characteristics of overlapping heavy ion distributions, with higher densities towards the edges and smooth azimuth, save for detector efficiency.

Given that the detector acceptance of events whose primary vertices lie beyond ± 5.3 cm does not correspond to $|\eta| < 0.9$, the mixing matrix $W_{mm'}^{\ell\ell'}$ should take a different outlook than shown in Fig. 4.3. As a consequence, $a_{\ell m}$ coefficients for maps with $|z_{vtx}| > 5.3$ cm will have distinct distributions compared to the rest. For instance, recall that fully isotropic maps limited to $|\eta| < 0.9$ had only non-zero $a_{\ell 0}$ modes with ℓ even. In the advent of an asymmetric mask, however, the mixing matrix would change its properties, thus allowing coefficients with ℓ odd to survive. This would completely change the average isotropic spectrum in Fig. 4.5.

The $F_{-1}^{all}(\mathbf{n_p})$ map on the bottom of Fig. 5.2 possesses a large scale geometry characterized by its symmetry around the equator. Based on this fact and the opposing feature of the top map, it should be interesting to check the a_{10} values of their underlying events, since harmonics with

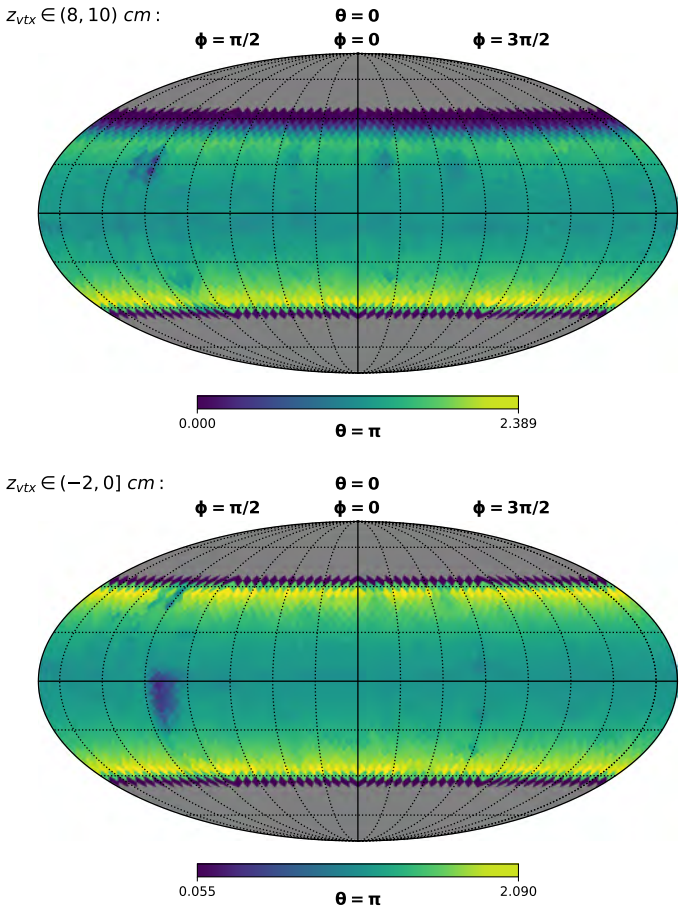

Figure 5.2: Superposed event maps $F_z^{all}(\mathbf{n_p})$ for $z_{vtx} \in (8, 10)$ cm (top) and $z_{vtx} \in (-2, 0]$ cm. Maps belong to the 10-20% centrality.

ℓ odd and $m = 0$ are themselves asymmetric relative to $\theta = \pi/2$.

Density distributions of $|a_{10}|^2$ are depicted in Fig. 5.3 for events belonging to the 10-20% centrality and with primary vertices positions at $z_{vtx} \in (8, 10)$ cm (top of Fig. 5.2), $z_{vtx} \in (-2, 0]$ cm (bottom of Fig. 5.2) and $z_{vtx} \in (4, 6]$ cm, a chosen intermediary interval. At first glance, it is already quite clear that the events with $z_{vtx} \in (8, 10)$ cm have a large

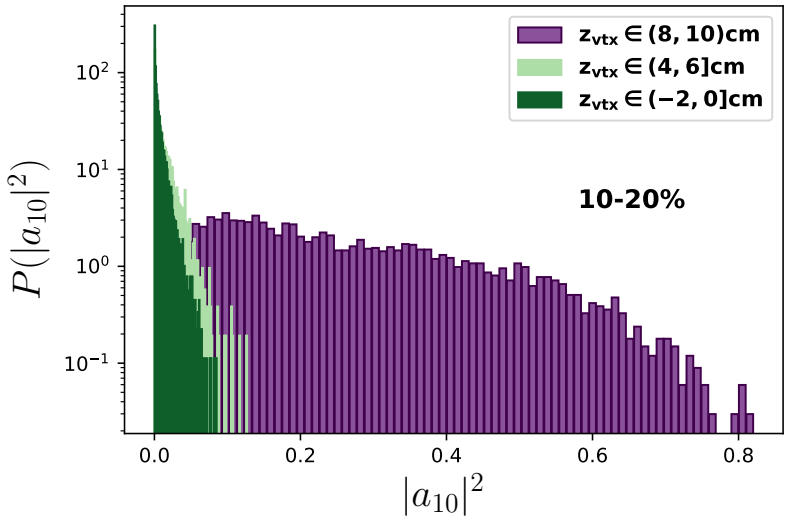

Figure 5.3: Density distribution of harmonic coefficient $|a_{10}|^2$ for events with primary vertices located in three distinct intervals.

scale anisotropy caused by asymmetric hemispheres. The spread out $|a_{10}|^2$ values up to 0.8 contrast with their counterparts closer to the detector's center. For $z_{vtx} \in (-2, 0]$ cm, the distribution has a mean value of $\mathcal{O}(10^{-3})$, which corresponds to the typical scale of fluctuations pertaining to multiplicity values from the 10-20% centrality, as noted in Ch. 4. Lastly, $z_{vtx} \in (4, 6]$ cm is $\sim 65\%$ composed of events with $|\eta| < 0.9$, which can explain the slight deviation is has from the previous case.

It should also be remarked that detector efficiency maps $D(\mathbf{n_p})$ must instead be denoted as $D_z(\mathbf{n_p})$, since the position in θ of its dark patches change with the events' interaction point. This effect can be seen in Fig. 5.2: for example, notice how the spot right below the equator on the bottom map is touching the lower edge ($\theta \sim 136^o$) of the top one. With efficiency depending on primary vertex position, the power spectrum estimation of heavy ion data, specially the normalization by $F_z^{all}(\mathbf{n_p})$, must be done for each separate interval in z. Following up, we do cen-

trality division and apply the method from Ch. 4 to data events with $z_{vtx} \in (-4, 4]$ cm, partitioned in widths of $dz = 2$ cm.

5.2 Power spectrum estimation applied

The ALICE data from [9] and extracted with [10] comprises of charged particles with $44^o \lesssim \theta \lesssim 136^o$, $0 \leq \phi < 2\pi$ and $0.15 < p_T < 100$ GeV. The focus of this work is to map particle angular coordinates $\hat{\mathbf{n}} = (\theta, \phi)$ onto the surface of a sphere, calculate their power spectra and take the ensemble average. Due to the limited detector coverage, however, the true underlying spectrum gives place to a *pseudo*-C_ℓ, associated to the former through a mixing matrix. It is of utmost interest that $W^{\ell\ell'}_{mm'}$ remains the same for all events, so only primary vertices within ±5.3 cm should be considered. Furthermore, detector efficiency $D_z(\mathbf{n_p})$ changes with the position of z_{vtx}, hence the necessity of estimating $\langle S_\ell^{m\neq 0} \rangle$ for each chosen interval in the beam axis.

The choice of $dz = 2$ cm as the interval width should enable each $D_z(\mathbf{n_p})$ to be approximately unique for a given z, while maintaining a reasonable number of events per bin. Since uniform acceptance within $|\eta| < 0.9$ is desired, only the intervals $(-4, 2]$ cm, $(-2, 0]$ cm, $(0, 2]$ cm and $(2, 4]$ cm will be considered in the following analysis.

Once a vertex interval has been selected, it is necessary to separate its events into centrality bins using their multiplicities. Recall that impact parameter and number of participant nucleons are directly related, Additionally their values influence the final particle multiplicity. This centrality division is shown in Fig. 5.4, where N_{evts} is plotted as a function of M for $z_{vtx} \in (-2, 0]$ cm. The intervals are limited by dashed red lines and numbered according to their centrality: (1) pertains to the 0-5% events with highest multiplicity, (2) to the 5-10% with highest M, (3) to 10-20%, (4) to 20-30% and (5) to 30-40%. The last three have $N_{evts} \sim 8000$, while the first two have $N_{evts} \sim 4000$.

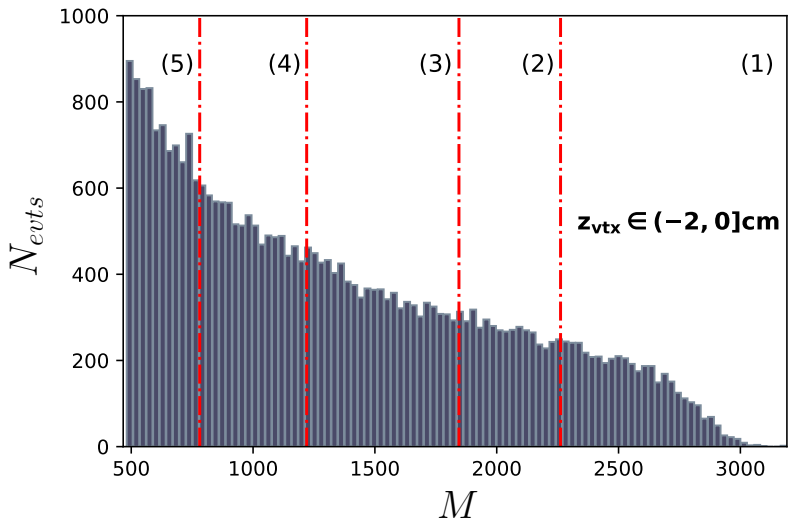

Figure 5.4: Centrality dependence on multiplicity: (1) **0-5%**, (2) **5-10%**, (3) **10-20%**, (4) **20-30%**, (5) **30-40%**.

After fixing z_{vtx}, we focus on a single centrality class in order to proceed with the power spectrum estimation. Then, the usual first steps are taken: **(i)** particles are mapped onto spherical projections with resolution $N_{side} = 16$, **(ii)** the resulting $f_z(\mathbf{n_p})$ are summed over, yielding $F_z^{all}(\mathbf{n_p}) = D_z(\mathbf{n_p})g(\mathbf{n_p})$. Following up is **(iii)** the normalization of event maps by their sum, $\overline{f}_z(\mathbf{n_p}) = f_z(\mathbf{n_p})/F_z^{all}(\mathbf{n_p})$, which assigns weights to pixels according to the vertex detector efficiency $D_z(\mathbf{n_p})$ and the overall θ distribution, $g(\mathbf{n_p})$. The latter should be independent of the choice in z_{vtx} interval. Moreover, **(iv)** the spectrum of each $\overline{f}_z(\mathbf{n_p})$ is calculated for modes with $m \neq 0$ to diminish geometrical effects caused by the $W(\mathbf{n_p})$ mask and, lastly, **(v)** the ensemble average is computed, thus issuing $\langle C_\ell^{m\neq 0} \rangle$.

The single map normalization by $F_z^{all}(\mathbf{n_p})$ is depicted in Fig. 5.5 for an event with $z_{vtx} \in (-2, 0]$ cm and it belonging to the 10-20% centrality. Note the grid square which corresponds to the dark patch in the bottom

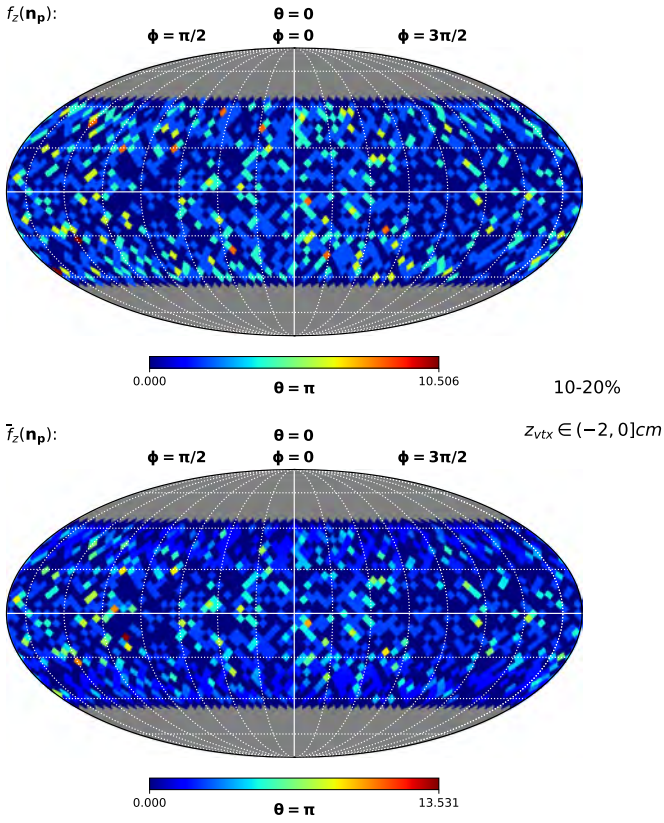

Figure 5.5: Single event map $f_z(\mathbf{n_p})$ (top) and its normalized version $\overline{f}_z(\mathbf{n_p}) = f_z(\mathbf{n_p})/F_z^{all}(\mathbf{n_p})$ (bottom); its interaction point lies within $(-2, 0]$ cm.

map of Fig. 5.2: when comparing it between the maps in Fig. 5.5, one may realize that $\overline{f}_z(\mathbf{n_p})$ has a deep red spot in this region. It is a consequence of assigning weights to the pixels according to $D_z(\mathbf{n_p})$. What is more, the brightness of pixels in $\overline{f}_z(\mathbf{n_p})$ is more concentrated along the equator, while for $f_z(\mathbf{n_p})$, it is spread out. Despite that, pixel density has not changed, as what is zero remains so. This characteristic must be accounted for when calculating $\langle N_\ell^{m\neq 0} \rangle$ for normalized maps whose

originals were anisotropic in θ.

Once stages **(i-v)** have been completed, it is time to estimate the background spectrum $\langle N_\ell^{m\neq 0}\rangle$ connected with the current interaction point interval and centrality. Likewise the case of MC_2 (Ch. 4) with non-unitary detector efficiency, the lack of uniformity in pixel density must be taken into consideration, since maps are divided by $g(\mathbf{n_p})$. This procedure goes as follows: **(vi)** original event maps $f_z(\mathbf{n_p})$ have their ϕ coordinates randomized according to a uniform distribution in $[0, 2\pi)$. Consequently, detector anisotropies are smoothed out, leaving only the θ distribution. Subsequently, **(vii)** these resulting events are summed over to extract $g(\mathbf{n_p})$. Next, the process in **(vi)** is repeated with a slight alteration: instead of going through each event once, **(viii)** they are randomly drawn by the algorithm and again have their ϕ values changed, though now their maps are divided by $g(\mathbf{n_p})$ to simulate the pixel weight distribution and density of $\overline{f}_z(\mathbf{n_p})$. This last step is repeated 10^6 times. Then **(ix)** their spectra are calculated for $m \neq 0$ and averaged over, yielding $\langle N_\ell^{m\neq 0}\rangle$.

Summing up, **(vi, vii)** produce $g(\mathbf{n_p})$, while **(viii, ix)** compute $\langle N_\ell^{m\neq 0}\rangle$. Results for the latter and $\langle C_\ell^{m\neq 0}\rangle$ can be seen in Fig. 5.6 for the vertex interval $z_{vtx} \in (-2, 0]$ cm and 10-20% centrality. Notice how the spectrum calculated from data stands slightly above its estimated background, which differs from the behavior of the MC simulations previously studied. In Fig. 4.10, the resulting MC average spectra seemed to coincide with the isotropic one for $\ell \geq 7$, suggesting that deviations from isotropy at such scales are of very low order in comparison to $\ell \leq 6$, the region dominated by v_n. Nonetheless, $\langle C_\ell^{m\neq 0}\rangle$ from Fig. 5.6 has some similarities to the distributions from Ch. 4: the peak at $\ell = 2$, associated with v_2 itself, and prominent values at the other $\ell \leq 6$ modes, with a more accentuated bump at $\ell = 6$ than the MC cases.

At last, the background is subtracted from the data spectrum, resulting in $\langle S_\ell^{m\neq 0}\rangle = \langle C_\ell^{m\neq 0}\rangle - \langle N_\ell^{m\neq 0}\rangle$ for a given vertex interval and centrality class. The latter respectively correspond to $z_{vtx} \in (-2, 0]$ cm and 10-20%

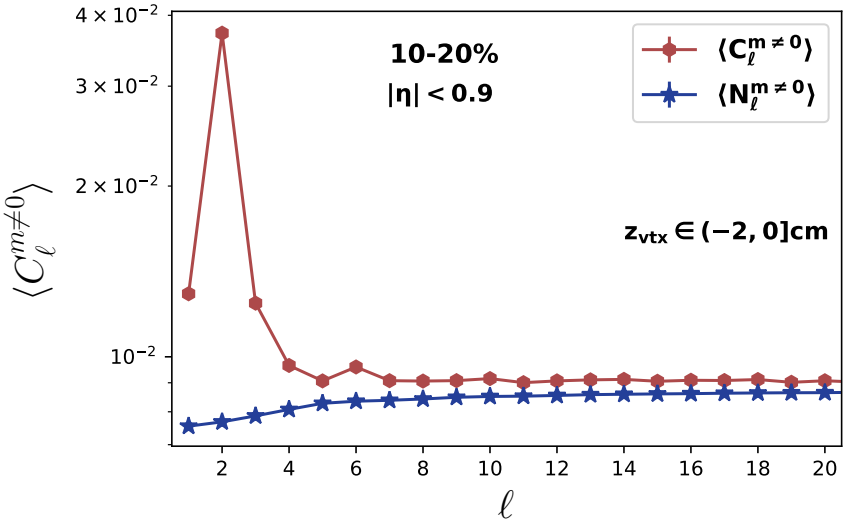

Figure 5.6: Comparison between $\langle C_\ell^{m\neq 0}\rangle$ calculated from 10-20% data and the estimated background $\langle N_\ell^{m\neq 0}\rangle$ for $z_{vtx} \in (-2, 0]$ cm.

in Fig. 5.7 (a). Unsurprisingly, modes at $\ell \leq 6$ have remarkably similar features to the MC power spectra in the same region. In contrast, MC values for $\ell \geq 7$ drop to $\mathcal{O}(10^{-5})$, while for data they are one order of magnitude larger (refer back to Fig. 4.12).

Steps **(i-ix)** are repeated for all aforementioned vertex intervals with width of $dz = 2$ cm. Due to each final spectrum originating from batches with distinct N_{evts}, their *weighted average* is thus taken, here denoted as $\langle S_\ell^{m\neq 0}\rangle_z$; note the subscript z to indicate the mean spectrum of z_{vtx} intervals. This result is depicted in Fig. 5.7 (b), with the points indicating each $\langle S_\ell^{m\neq 0}\rangle$ from a fixed z_{vtx} and the lines representing their average $\langle S_\ell^{m\neq 0}\rangle_z$ weighted by the number of events. The standard deviation of the vertices spectra values at each ℓ are of order $\mathcal{O}(10^{-5})$. Error bars for the total mean spectrum $\langle S_\ell^{m\neq 0}\rangle_z$ are obtained through error propagation of the individual z_{vtx} spectra; they are also of $\mathcal{O}(10^{-5})$, hence their invisibility.

As a bonus, the whole procedure up until this point was repeated for

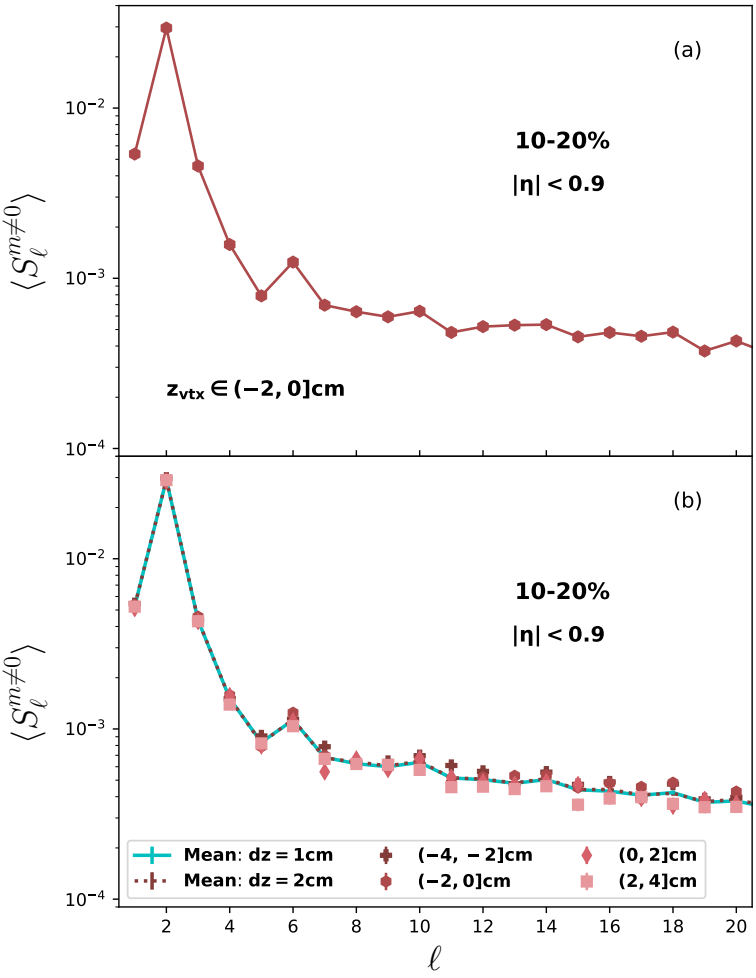

Figure 5.7: (a) Estimated $\langle S_\ell^{m\neq 0}\rangle$ for $z_{vtx} \in (-2, 0]$ cm and 10-20% centrality. (b) Estimated $\langle S_\ell^{m\neq 0}\rangle$ for all vertices within $(-4, 4]$ cm and $dz = 2$ cm (points) in addition to the averages when $dz = 2$ cm and $dz = 1$ cm with $z_{vtx} \in (-5, 5]$ cm (lines).

events with interaction points within $(-5, 5]$ cm separated in intervals of width $dz = 1$ cm. Observe in Fig. 5.7(b) how their mean spectrum

(blue line) coincides with the $dz = 2$ cm case (dotted line). This result strengthens the applicability of the method developed in this work.

The vertex averaged $\langle S_\ell^{\neq 0} \rangle_z$ from Fig. 5.7 (b) is an estimate of the angular power spectrum of the 10-20% most central heavy ion events. The stages of its calculation can be followed to compute the spectra pertaining to the other centralities shown in Fig. 5.4. The latter's division is performed for all four intervals within $(-4, 4]$ cm. Then steps **(i-ix)** are used to find $\langle S_\ell^{m\neq 0} \rangle$ for all centralities within each vertex interval. At last, these final spectra are averaged over z_{vtx}, thus providing the results in Fig. 5.8.

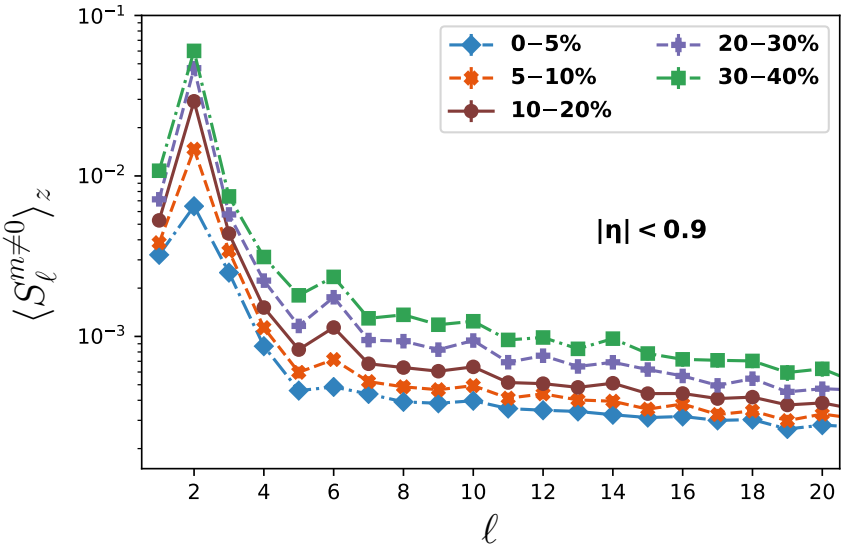

Figure 5.8: Power spectra averaged over vertices $\langle S_\ell^{m\neq 0} \rangle_z$ for centrality classes within 0-40%.

At first glance, the spectra in Fig. 5.8 possess the same usual features: a peak in $\ell = 2$ followed by descending values until a bump in $\ell = 6$. Then, a damping tail mainly characterizes the higher modes. Addition-

ally, a clear spectral hierarchy is observed from the most central events to more peripheral ones, as $\langle S_\ell^{m\neq 0}\rangle_z$ acquires higher values.

The almond-like shape of overlapping nuclei is largely associated with the elliptic flow coefficient v_2 of the Fourier expansion in Eq. (2.3). Given that events belonging to the lower centrality percentages have a more spherical form than their counterparts, it is no wonder that the $\ell = 2$ peak becomes more enhanced with peripheral collisions; refer to the relation in Eq. (4.3) between $a_{\ell m}$ and v_n under a possible pure-flow distribution. Also, $\ell = 2$ has the highest variation with centrality among the other modes, as its values spam over one order of magnitude.

All these large scale characteristics strongly indicate the presence of flow. They resemble the aspects of the MC spectra from Ch. 4 and the relations between ℓ modes share similarities with the plot in Fig. 2.8 of integrated v_n as a function of centrality. Specifically, $v_2 > v_3 > v_4$ and their values increase from 0-5% to 30-40% most central events, specially v_2.

The angular power spectrum describes correlations of (θ_i, ϕ_i) pairs in Fourier space; a sentence from Ch. 3. In other words, it measures the size of fluctuations for two-particle correlations, since it is the second moment $\langle a_{\ell m} a^*_{\ell' m'}\rangle$ of a distribution $f(\hat{\mathbf{n}})$. Jets, resonance decays and other phenomena contribute to the two-point function of emitted hadrons. Due to their small angular structure, the tail at $\ell \geq 7$ could be an indicative of their existence. After all, the latter would not appear if the spectrum was completely dominated by flow, as seen in Ch. 4.

The aforementioned features of $\langle S_\ell^{m\neq 0}\rangle_z$ raise the question of whether one could actually obtain the v_n coefficients from the latter and what is the impact of non-flow phenomena. Furthermore, the mode value at $\ell = 1$ suggests a net dipole asymmetry in the data worth investigating. These subjects are tackled in the next section, as we translate angular power spectrum into Fourier flow harmonics.

5.3 Flow contribution

Results from the previous section strongly indicate that geometries of different scales are encoded in the angular power spectra of Fig. 5.8 (b). Besides, Monte Carlo simulations from Ch. 4 showed that, in a pure flow scenario, modes would be the most enhanced for $\ell \leq 6$, while other sources of fluctuations could take over for higher multipole values. The well-studied v_n harmonics [35, 36] describe azimuthal anisotropies of the final hadron distribution, while C_ℓ, or $\langle S_\ell^{m\neq 0}\rangle$, quantifies angular pair correlations on a sphere. At first glance, these seem to treat the emitted particles from quite distinct perspectives, specially considering their dimensions. Then, this work's next objective consists in finding a relation between these quantities associated with azimuthal and spherical geometries.

5.3.1 Back to simulations

Take a step back and look again at the distributions from Ch. 4, $f_{MC_1}(\hat{\mathbf{n}})$ and $f_{MC_2}(\hat{\mathbf{n}})$. Both are *factorizable* functions which, under the $W(\hat{\mathbf{n}})$ mask, have associated harmonic coefficients $a_{\ell m}$ given by Eq. (4.3), save for their $b_{\ell m}$ values. These still end up being analogous to Eq. (4.4), though the integral in θ goes from $\sim 44^o$ to $\sim 136^o$. In other words, one should make the substitution $g(\theta) \to W(\hat{\mathbf{n}})g(\theta)$ to get the $b_{\ell m}$ of interest.

Having established the relation between flow and spherical harmonic coefficients for the functions at hand, $|a_{\ell n}|^2 = |b_{\ell n}|^2 v_n^2$, combine it with Eq. (4.5) and isolate v_n to find:

$$|v_n|^2 = \frac{2n+1}{2} \cdot \frac{C_n^{m\neq 0}}{|b_{nn}|^2} \cdot \frac{|b_{00}|^2}{C_0} \quad \text{or} \tag{5.1}$$

$$|v_n|^2 = \frac{1}{|b_{nn}|^2}\left[\frac{2n+1}{2} \cdot C_n^{m\neq 0} - \frac{2n-3}{2} \cdot \frac{|b_{nn-2}|^2}{|b_{n-2n-2}|^2} \cdot C_{n-2}^{m\neq 0}\right]\frac{|b_{00}|^2}{C_0}, \tag{5.2}$$

valid for $n = 1, 2$ and $n = 3, 4$, respectively. The normalization factor $|b_{00}|^2/C_0$ equals one if the integral of $f(\hat{\mathbf{n}})$ over the sphere is set to 4π, in accordance with the spectra calculated in this work. The expressions in Eqs. (5.1, 5.2) become larger and larger for higher n, as all $b_{\ell m}$ modes with $\ell, m \leq n$ may contribute as long as ℓ, m have the same parity.

At this point, it would be a great opportunity to compare this extraction of flow through $C_\ell^{m\neq 0}$ to other known methods. Due to its reliance on computations of particle correlations, the Q-cumulants [13, 42] method was chosen.

Sets of events were drawn from the following distributions: $f_{MC_1}(\hat{\mathbf{n}}) = h(\phi)$, $f_{MC_2}(\hat{\mathbf{n}}) = g(\theta)h(\phi)$ and $f_{D_2}(\hat{\mathbf{n}}) = D(\hat{\mathbf{n}})g(\theta)h(\phi)$. The first two, MC_1 and MC_2, were generated for eight centrality classes within 0-40% with intervals of 5%. The one with detector anisotropies $D(\hat{\mathbf{n}})$ was created only for 0-5%, 10-15% and 35-40%, in addition to being corrected like Eq. (4.7). They have same input v_n values, each increasing with centrality.

After generating events for each distribution function and centrality mentioned above, $\langle S_\ell^{m\neq 0}\rangle$ were calculated from the difference between ensemble averaged spectra and backgrounds; these estimated for each centrality class, befitting to the underlying $f(\hat{\mathbf{n}})$. Then, v_n for $n = 1, \cdots, 4$ were computed by substituting the corresponding $\langle S_n^{m\neq 0}\rangle$ in Eqs. (5.1, 5.2). As for the Q-cumulants, two-particle correlation functions $\langle 2\rangle$ were calculated for the simulated azimuthal distributions and their values were used to extract $v_n\{2\}$; see Eqs. (2.5) to (2.8).

The results of v_n estimation using the power spectrum are indicated by $v_n\{C_\ell\}$, while for Q-cumulants with two-particle correlations, the same are denoted by $v_n\{2, QC\}$. Both are shown in Fig. 5.9 as a function of centrality, where the dashed lines correspond to the input values and "**Det.**" symbolizes the events under corrected MC with non-uniform detector efficiency. Unsurprisingly, all v_2 estimates in Fig. 5.9 (b) are superposed and, although the results for MC_1, MC_2 and $\overline{f}_{D_2}(\mathbf{n_p})$ spectra and Q-cumulants fluctuate, they do not differ from each other

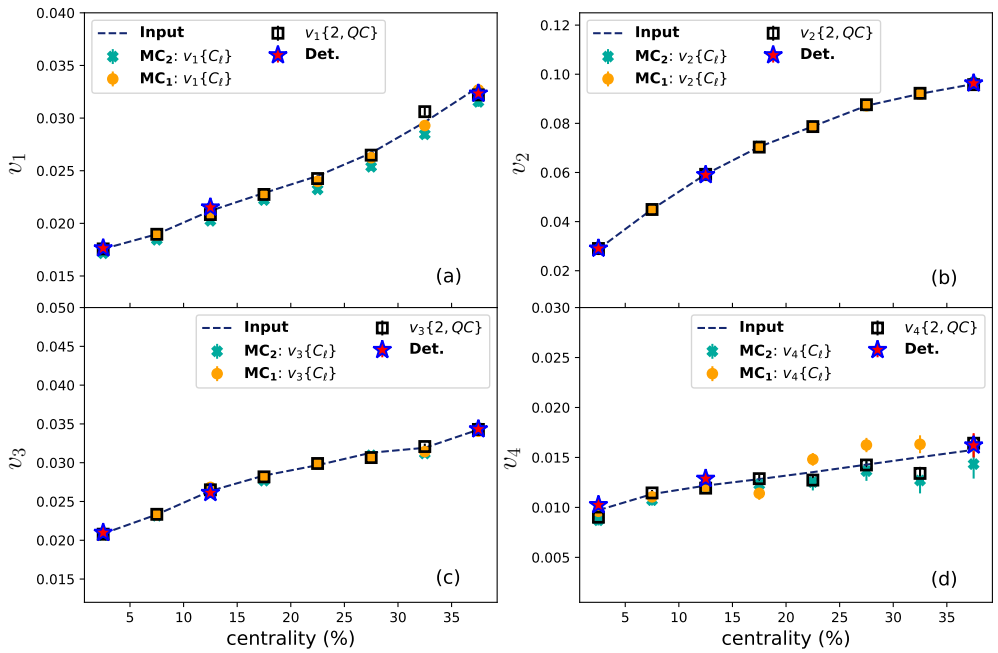

Figure 5.9: Comparison of v_n, $n = 1, \cdots, 4$ for MC distributions calculated through the power spectrum, $v_n\{C_\ell\}$, and the Q-cumulants method with two-particle correlations, $v_n\{2, QC\}$.

significantly. Given that the chosen distributions are purely dominated by flow, these coincident values should be expected.

Originally, the centrality classes for data were divided like the MC simulations above, as seen in [87]. However, the separation in vertex intervals and the analyses of maps with particles selected according to their p_T values (to be discussed soon) made the enlargement of the centrality percentages necessary.

5.3.2 Coefficients from data

Let us begin by making the assumption that heavy ion data maps can be written as $f_z(\mathbf{n_p}) = D_z(\mathbf{n_p})g(\theta_p)h(\phi_p)$, with θ_p and ϕ_p simply representing a pixelation of functions that are uniform in ϕ and θ, respectively. In this scenario, aside from the overall θ distribution, $g(\theta_p)$, events have no other dependence on the polar angle, making their anisotropies entirely azimuthal. After normalizing the data maps by $D_z(\mathbf{n_p})g(\theta_p)$, their corresponding $\overline{f}_z(\mathbf{n_p})$ have a resulting average spectrum $\langle S_\ell^{m\neq0}\rangle$ approximately free from $D_z(\mathbf{n_p})$ and uniform in θ, since $\langle N_\ell^{m\neq0}\rangle$ compensates for the pixel densities. Additionally, their vertex average should also share these characteristics. Then, if $h(\phi_p)$ can be described as a Fourier expansion of flow harmonics, the relation between $\langle S_\ell^{m\neq0}\rangle_z$ and v_n can be given by Eqs. (5.1, 5.2), with $b_{\ell m}$ as an integral of $W(\hat{\mathbf{n}})$ over the sphere; $g(\theta) = 1$ in this case.

The previous paragraph relates the same situation as the MC case with non-uniform detector efficiency tackled in Ch. 4. Its resulting spectrum is seen in Fig. 4.15 compared to the expected $\mathtt{C}_\ell^{m\neq0}$ with equal ϕ dependence and isotropic in θ. Also, its estimated v_n are depicted in Fig. 5.9 as stars and their values do not differ significantly from the other MC cases or the Q-cumulants calculation.

This translation from angular power spectrum $\langle S_\ell^{m\neq0}\rangle_z$ to azimuthal flow coefficients $v_n\{C_\ell\}$ appears in Fig. 5.10 in comparison to Q-cumulants calculations from two-particle correlations: $v_n\{2\}$ is done directly through the implementation of Eqs. (2.5) to (2.8), while $v_n\{2,|\Delta\eta| > 1\}$ requires a pseudorapidity gap of $|\Delta\eta| > 1$ to suppress non-flow effects. The latter is the weighted event ensemble average of Eq. (2.9). Sub-event A has particles with $-0.9 < \eta < -0.5$, while B lies within $0.5 < \eta < 0.9$.

The difference between v_n estimations with and without η gap is basically due to non-flow effects. For instance, the supposedly observed dipole in Fig. 5.10 (a) is null for $v_n\{2,|\Delta\eta| > 1\}$, implying that azimuthal

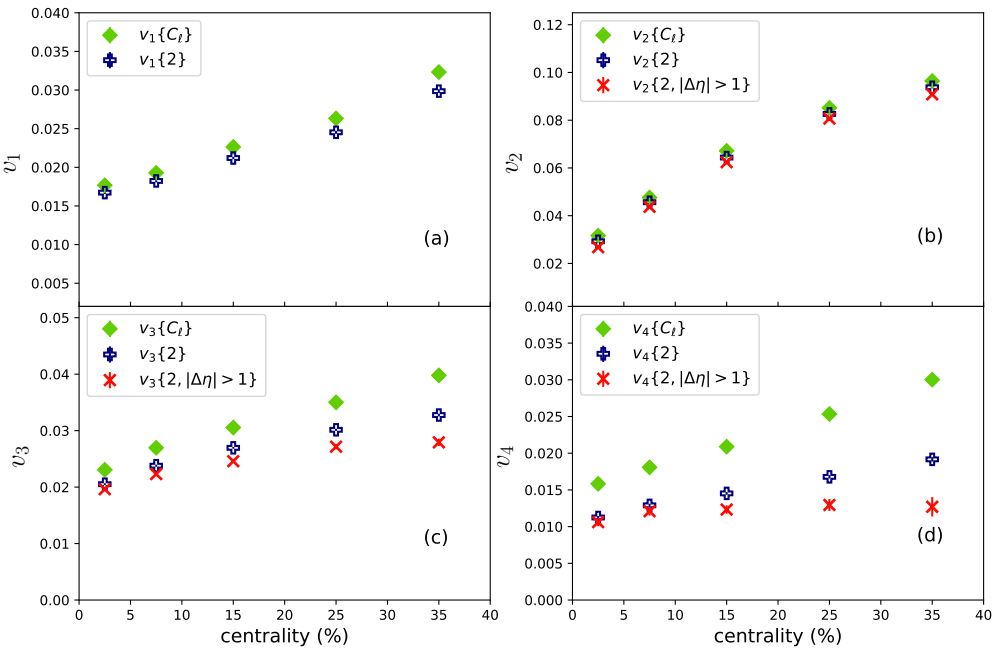

Figure 5.10: Comparison between v_n calculated through the power spectrum $v_n\{C_\ell\}$ and Q-cumulants with a pseudorapidity gap $v_n\{2, |\Delta\eta| > 1\}$ and without it $v_n\{2\}$.

two-particle correlations of the type $\langle e^{i(\phi_1 - \phi_2)} \rangle$ do not relate to a symmetry plane Ψ_1 and are short-ranged in η. Aside from this expected discrepancy, $v_n\{C_\ell\}$ stands above them all.

As previously mentioned, computing a power spectrum is measuring correlations between (θ, ϕ) (pixel) pairs over the whole sphere. Consequently, small scale structures unrelated to flow contribute to $\langle S_\ell^{m\neq 0} \rangle_z$, thus increasing $v_n\{C_\ell\}$ at least in comparison to $v_n\{2, |\Delta\eta| > 1\}$. At the same time, for Q-cumulants without a pseudorapidity gap, the whole particle distribution is simply flattened along the polar direction. As a result, all possible azimuthal pairs are considered, analogously to a spectrum calculation. For this reason,$v_n\{2\}$ and $v_n\{C_\ell\}$ should coincide,

even in a situation where flow is not the sole contributor to azimuthal anisotropies. That is, if an event particle distribution can actually be factorized, i.e., $f(\hat{\mathbf{n}}) = g(\theta)h(\phi)$.

More specifically, imagine that for the phase space at hand, or $|\eta| < 0.9$, a heavy ion event could be transversely cut at a certain θ value. If the distribution in ϕ does not depend on the chosen polar angle, then $a_{\ell m}$ should be a product of integrals: in θ, the result is expressed by the $b_{\ell m}$ modes mentioned before, while in ϕ it becomes $\langle e^{-im\phi} \rangle$. Summing up, the power spectrum calculation of a function $f(\hat{\mathbf{n}}) = g(\theta)h(\phi)$ comprises the net expectation value of $e^{-im\phi}$ over all possible slices in θ, followed by taking its variance over m modes $\langle a^*_{\ell m} a_{\ell m} \rangle$. This is akin to computing azimuthal two-particle correlations.

The difference between v_n results in Fig. 5.10 for $v_n\{2\}$ and $v_n\{C_\ell\}$ suggests that $f(\hat{\mathbf{n}}) \neq g(\theta)h(\phi)$. Alternatively, one could understand the final particle distribution as a superposition of maps: one consisting of large scale geometries, like the almond-shaped overlap region, and another composed of particle clusters, possibly pertaining to resonance decays, quantum correlations. In this case, $|a_{\ell m}|^2$ would receive contributions not only from each of the aforementioned maps, i.e., $|a^A_{\ell m}|^2$ and $|a^B_{\ell m}|^2$, but also their cross-correlation terms, $(a^A_{\ell m})^* a^B_{\ell m}$ and its conjugate; A and B here represent those distinct maps. This plethora of contributions imply that Eqs. (5.1, 5.2) cannot be applied in the estimation of azimuthal flow coefficients.

Another way of looking at this discrepancy in Fig. 5.10 is to realize that the 3-D geometry of non-flow is seen differently through the angular power spectrum and azimuthal two-particle correlations. On that note, $\langle S_\ell^{m\neq 0} \rangle_z$ not only has the influence of primordial lumpiness, but also of late-stage effects like momentum conservation. Furthermore, global azimuthal anisotropies probably dominate $2 \leq \ell \leq 6$, given the similarities to the MC-spectra, while sources of particle clustering might be responsible for the damping tail at $\ell \geq 7$. Regarding the relatively high dipole ($\ell = 1$), Q-cumulants calculations with $|\Delta\eta| > 1$ have shown that it is not

related to directed flow.

At this point, there should be a general understanding on how to estimate an angular power spectrum of heavy ions as well as which effects could be responsible for its features. The next step in this investigation tackles the still-not-covered transverse momentum, where the maps dealt with so far will be split accordingly.

5.4 Transverse momentum and the spectrum

The overall geometry of the emitted particles changes with their transverse momentum. Clearly shown by measurements of azimuthal flow as a function of p_T, like in Fig. 2.9. Nevertheless, the analysis so far has only considered the angular coordinates of particles, while completely disregarding their momenta. It was mentioned before that the limit imposed on p_T for the data set at hand [9] is $0.15 < p_T < 100$ GeV [10]. Within such wide range, the measured spectra above may comprise all sorts of effects, like clusters of low-p_T particles originated from hadron decays and high momentum jets.

The study of power spectrum dependence on transverse momentum follows a rather simple approach: each event is split in two distributions according to its particles p_T coordinates, one side with $p_T > 0.54$ GeV and another with $p_T < 0.54$ GeV. This choice of interval results in both halves having approximately the same multiplicities, which is the only way to maximize the number of particles for these newly created sub-events. Besides that, making more partitions in p_T could compromise the spectrum estimation, since low event multiplicity increases the number of unfilled pixels and, consequently, the uncertainties on $a_{\ell m}$ calculation.

As usual, a vertex interval is selected along with a centrality class pertaining to it. At this point, the event is divided into the aforementioned transverse momentum ranges. Then, each of the formed sub-events follows steps **(i-ix)** separately, yielding *two* averaged angular power spec-

tra, $\langle S_\ell^{m\neq 0}\rangle_{Uz}$ for $p_T > 0.54$ GeV and $\langle S_\ell^{m\neq 0}\rangle_{Lz}$ for $p_T < 0.54$ GeV. It should be remarked that U and L stand for *upper* and *lower* p_T bounds, respectively. Also, the spectra are averaged over all vertex intervals.

In this new scenario, the original event map is simply the superposition of two distinct angular distributions, i.e., $f(\mathbf{n_p}) = f_U(\mathbf{n_p}) + f_L(\mathbf{n_p})$, representing the maps for $p_T > 0.54$ GeV and $p_T < 0.54$ GeV, respectively. As a consequence, $a_{\ell m}$ will also be a sum of the spherical coefficients of each p_T-bound map. At any rate, what matters in the power spectrum calculation is the absolute square value of the harmonics:

$$|a_{\ell m}|^2 = |a_{\ell m}^U|^2 + |a_{\ell m}^L|^2 + (a_{\ell m}^U)^* \cdot a_{\ell m}^L + a_{\ell m}^U \cdot (a_{\ell m}^L)^*. \tag{5.3}$$

The terms in Eq. (5.3) can be averaged over m and divided by $2\ell + 1$. This final expression shows that the full spectrum presented in the sections above receives contributions from $\langle S_\ell^{m\neq 0}\rangle_{Uz}$, $\langle S_\ell^{m\neq 0}\rangle_{Lz}$ as well as a cross term between both sub-event maps. For estimating the latter, only stages **(i-v)** are necessary, i.e., there is no "cross-background". Since the multiplicity corrections for each p_T-bound map are independent of each other, their associated cross terms are null.

Results for the $p_T > 0.54$ GeV and $p_T < 0.54$ GeV spectra, in addition to their cross term are depicted in Fig. 5.11 for the 10-20% centrality class. Notably, there is a change in dominance from $\langle S_\ell^{m\neq 0}\rangle_{Uz}$ to $\langle S_\ell^{m\neq 0}\rangle_{Lz}$ after $\ell = 4$. This is a consequence of large scale geometries tending to become more accentuated at higher p_T, i.e., of anisotropies quantified by v_n generally increasing with transverse momentum. What it more, the peaks in $\ell = 2, 6, 10$ for $\langle S_\ell^{m\neq 0}\rangle_{Uz}$ are sharper in comparison to the spectrum at full p_T range in Fig. 5.7 (b). On the other hand, $\langle S_\ell^{m\neq 0}\rangle_{Lz}$ has an ever decreasing flat tail from $\ell = 3$. If particles with $p_T < 0.54$ GeV were fully isotropic, the spectrum would have much lower values and large uncertainties, due to its closeness to the background. Therefore, the composing distributions of $\langle S_\ell^{m\neq 0}\rangle_{Lz}$ are probably made of tiny particle clusters with an overall degree of elliptic eccentricity, hence the high

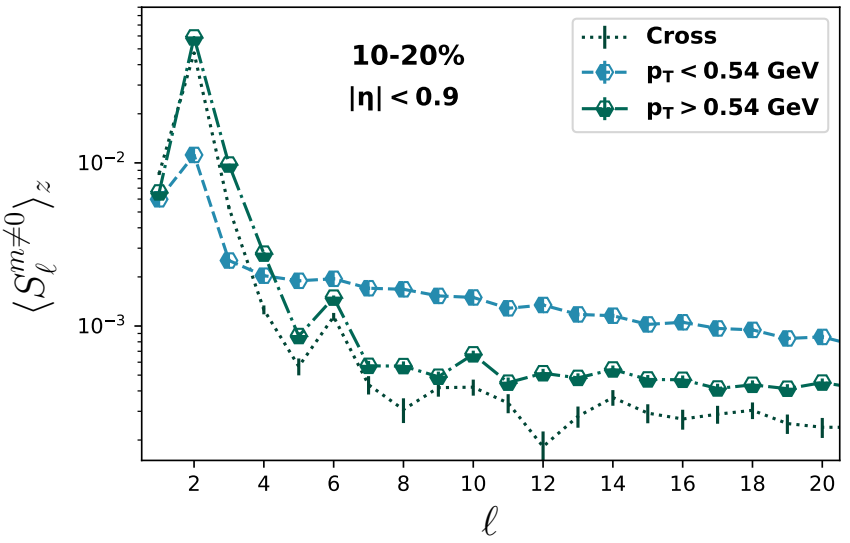

Figure 5.11: Comparison between spectra for the lower and upper p_T intervals and their cross term from Eq. (5.3).

$\ell = 2$.

Altogether, particles with $p_T < 0.54$ GeV form small scale structures, while the ones with $p_T > 0.54$ GeV make up the bulk of large scale anisotropies. As for the cross term, despite its features not being well understood, its existence demonstrates that particles from the upper and lower p_T bounds are correlated to each other, i.e., not independent, which is expected since both sides originate from the same heavy ion collision and underwent collective expansion. Lastly, if the full p_T-range $\langle S_\ell^{m\neq 0}\rangle_z$ is to be recovered, the spectra in Fig. 5.11 should be added and divided by four, reason being that in Eq. (5.3) the cross term contributes with a weight of two.

Akin to the spectrum within full transverse momentum phase space, we follow up by verifying how $\langle S_\ell^{m\neq 0}\rangle_{Uz}$ and $\langle S_\ell^{m\neq 0}\rangle_{Lz}$ change with centrality. The results are displayed in Fig. 5.12 (a) and (b), respectively.

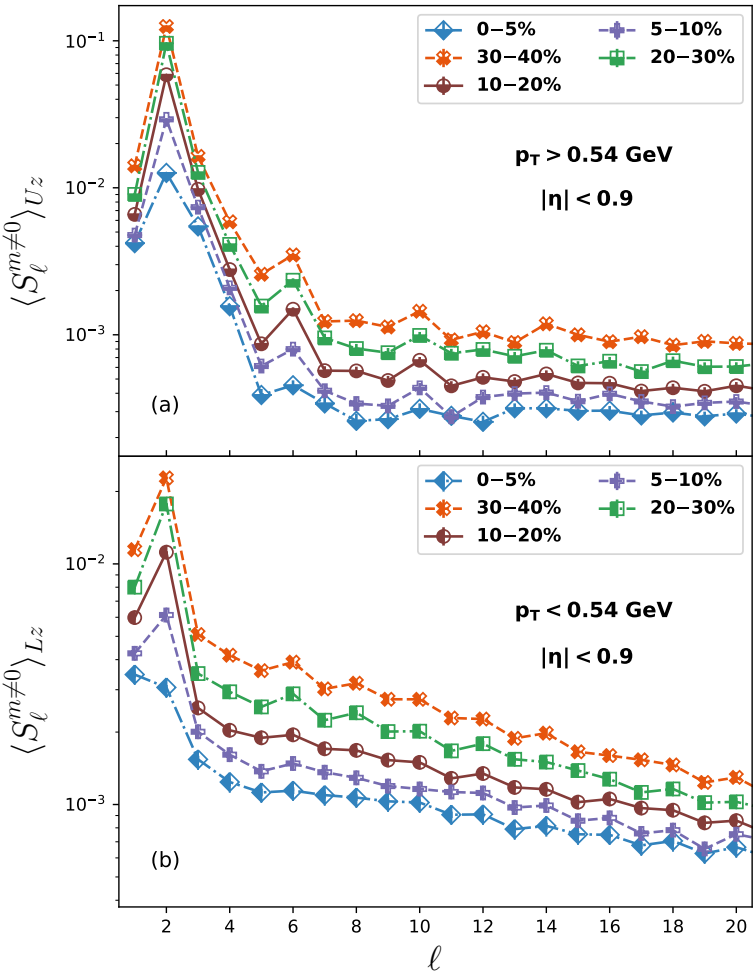

Figure 5.12: Spectra of distributions within $p_T > 0.54$ GeV (a) and $p_T < 0.54$ GeV (b) as they change with centrality.

Overall, the spectral hierarchy remains, with values increasing as collisions become more peripheral. As discussed before, the main cause are the initial anisotropies arising when the nuclei first interact. Next, we tackle each p_T interval separately and comment on their differences to

$\langle S_\ell^{m\neq 0}\rangle_z$.

For particle distributions with $p_T > 0.54$ GeV, the spectrum features are much sharper at $\ell \leq 6$, while at higher ℓ they seem to become approximately constant. This plateau means that the size of fluctuations is not changing as angular distances decrease. The method could have reached its limit for $\ell > 10$ in this particular case. Further, the peaks at $\ell = 10$ were barely discernible in $\langle S_\ell^{m\neq 0}\rangle_z$ and now appear more prominently. A quick calculation of $v_n\{C_\ell\}$ turned out in the same way as Fig. 5.10 when compared to Q-cumulants. Since phenomena unrelated to flow are still present in the current phase space, this result is expected.

Moving to the other side where $p_T < 0.54$ GeV, the damping tails become more slanted than in $\langle S_\ell^{m\neq 0}\rangle_z$. The peak in $\ell = 6$ has basically merged with the other modes. Still, the peak at $\ell = 2$ remains, except for 0-5%. Its presence suggests that low momentum particles are arranged into the elliptic structure characteristic of the overlapping region. Moreover, $\ell = 1$ standing above $\ell = 2$ for 0-5% further supports low-p_T particles having a geometry associated with local phenomena, as the almond-shape became suppressed.

The tails of $\langle S_\ell^{m\neq 0}\rangle_{Lz}$ seem to decay with a power law so, out of curiosity, a fit to the function $P_{ow}(\ell) = \mathcal{A}\cdot\ell^{-\gamma}$ was performed for modes within $3 \leq \ell \leq 20$ on the spectra of all centralities. Since $\mathcal{A}$ is just a scaling factor, only the exponent γ is plotted as it changes with centrality; see Fig. 5.13. Since γ increases with centrality percentile, the size of fluctuations decreases faster for peripheral centralities in comparison to central ones. This could be explained through rarefaction of the medium: a domino effect of interactions is more probable in a denser system, thus creating a plethora of particle clusters with all sorts of sizes. Peripheral collisions would return less clusters, so its tail would dampen faster.

Taking momentum conservation to be the emission of particles on opposite sides of a sphere, one can see through spherical harmonics $Y_{\ell m}$, that only ℓ even possess such symmetry. Consequently, the resulting spectrum would have enhanced even modes. This characteristic can

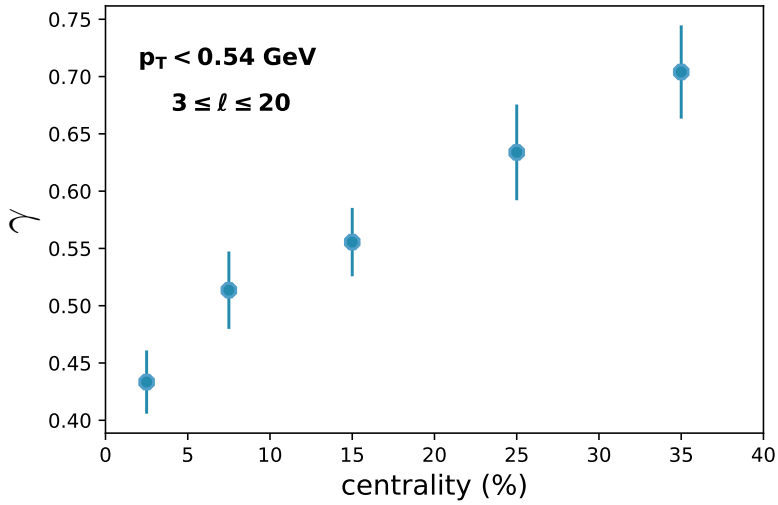

Figure 5.13: Power law exponent γ as a function of centrality.

be seen slightly in $\langle S_\ell^{m\neq 0}\rangle_{Lz}$ for the 30-40% and 20-30% centralities in Fig. 5.12 (b). Their sparsity allows for the particles to travel without much medium interaction.

All data spectra exhibit a relatively high dipole moment ($\ell = 1$), no matter the centrality. When separating the transverse momentum phase space, the $\ell = 1$ sit quite close to each other, with $p_T > 0.54$ GeV slightly higher; see Fig. 5.11. This global geometry is connected to Y_{11} and Y_{1-1} which indicate net asymmetry in ϕ. Since not all particles can be accounted for due to limited detector acceptance, that could be the cause for such enhancement. A single emitted jet while its partner got swallowed by the medium also contributes to the dipole.

These p_T spectra are more extreme versions of the full one: with $\langle S_\ell^{m\neq 0}\rangle_{Uz}$ having rather accentuated peaks and $\langle S_\ell^{m\neq 0}\rangle_{Uz}$ a more oblique tail. They show that the geometry of distributions change with transverse momentum. For the higher p_T interval, primordial anisotropies associated with v_n dominate, as it is composed by particles that man-

aged to escape after expansion without much interaction. In contrast, low p_T distributions are mainly characterized by non-flow effects, with their typical sizes decreasing with smaller angular scale.

Given the results in this chapter, the method developed for power spectrum estimation seems to have been successful. We refer to the resulting $\langle S_\ell^{m\neq 0}\rangle_z$ in Fig. 5.7 (b) when different interval widths, $dz = 2$ cm and $dz = 1$ cm, were chosen, and the use of Eq. (5.3) to recover the aforementioned spectrum. In light of these outcomes, we saw that $\langle S_\ell^{m\neq 0}\rangle_z$ encodes a plethora of geometries which arise from the collisions of nuclei and their collective expansion. From effects of azimuthal flow to momentum conservation and hadron decays, among possible others. The angular power spectrum also sees these structures differently than two-particle azimuthal correlations and further suggests that an event described by $f(\hat{\mathbf{n}})$ cannot easily be decomposed into a product $g(\theta)h(\phi)$, implying that what happens along rapidity might not be so trivial after all.

6 Conclusion

"With magic, you can turn a frog into a prince. With science, you can turn a frog into a Ph.D and you still have the frog you started with."

— Terry Pratchett, *The Science of Discworld*

This work tackled the anisotropies found in particles emitted from heavy ion collisions as a sum of different spherical geometries $Y_{\ell m}$. The latter's mean contributions at each ℓ were readily quantified by the angular power spectrum. The diversity of two-particle correlation sources imply that $\langle S_\ell^{m\neq 0}\rangle_z$ encodes a plethora of geometries. This final chapter starts by highlighting the main features found in the full phase space spectra and in the ones pertaining to different p_T intervals. Secondly, $\langle S_\ell^{m\neq 0}\rangle_z$ is discussed in comparison to other measurements of event anisotropies, most of them mentioned in Ch. 2. Finally, the limitations of the analysis are discussed, as well as its future prospects.

6.1 Highlights

Even before spectra were corrected by $\langle N_\ell^{m\neq0}\rangle$, their most striking characteristic was already in full view: the peak at $\ell = 2$; Fig. 5.6. This enhanced quadrupole mode is followed by decreasing $\langle S_\ell^{m\neq0}\rangle_z$ until the second peak at $\ell = 6$. From this point on the power spectrum values become smaller with higher ℓ. In addition, a dipole $\ell = 1$ comparable to fluctuations at $\ell = 3$ is observed; see Fig. 5.7.

There is a hierarchy of centralities when it comes to the resulting spectrum: $\langle S_\ell^{m\neq0}\rangle_z$ values increase as collisions become peripheral. The same aforementioned features are present in all spectra, with the exception of 0-5%. In this case, the peak at $\ell = 6$ is non-existent. Furthermore, the ratio of $\langle S_2^{m\neq0}\rangle_z$ to other modes for the 0-5% spectrum is approximately half of that same ratio for 10-20%, 20-30% and 30-40%. The $\langle S_\ell^{m\neq0}\rangle_z$ spectra in Fig. 5.8 start decreasing at the same angular scale, though the size of fluctuations varies.

When the transverse momentum phase space was divided, the typical anisotropies pertaining to each side of the interval came to light. In Fig. 5.11 both spectra retain the peak at $\ell = 2$ and have close dipole values. At the same time, the fluctuations of $\langle S_\ell^{m\neq0}\rangle_{Uz}$ for $p_T > 0.54$ GeV dominate at $\ell \leq 4$, with the opposite happening for $\ell \geq 5$. The spectrum from the upper p_T-bound has peaks also at $\ell = 6$ and $\ell = 10$, then it seems to flat out for $\ell \geq 11$. On the other hand, $\langle S_\ell^{m\neq0}\rangle_{Lz}$ differs more from the full-p_T spectrum than its counterpart: from $\ell = 3$ it has a damping tail decaying with a power law.

Turning to the variation of $\langle S_\ell^{m\neq0}\rangle_{Uz}$ and $\langle S_\ell^{m\neq0}\rangle_{Lz}$ with centrality, the hierarchy is present in both, as well as the ℓ interval that each dominate. Looking at $\langle S_\ell^{m\neq0}\rangle_{Uz}$ in Fig. 5.12 (a), the 0-5% spectrum now has a peak at $\ell = 6$. Meanwhile, the 30-40% spectrum seems to have an additional peak at $\ell = 14$. In spite of that, all spectra seem to become approximately flat for $\ell \geq 11$. In the case of $\langle S_\ell^{m\neq0}\rangle_{Lz}$, the dipole surpasses $\ell = 2$ for 0-5%. The spectra for 20-30% and 30-40% display a relative enhancement

of even modes from $\ell = 6$ until $\ell = 12$ and $\ell = 14$, respectively. All tails start at $\ell = 3$ and fit $P_{ow}(\ell) \propto \ell^{-\gamma}$, with γ linearly increasing with centrality percentile.

In the subsequent section, the possible reasons for such features will be discussed alongside previous observations of anisotropies in heavy ions.

6.2 Discussion

The spectra obtained from Monte Carlo simulations in Ch. 4 possess striking similarity to $\langle S_\ell^{m\neq 0}\rangle_z$ for $\ell \leq 6$. In light of the input v_n values from Table. 4.1 and the expressions for their harmonic coefficients $|a_{\ell n}|^2 \propto v_n^2$, one may conclude that $\ell = 2$ becomes enhanced due to v_2. Applying this statement to data, $\langle S_\ell^{m\neq 0}\rangle_z$ has an imprint from the almond-shaped nuclei overlap region. Additionally, with $3 \leq \ell \leq 6$ relatively higher than other modes, the spectrum could encompass other azimuthal anisotropies related to flow.

The Fourier harmonics v_n are calculated from $\langle S_\ell^{m\neq 0}\rangle_z$ under the assumption that the underlying distribution function is of the type $f(\hat{\mathbf{n}}) = g(\theta)h(\phi)$, with v_n and Ψ_n approximately constant within $|\eta| < 0.9$. Given that the power spectrum quantifies the (θ, ϕ)-pair correlation as a function of angular scale, one would expect that $v_n\{C_\ell\} \approx v_n\{2\}$. However, Fig. 5.10 contradicts the previous sentence, suggesting that $\langle S_\ell^{m\neq 0}\rangle_z$ tackles anisotropies differently than solely azimuthal two-particle correlations. Likewise, the discrepancy between v_n breaks the initial assumption on $f(\hat{\mathbf{n}})$.

What the comparisons of flow estimation did not subdue was the centrality hierarchy of v_n. Similarly to the ALICE results in Fig. 2.8 (a), $\langle S_\ell^{m\neq 0}\rangle_z$ as well as its associated flow values increase from 0-5% to 30-40%. Furthermore, $\langle S_2^{m\neq 0}\rangle_z > \langle S_3^{m\neq 0}\rangle_z > \langle S_4^{m\neq 0}\rangle_z$, akin to what happens with $v_n\{2\}$ and $v_n\{2, |\Delta\eta| > 1\}$.

In comparison to how flow coefficients change with pseudorapidity, it should be reminded that $\langle S_\ell^{m\neq0}\rangle_z$ does not apply θ-gaps. As a result, it tackles longitudinal anisotropies differently than the $v_n(\eta)$ calculations in Fig. 2.10. At the same time, if $\Psi_n(\eta)$ it could explain why the v_n extraction through power spectrum was distinct from the two-particle correlation Q-cumulants. However, CMS measurements were done for centralities from 55% to 67%, much beyond our scope.

Differential flow $v_n(p_T)$ has an overall tendency to increase with transverse momentum until a certain value, see Fig. 2.9, its damping occurring due to shear viscosity. Accordingly, for $p_T < 0.54$ GeV the influence of azimuthal flow harmonics dwindles significantly. This establishes the dominance of other two-particle correlation sources in $\langle S_\ell^{m\neq0}\rangle_{Lz}$, making the spectra in Fig. 5.12 (b) measurements of non-flow fluctuations. The relative enhancement of even modes in 20-30% and 30-40% suggests that $Y_{\ell m}$ with even ℓ have larger contribution than the others. The typical shape of these $Y_{\ell m}$ is characterized by symmetries between diametrically opposite points. Altogether, the bumps in $6 \leq \ell \leq 12$ (or 14, if 30-40%) could indicate momentum conservation.

In opposition to the spectrum discussed above, $\langle S_\ell^{m\neq0}\rangle_{Uz}$ is probably more influenced by fluctuations from initial conditions. At large scales ($\ell \leq 6$), its values are overall higher in comparison to the full-p_T spectrum. Looking back at the angular two-particle correlation functions $C(\Delta\phi, \Delta\eta)$ in Fig. 2.11, small range $(\Delta\phi, \Delta\eta) \approx 0$ correlations are also at play for $p_T > 0.54$ GeV. Notice how the peak at small angular separation increases with centrality percentile. This provides a reasonable explanation for the $\langle S_\ell^{m\neq0}\rangle_{Uz}$ values when it becomes flat ($\ell \geq 11$). Curiously, the Fourier transform of a Dirac delta is a constant. Given that the power spectrum itself is the Fourier transform of the correlation function, then it makes sense that the spectra would flatten out with smaller scales.

All the observed spectra have a relatively high dipole, comparable to the modes dominated by primordial fluctuations. This net asymmetry in the azimuthal direction is also observed by $v_n\{2\}$. Still $v_1\{2, |\Delta\eta| > 1\} = 0$,

so this anisotropy is not related to Ψ_1, and it is short-ranged in η (θ). Considering the configuration of $C(\Delta\phi, \Delta\eta)$, this asymmetry could be caused by the peak in $(\Delta\phi, \Delta\eta) \approx 0$ in opposition to the far side ridge when $\Delta\eta \approx 0$. There is an abundance of short-range (θ, ϕ) correlations relative to flow. Also, back-to-back jets are not necessarily diametrically opposed, which could add to $\langle S_\ell^{m\neq 0} \rangle_z$.

This last paragraph traces a parallel between the CMB damping tail and the heavy ion one for $p_T < 0.54$ GeV. The CMB spectrum decreases with $\ell \gtrsim 800$, because the scale of these fluctuations is comparable to the mean free path of photons; from Sec. 3.3. Diffusion, in turn, equalizes temperatures and dampens anisotropies. The lack of structure associated with flow in $\langle S_\ell^{m\neq 0} \rangle_{Lz}$ does indicate smoothed out primordial anisotropies. Stretching the analogy, the spectrum would be damped on scales smaller than the mean free path of low momentum hadrons. Such scales seem to be at $\ell = 3$, associated with an angular separation of $\sim 60^o$. In the end, these statements are mere speculation and further investigations are necessary.

6.3 Shortcomings and future prospects

One of the main limitations of angular power spectrum estimation lies in the event multiplicities. As the latter decreases, maps have less filled pixels, thus making necessary to lower the resolution. Consequently, $a_{\ell m}$ calculations become less accurate and precise. The limitation imposed by multiplicity constrains the following analyses of $\langle S_\ell^{m\neq 0} \rangle_z$: high transverse momentum $p_T > 2$ GeV, different particle species (with the possible exception of pions) and p-Pb and p-p collision systems. Precisely due to multiplicity limitations on the aforementioned analyses, separating the causes of anisotropies could prove to be challenging.

As means of enriching this study, the complete analysis should be ap-

plied to a 3+1-D heavy ion model. A Multi-Phase Transport (AMPT) [91] model would be a viable first option, since it runs faster than hydrodynamics 3+1-D. An evaluation of the ensemble averaged $|a_{\ell m}|^2$ could also shed light on the contribution of different spherical harmonics to the anisotropies. They could be corrected by multiplicity through the subtraction of a mean $|n_{\ell m}|^2$, these being the coefficients of $\langle N_\ell^{m\neq 0}\rangle$. Another possible line of investigation could be the p_T cross term from Eq. (5.3), since its implications are not fully understood beyond the recovery of the full-p_T spectrum.

The quark-gluon plasma production at colliders is often linked to the early universe after inflation. Curiously, the typical scales of anisotropies in heavy ions are much larger ($\ell < 20$) than the CMB ones ($\ell > 100$), in spite of the QGP size in comparison to the universe at recombination. The peaks of the heavy ion spectrum indicate the initial almond-like geometry, while the CMB peaks provide information on the curvature of the universe and matter densities.

References

[1] A. A. Penzias and R. W. Wilson, "A Measurement of Excess Antenna Temperature at 4080 Mc/s.", APJ **142**, 419 (1965).

[2] I. Arsene et al., "Quark gluon plasma and color glass condensate at RHIC? The Perspective from the BRAHMS experiment", Nucl. Phys. **A757**, 1 (2005).

[3] B. B. Back et al., "The PHOBOS perspective on discoveries at RHIC", Nucl. Phys. **A757**, 28 (2005).

[4] J. Adams et al., "Experimental and theoretical challenges in the search for the quark gluon plasma: The STAR Collaboration's critical assessment of the evidence from RHIC collisions", Nucl. Phys. **A757**, 102 (2005).

[5] K. Adcox et al., "Formation of dense partonic matter in relativistic nucleus-nucleus collisions at RHIC: Experimental evaluation by the PHENIX collaboration", Nucl. Phys. **A757**, 184 (2005).

[6] R. Snellings, "Elliptic flow measurements from STAR", Acta Phys. Hung. **A21**, [Frascati Phys. Ser.30(2003)], 237 (2004).

[7] K. Aamodt et al., "Elliptic flow of charged particles in Pb-Pb collisions at 2.76 TeV", Phys. Rev. Lett. **105**, 252302 (2010).

[8] J. Adam et al., "Anisotropic flow of charged particles in Pb-Pb collisions at $\sqrt{s_{\mathrm{NN}}} = 5.02$ TeV", Phys. Rev. Lett. **116**, 132302 (2016).

[9] ALICE Collaboration, *Pb-Pb data sample at* 2.76TeV *from run number 139465. CERN Open Data Portal.* `http://opendata.cern.ch/record/1106`.

[10] C. Bourjau, *mALICE: An open source framework for analyzing ALICE's Open Data*, 2018–.

[11] R. Snellings, "Elliptic Flow: A Brief Review", New J. Phys. **13**, 055008 (2011).

[12] W. Busza, K. Rajagopal, and W. van der Schee, "Heavy Ion Collisions: The Big Picture and the Big Questions", Annual Review of Nuclear and Particle Science **68**, 339 (2018).

[13] A. Bilandzic, R. Snellings, and S. Voloshin, "Flow analysis with cumulants: Direct calculations", Phys. Rev. **C83**, 044913 (2011).

[14] A. Mazeliauskas, "Initial conditions for nuclear collisions: theory overview", Nuclear Physics A **982**, The 27th International Conference on Ultrarelativistic Nucleus-Nucleus Collisions: Quark Matter 2018, 134 (2019).

[15] E. Iancu and R. Venugopalan, in *Quark-gluon plasma 4*, edited by R. C. Hwa and X.-N. Wang (2003), pp. 249–3363.

[16] Utrecht University, Institute for Subatomic Physics, *Color-Glass Condensate*.

[17] L. McLerran, "A Brief Introduction to the Color Glass Condensate and the Glasma", in Proceedings, 38th International Symposium on Multiparticle Dynamics (ISMD 2008): Hamburg, Germany, September 15-20, 2008 (2009), pp. 3–18.

[18] A. Kovner, L. McLerran, and H. Weigert, "Gluon production at high transverse momentum in the McLerran-Venugopalan model of nuclear structure functions", Phys. Rev. D **52**, 3809 (1995).

[19] A. Kovner, L. McLerran, and H. Weigert, "Gluon production from non-Abelian Weizsäcker-Williams fields in nucleus-nucleus collisions", Phys. Rev. D **52**, 6231 (1995).

[20] A. Krasnitz and R. Venugopalan, "Initial Energy Density of Gluons Produced in Very-High-Energy Nuclear Collisions", Phys. Rev. Lett. **84**, 4309 (2000).

[21] A. Krasnitz and R. Venugopalan, "Initial Gluon Multiplicity in Heavy-Ion Collisions", Phys. Rev. Lett. **86**, 1717 (2001).

[22] T. Lappi and L. McLerran, "Some features of the glasma", Nuclear Physics A **772**, 200 (2006).

[23] W. Li, "Collective flow from AA, pA to pp collisions – Toward a unified paradigm", Nuclear Physics A **967**, The 26th International Conference on Ultra-relativistic Nucleus-Nucleus Collisions: Quark Matter 2017, 59 (2017).

[24] Y. Zhou, "Collective Effects in Nuclear Collisions: Experimental Overview", Nuclear Physics A **982**, The 27th International Conference on Ultrarelativistic Nucleus-Nucleus Collisions: Quark Matter 2018, 71 (2019).

[25] P. Romatschke, "Do nuclear collisions create a locally equilibrated quark–gluon plasma?", The European Physical Journal C **77**, 21 (2017).

[26] P. Huovinen and P. Petreczky, "QCD equation of state and hadron resonance gas", Nuclear Physics A **837**, 26 (2010).

[27] M. Luzum and P. Romatschke, "Conformal relativistic viscous hydrodynamics: Applications to RHIC results at $\sqrt{s_{NN}} = 200$ GeV", Phys. Rev. C **78**, 034915 (2008).

[28] P. K. Kovtun, D. T. Son, and A. O. Starinets, "Viscosity in Strongly Interacting Quantum Field Theories from Black Hole Physics", Phys. Rev. Lett. **94**, 111601 (2005).

[29] H. B. Meyer, "Calculation of the Bulk Viscosity in SU(3) Gluodynamics", Phys. Rev. Lett. **100**, 162001 (2008).

[30] T. Lee, "The strongly interacting quark–gluon plasma and future physics", Nuclear Physics A **750**, Quark-Gluon Plasma. New Discoveries at RHIC: Case for the Strongly Interacting Quark-Gluon Plasma. Contributions from the RBRC Workshop held May 14-15, 2004, 1 (2005).

[31] I. Arsene et al., "Quark–gluon plasma and color glass condensate at RHIC? The perspective from the BRAHMS experiment", Nuclear Physics A **757**, First Three Years of Operation of RHIC, 1 (2005).

[32] Y. Aoki et al., "The order of the quantum chromodynamics transition predicted by the standard model of particle physics", Nature **443**, 675 (2006).

[33] A. Bazavov et al., "Equation of state in $(2+1)$-flavor QCD", Phys. Rev. D **90**, 094503 (2014).

[34] Nuclear Physics European Collaboration Committee, *NuPECC Long Range Plan 2017: Perspectives of Nuclear Physics*.

[35] S. Voloshin and Y. Zhang, "Flow study in relativistic nuclear collisions by Fourier expansion of azimuthal particle distributions", Zeitschrift für Physik C Particles and Fields **70**, 665 (1996).

[36] A. M. Poskanzer and S. A. Voloshin, "Methods for analyzing anisotropic flow in relativistic nuclear collisions", Phys. Rev. C **58**, 1671 (1998).

[37] P. Danielewicz and G. Odyniec, "Transverse momentum analysis of collective motion in relativistic nuclear collisions", Physics Letters B **157**, 146 (1985).

[38] R. Bhalerao, N. Borghini, and J.-Y. Ollitrault, "Analysis of anisotropic flow with Lee–Yang zeroes", Nuclear Physics A **727**, 373 (2003).

[39] R. S. Bhalerao, N. Borghini, and J. Y. Ollitrault, "Genuine collective flow from Lee-Yang zeroes", Phys. Lett. **B580**, 157 (2004).

[40] N. Borghini, P. M. Dinh, and J.-Y. Ollitrault, "A New method for measuring azimuthal distributions in nucleus-nucleus collisions", Phys. Rev. **C63**, 054906 (2001).

[41] N. Borghini, P. M. Dinh, and J.-Y. Ollitrault, "Flow analysis from multiparticle azimuthal correlations", Phys. Rev. **C64**, 054901 (2001).

[42] A. Bilandzic et al., "Generic framework for anisotropic flow analyses with multiparticle azimuthal correlations", Phys. Rev. **C89**, 064904 (2014).

[43] B. Alver, *Measurement of Non-flow Correlations and Elliptic Flow Fluctuations in Au+Au collisions at RHIC*, `https://www.bnl.gov/rhic_ags/users_meeting/Past_Meetings/2010/agenda/Thurs/Alver.pdf`, June 2010.

[44] B. Alver and G. Roland, "Collision-geometry fluctuations and triangular flow in heavy-ion collisions", Phys. Rev. C **81**, 054905 (2010).

[45] J. Adam et al., "Anisotropic Flow of Charged Particles in Pb-Pb Collisions at $\sqrt{s_{NN}} = 5.02$ TeV", Phys. Rev. Lett. **116**, 132302 (2016).

[46] B. B. Abelev et al., "Multiparticle azimuthal correlations in p -Pb and Pb-Pb collisions at the CERN Large Hadron Collider", Phys. Rev. **C90**, 054901 (2014).

[47] Y. Zhou et al., "Anisotropic distributions in a multiphase transport model", Phys. Rev. **C93**, 034909 (2016).

[48] J. Noronha-Hostler, M. Luzum, and J.-Y. Ollitrault, "Hydrodynamic predictions for 5.02 TeV Pb-Pb collisions", Phys. Rev. **C93**, 034912 (2016).

[49] H. Niemi, K. J. Eskola, R. Paatelainen, and K. Tuominen, "Predictions for 5.023 TeV Pb + Pb collisions at the CERN Large Hadron Collider", Phys. Rev. **C93**, 014912 (2016).

[50] C. Adler et al., "Elliptic flow from two and four particle correlations in Au+Au collisions at s(NN)**(1/2) = 130-GeV", Phys. Rev. **C66**, 034904 (2002).

[51] M. Luzum and J.-Y. Ollitrault, "Eliminating experimental bias in anisotropic-flow measurements of high-energy nuclear collisions", Phys. Rev. **C87**, 044907 (2013).

[52] A. M. Sirunyan et al., "Pseudorapidity and transverse momentum dependence of flow harmonics in pPb and PbPb collisions", Phys. Rev. **C98**, 044902 (2018).

[53] P. Bozek, W. Broniowski, and J. Moreira, "Torqued fireballs in relativistic heavy-ion collisions", Phys. Rev. **C83**, 034911 (2011).

[54] G. Aad et al., "Measurement of the azimuthal anisotropy for charged particle production in $\sqrt{s_{NN}}$ = 2.76 TeV lead-lead collisions with the ATLAS detector", Phys. Rev. **C86**, 014907 (2012).

[55] M. A. Lisa, S. Pratt, R. Soltz, and U. Wiedemann, "Femtoscopy in relativistic heavy ion collisions", Ann. Rev. Nucl. Part. Sci. **55**, 357 (2005).

[56] M. Aaboud et al., "Measurement of jet fragmentation in Pb+Pb and pp collisions at $\sqrt{s_{\mathrm{NN}}}$ = 2.76 TeV with the ATLAS detector at the LHC", Eur. Phys. J. **C77**, 379 (2017).

[57] B. Alver and G. Roland, "Collision geometry fluctuations and triangular flow in heavy-ion collisions", Phys. Rev. **C81**, [Erratum: Phys. Rev.C82,039903(2010)], 054905 (2010).

[58] J. L. Nagle and W. A. Zajc, "Small System Collectivity in Relativistic Hadronic and Nuclear Collisions", Ann. Rev. Nucl. Part. Sci. **68**, 211 (2018).

[59] R. M. Howard, *A Signal Theoretic Introduction to Random Processes* (John Wiley & Sons, July 2015).

[60] S. V. Vaseghi, *Advanced Digital Signal Processing and Noise Reduction*, 2nd Edition (John Wiley & Sons, 2000).

[61] R. Priemer, *Introductory Signal Processing* (WORLD SCIENTIFIC, 1990).

[62] S. L. Kramer, *Geotechnical Earthquake Engineering* (Prentice Hall, Upper Saddle River, N.J., U.S.A., 1996).

[63] E. W. Weisstein, *Wiener- Khinchin Theorem. From MathWorld—A Wolfram Web Resource*, http://mathworld.wolfram.com/Wiener-KhinchinTheorem.html.

[64] D. Samtleben, S. Staggs, and B. Winstein, "The Cosmic Microwave Background for Pedestrians: A Review for Particle and Nuclear Physicists", Annual Review of Nuclear and Particle Science **57**, 245 (2007).

[65] D. Armet, *3 Surface Harmonics at $l = 6$ $m = 0$, $l = 6$ $m = 3$, $l = 6$ $m = 6$*, https://gong.nso.edu/gallery/disk2k10/data/resource/harmonics/modes2.jpg, 2017.

[66] G. F. Smoot et al., "Structure in the COBE differential microwave radiometer first-year maps", APJL **396**, L1 (1992).

[67] Bennett, C. L., et.al., "Nine-year Wilkinson Microwave Anisotropy Probe (WMAP) Observations: Final Maps and Results", APJS (2012).

[68] Planck Collaboration et al., "Planck 2015 results - I. Overview of products and scientific results", A&A **594**, A1 (2016).

[69] ESA and the Planck Collaboration, *Map of CMB temperature from SMICA*, https://www.cosmos.esa.int/documents/387566/425793/2015_SMICA_CMB/c8c4c802-4b76-49da-b80a-0fb8d02c62b7?t=1423083319437, Feb. 2015.

[70] ESA and the Planck Collaboration, *Power Spectrum of temperature and fluctuations in the Cosmic Microwave Background*, http://sci.esa.int/planck/51555-planck-power-spectrum-of-temperature-fluctuations-in-the-cosmic-microwave-background/, Mar. 2013.

[71] W. Hu, N. Sugiyama, and J. Silk, "The Physics of Microwave Background Anisotropies", Nature **386** (1997) 10.1038/386037a0.

[72] P. de Bernardis et al., "A flat Universe from high-resolution maps of the cosmic microwave background radiation", Nature **404**, 955 (2000).

[73] W. Hu and S. Dodelson, "Cosmic Microwave Background Anisotropies", Annual Review of Astronomy and Astrophysics **40**, 171 (2002).

[74] J. Silk, "Cosmic Black-Body Radiation and Galaxy Formation", APJ **151**, 459 (1968).

[75] Y. Akrami et al., "Planck 2018 results. I. Overview and the cosmological legacy of Planck", (2018).

[76] T. Caudron, "ALICE official schematics (2012)", General Photo, Apr. 2012.

[77] J. Schukraft, "Heavy Ion physics with the ALICE experiment at the CERN LHC", Phil. Trans. Roy. Soc. Lond. **A370**, 917 (2012).

[78] *ALICE Inner Tracking System (ITS): Technical Design Report*, Technical Design Report ALICE (CERN, Geneva, 1999).

[79] The ALICE Collaboration et al., "The ALICE experiment at the CERN LHC", Journal of Instrumentation **3**, S08002 (2008).

[80] G. Dellacasa et al., *ALICE time projection chamber: Technical Design Report*, Technical Design Report ALICE (CERN, Geneva, 2000).

[81] P. Cortese et al., *ALICE forward detectors: FMD, TO and VO: Technical Design Report*, Technical Design Report ALICE, Submitted on 10 Sep 2004 (CERN, Geneva, 2004).

[82] K. Aamodt et al., "Centrality Dependence of the Charged-Particle Multiplicity Density at Midrapidity in Pb-Pb Collisions at $\sqrt{s_{\mathrm{NN}}}$ = 2.76 TeV", Phys. Rev. Lett. **106**, 032301 (2011).

[83] K. M. Gorski et al., "HEALPix - A Framework for high resolution discretization, and fast analysis of data distributed on the sphere", Astrophys. J. **622**, 759 (2005).

[84] P. Peebles, "Statistical Analysis of Catalogs of Extragalactic Objects. I. Theory", ApJ **185**, 413 (1973).

[85] B. D. Wandelt, E. Hivon, and K. M. Gorski, "The pseudo-cl method: cosmic microwave background anisotropy power spectrum statistics for high precision cosmology", Phys. Rev. **D64**, 083003 (2001).

[86] E. Hivon et al., "Master of the cosmic microwave background anisotropy power spectrum: a fast method for statistical analysis of large and complex cosmic microwave background data sets", Astrophys. J. **567**, 2 (2002).

[87] M. Machado, P. H. Damgaard, J. J. Gaardhøje, and C. Bourjau, "Angular power spectrum of heavy ion collisions", Phys. Rev. C **99**, 054910 (2019).

[88] J. Adam et al., "Centrality evolution of the charged-particle pseudorapidity density over a broad pseudorapidity range in Pb-Pb collisions at $\sqrt{s_{\mathrm{NN}}}$ = 2.76 TeV", Phys. Lett. **B754**, 373 (2016).

[89] HEASARC and Astrophysics Science Division at NASA/GSFC, *HEALPix Pixel Coordinates*, https://lambda.gsfc.nasa.gov/toolbox/tb_pixelcoords.cfm#pixelinfo, Page updated Nov 2008.

[90] S. Chatrchyan et al., "Measurement of higher-order harmonic azimuthal anisotropy in PbPb collisions at $\sqrt{s_{NN}}$ = 2.76 TeV", Phys. Rev. C **89**, 044906 (2014).

[91] Z.-W. Lin, "Evolution of transverse flow and effective temperatures in the parton phase from a multi-phase transport model", Phys. Rev. **C90**, 014904 (2014).